CONCENTRATION PROFILER (CCP) FOR THE MEASUREMENT OF NEARBED SEDIMENT CONCENTRATIONS:

APPLICATION IN THE SWASH ZONE ON A LABORATORY BEACH

BY

JOSEPH W. C. FARIES

AND

JACK A. PULEO

TABLE OF CONTENTS

Chapter

LIST OF FIGURES

ix

LIST OF TABLES

ABSTRACT

The swash zone, the landward extension of the surf zone, acts as a conduit for sediment to exchange between the dry portion of the beachface and the sub-aqueous offshore beach profile. Therefore, having a more complete description of swash morphodynamics is paramount for improving nearshore morphology models. However, the complexity of swash flows in addition to turbulence and infiltration make swash processes difficult to understand and data difficult to collect. To date, almost all instantaneous measurements of swash zone sediment transport have excluded motion closer than 0.01 m above the instantaneous bed completely missing bedload contributions. Time integrated sediment traps have shown that the bedload component can be dominant. Therefore, the investigators in this work have used 3 commercial Conductivity Concentration Meters (CCM) by Deltares along with a fabricated Conductivity Concentration Profiler (CCP) to measure sediment concentration profiles in the near bed/bedload regime in the swash zone of a laboratory beach under solitary waves.

The development of the CCP proved to be a difficult task. Several preliminary CCP prototypes and test sensors have been fabricated and tested leading to the most recent CCP prototype from which data are presented. The iterative process of CCP fabrication has yielded a CCP that is robust, clearly detects varying concentrations of sediment, produces repeatable results in simple tests, and collects independent measurements at different elevations simultaneously. However, the evolution of the CCP is not yet complete. The future development requires more attention to the physical structure of the sensor as scour has been shown to effect data collection.

Data showing the near bed concentration signals which have eluded previous investigators along with swash depth and velocity at different locations in the swash zone are presented. Assuming a velocity boundary layer profile, the velocity and concentration signals yield approximations of instantaneous sediment transport throughout swash cycles. The net transport approximations resulting from different boundary layer profiles have been compared to beach erosion calculations from beach profile measurements made after each swash event. The average measured beach profile change was 0.3459 kg of sand eroded per swash event. The profile erosion calculated based on the difference between transport calculation at different cross-shore locations ranged from 0.3823 to 4.4502 kg reflecting the uncertainty associated with assuming a velocity boundary layer profile.

Future work involves the deployment of sensors at multiple cross shore locations and adding Fiber Optic Backscatter Sensors (FOBS) to the sensor array (to measure sediment concentrations further above the bed). The most important development necessary is a technology capable of measuring sediment velocity near the bed that could be coupled with concentration measurements for more accurate transport calculations. Ultimately, larger scale laboratory and field experiments will supplement modeling efforts to improve shoreline evolution predictions.

Chapter 1

OVERVIEW OF THE SWASH ZONE: A BRIEF REVIEW

Scanning the literature yields different technical spatial definitions of the swash zone. One suggestion is that the seaward edge of the swash zone is where bore turbulence significantly begins to drive sediment motion at the sea bed [1]. A more common definition is simply the wet/dry region of the nearshore beach profile where run up and down occurs resulting from collapsed wave bores (See Figure 1.1). The former definition implies the connection between the surf zone and swash zone, which has been a focus of recent data collection and modeling attempts[1]. However, for the scope of the experimentation conducted, the simpler definition of the swash zone is sufficient.

1.1 Significance

There are several reasons why the swash zone is an important part of the nearshore environment that necessitate a better understanding of swash zone processes. Firstly, the swash zone essentially acts as a conduit for sediment, and, to a lesser extent, turbulence between the upper beach and the surf zone [1]. Secondly, substantial quantities of longshore sediment transport may occur within the swash

---

[1] Will be discussed subsequently in this chapter.

zone [2].[2] Swash processes are also pertinent academically as they are often determining factors of beachface slope and thought to be a formation mechanism for beach cusps. The equilibrium beachface slope, which tends to be steep, is thought to represent a balance between the onshore asymmetry of swash flows and gravity forces [3].
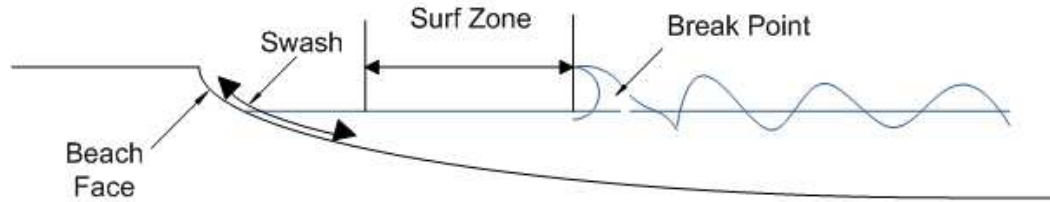
Figure 1.1: A skecth of the nearshore profile. As per the data presented in Chapter 5, the relevant spatial definition of the swash zone is the portion of the beach profile where broken waves run up and down the beachface.

The implications of swash processes on cross shore sediment transport and beach morphology have been declared throughout the literature in recent decades e.g. [4]. Swash processes determine whether sand grains are deposited on the beachface or transported into the surfzone making it the region that dictates whether a beach erodes or accretes. For the same reason, swash zone morphodynamics account for post-storm beach recovery. Therefore, it has long been established that the inclusion of swash zone sediment transport data is important for the validation of shoreline evolution models e.g. [5]. However, data collection and modeling efforts in the swash zone have lagged behind other areas in the nearshore.

Morphodynamic research in the swash zone had been lacking due to the perception that it was prohibitively difficult to conduct. Swash forcing is characterized by aerated, rapid, direction reversing flows carrying high sediment concentrations.

---

[2] The research described here in does not address the longshore component, however the swash zones contribution to total littoral drift is of great practical importance.

This, coupled with turbulence and infiltration account for these difficulties (Figure 1.2). It has been described as the most scientifically challenging oceanic environment for predicting sediment transport [6]. However, the swash zone is the most accessible region of the nearshore environment. Therefore there has been a renewed interest in swash investigations in the last 15-20 years.
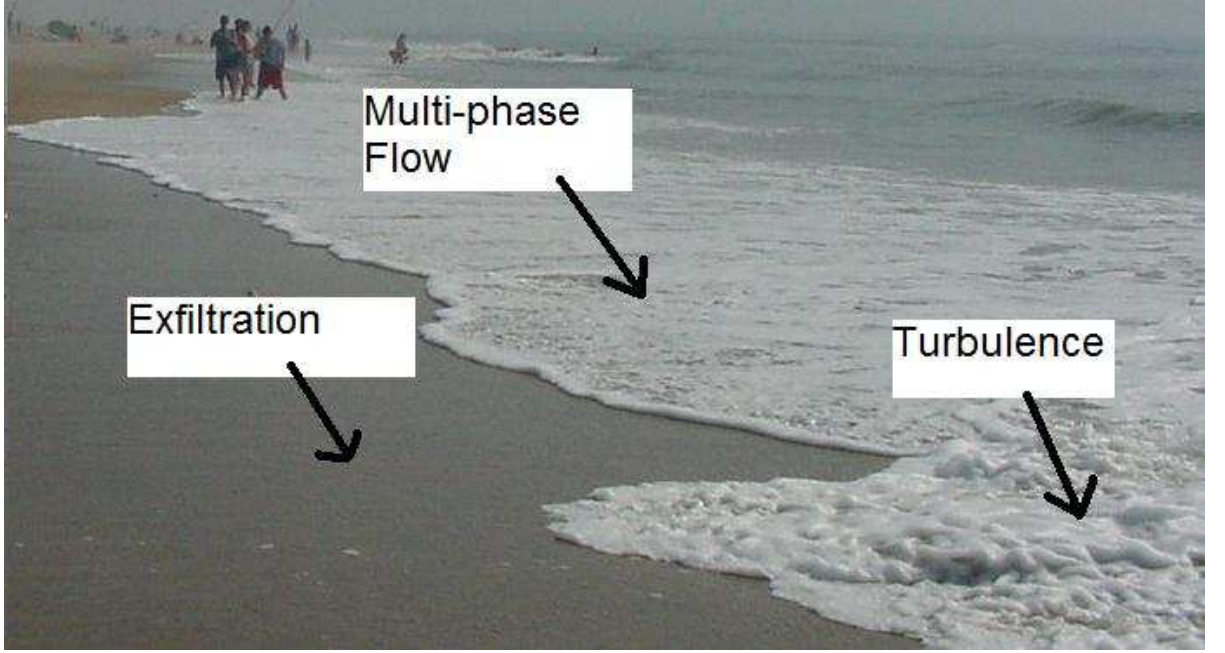
Figure 1.2: The complicated processes occurring in the swash zone are difficult to predict and make data collection non-trivial.

1.2 State of Research

1.2.1 Hydrodynamics

Over the last decade, measurements of swash zone hydrodynamics have led to generally accepted knowledge of swash flow patterns. Cross shore velocity data collected by electromagnetic current meters (EMCM) [7] and acoustic Doppler velocimeters (ADV) [8] have shown the asymmetry between uprush and backwash.

Hydrodynamic modeling has attempted to keep pace with the growth of laboratory and field swash zone data collection. For example, Rbreak [9], a one-dimensional time-domain wave model based on the fully nonlinear shallow water wave equations (DNLSWE), was extended to include swash velocities. The model over predicted swash zone velocity skewness and the ratio between maximum uprush and back-wash velocities [10]. More recently modeling attempts have included high resolution Navier-Stokes solvers. Recently, NEWFLUME [11], a 2D Reynolds-averaged Navier-Stokes equations solver for an incompressible fluid, has been utilized to simulate idealized swash over planar, impermeable slopes [12]. The simulated results yielded short-lived onshore temporal accelerations (due to the pressure gradient overcoming gravitational forces) during initiation and termination of the swash cycle. Convective accelerations were found to be either zero or slightly directed onshore away from the rundown limit where convective accelerations are the largest. However, the results are for idealized cases and must be extended to natural beaches with random wave forcing.

1.2.2 Sediment Transport

Like hydrodynamic models, sediment transport modeling attempts have failed to accurately predict field observations in a consistent manner. In fact, instantaneous sediment transport predictions are far worse than their hydrodynamic counterparts. Some researchers report instantaneous transport predictions within a factor of 2-3 [13]. The reason for this inaccuracy is the fact that researchers tend to use transport physics from predictive equations for uni-directional, open-channel flow[3].

These Bagnold-type equations state that a fraction of the energy dissipation is effective in moving sediment [14]. The energetics-based equations model the shear stress on the bed using a quadratic drag law that is dependent on a friction factor.

---

[3] It has already been stated that swash flows have unique characteristics and therefore a translation from classical hydraulics is intuitively wrong.

4

This friction factor has been shown to be different for uprush and backwash and is largely dependent on grain size. Conflicting literature exists on how the friction factor changes in a given swash cycle. A comprehensive set of video based observations of swash flows compared with a simple hydrodynamic model showed that the backwash friction factors varied throughout tidal time scales but were consistently higher than frictional values for uprush [15]. On the other hand, direct measurements of bed shear stress using a hot film shear stress sensor showed that friction factors were consistently greater during uprush rather than backwash [16]. This is likely due to turbulence advected from the surf zone (not quantified in video imagery). Since they are calculated rather than measured, friction factors are inherently dependent upon the model that is used to tune them. Further, the importance of accurate friction factors (and therefore Bagnold-type models) is questionable due to the presence of other first order factors such as turbulence advection from the surf zone [1] and infiltration/exfiltration, which are excluded in these models.

Recent research has attempted to quantify the importance of turbulence and sediment advection from the surf zone into the swash zone. A field study using streamer traps showed that suspended sediment transport in the uprush is driven by two distinct mechanisms: sediment advection from bore collapse and subsequent local suspension due to bore propagation up the beachface [17]. More recently, a laboratory experiment was designed such that only the sediment picked up during bore collapse shoreward of the swash zone was measured. Sediment was trapped during the uprush of a solitary wave on an impermeable beachface. The experiment was coupled with a model that resolves the hydrodynamics using DNLSWE solutions for the hydrodynamics in an Eulerian framework and solves the advection - diffusion equation for turbulence and suspended sediment in a Lagrangian framework [18]. These recent results further verify the importance of modeling the generation and advection of turbulence to account for the cross shore advection of sediment into

the swash zone which has been stated throughout the literature in the past decade e.g. [1], [19], [20].

During a given uprush event, it is likely that the flow will reach portions of the beachface that are unsaturated. This will result in some water infiltrating the beachface depending on the grain size and hydraulic conductivity properties of the sediment making up the beachface. Conversely, during backwash, water is likely to exfiltrate from the bed. Again, this depends on the sediment properties and is driven by the relationship between the beach groundwater table and the mean water level. Infiltration increases the effective weight of (thus, acts to stabilize) the bed sediment and visa versa. However, infiltration also modifies the boundary layer. Therefore infiltration can act to destabilize the bed by inducing stronger shearing stresses and vice versa. These effects likely account for the changes in the backwash friction factor throughout a tidal cycle [15]. The decrease in friction factor during a rising tide may be attributed to percolation into the bed as uprush reaches unsaturated portions of the beachface. Recent simulations have, however, shown that these effects play key roles in the evolution of coarse-grained beaches but are not significant contributors for sand beaches [21].

In addition to the trap studies, several measurements of instantaneous suspended sediment transport have been made in recent years e.g. [1], [22]. In many of these studies suspended sediment concentration was quantified using optical backscatter sensors (FOBS) [23]. The principle behind these sensors is that a light source is emitted into the water column, backscatters off of suspended particles and is received by a detector in the sensor. The amount of light backscattered is proportional to sediment concentration obtained via laboratory calibration curves. The optical approach is not appropriate in the direct vicinity of the bed because the light signal can be backscattered off the bed itself and optical sensors usually are linear in concentration out to only about 200 kg/m^3. Therefore, measurements

of instantaneous sediment transport in the swash zone have excluded motion closer than 0.01 m from the instantaneous bed. This limitation has caused the end of backwash where the flow is very shallow (< 0.01 m) with high velocities and sediment concentrations to be missed in instaneous measurements. This final portion of backwash has been described as a 'slurry' of sand and water [24] arising from sheet flow conditions.

1.3 The Missing Component

Thus far, only investigations of suspended sediment tranport have been discussed. However total sediment transport is described as a combination of suspended load, bed load, and sheet flow. Whereas the suspended load is supported by turbulence fluctuations, the bed load results from intergranular collisions where particles remain in the direct vicinity of the bed. Sheet flow conditions occur when excess shear stress is large and results in the sliding of entire 'sheets' of sediment along the bed [25]. A field study was conducted by Horn and Mason (1994) to compare the relative importance of bedload versus suspended load. They did so by constructing two separate sediment traps, one which collected sediment to a height of 0.01 m above the bed (defined as bedload) while the other captured sediments above 0.01 m (suspend load). Traps were deployed for half swash cycles to capture total load during uprush or backwash in the mid-point of the swash zone at four sites in the United Kingdom. Of the four beaches studied, bedload was dominant in the backwash at three sites, and in both uprush and backwash at two sites [26].

The assignment of bedload to within 0.01 m coincides with the definition of bedload as being within 10 grain diameters of the bed as the median grain size at all sites was between 0.002 - 0.005 m. However, it is not absolute truth that this distance contains solely grains driven by bedload mechanisms. Because of this, it can be argued that the height relative to the bed is an incorrect specification of bedload versus suspended load. This is a moot point, the striking fact is that *nearbed*

7

sediment transport has been shown to be a significant component of the total load. Further this nearbed transport has been completely missed by almost all previous studies. One published study could be located that investigated instantaneous bed-load concentrations in the swash zone of a sandy beach [27]. It contained just a few short time series on a low energy beach but did indicate large variability in the quantity of sediment mobilized in the bedload layer.

Net transport in the swash zone results from the small differences between large total loads transported in the uprush and backwash [28]. Therefore, failing to accurately predict all transport contributions throughout the entire swash cycle disturbs this fine balance and could lead to the prediction of net transport in the wrong direction. The errors in morphodynamic modeling efforts arise partly due to the difficulties in predicting swash zone sediment transport and shoreline change without measurements from the nearbed component. Obtaining instantaneous vertical profiles of nearbed transport (from below the bed to 0.005 - 0.01 m above the bed) is an important endeavor to pursue to advance the understanding of swash zone sediment transport.

Chapter 2

DEVELOPMENT OF THE CONDUCTIVITY CONCENTRATION PROFILER

The fact that nearbed sediment concentrations had yet to been measured in the swash is not due to a lack of interest by swash zone researchers. It merely reflects the difficulties of obtaining such measurements and the lack of adequate technology to do so. Therefore a new tool, a Conductivity Concentration Profiler (CCP), has been designed specifically for profiling nearbed sediment concentrations. The development of the CCP proved to be a difficult task. This chapter will detail the development, calibration, and behavior of the sensor.

2.1 Methodology

Optical techniques (described in the previous chapter) are problematic at high sediment concentrations and the signal is often obscured by the bed itself. Therefore, a different approach was necessary to measure nearbed sediment mobility which is characterized by high volumetric concentrations. In the spirit of past research efforts, the problem was approached using electrical conductivity as a proxy for sediment concentration.

The electrical conductivity of water (K) depends on its electrolytic constituents (β) and temperature (T).

$$K = f_1(\beta, T) \tag{2.1}$$

9

When sand is added to water, the volumetric concentration of sediment becomes a third variable upon which the conductivity of the sand/water slurry depends. In a laboratory set-up, the first two variables can be controlled such that the conductivity becomes strictly a function sediment concentration, c.

$$K = f(c) \tag{2.2}$$

Conceptually, tap water is mildly conductive (oceanic salt water, of course, much more so) while sand grains are poor electrical conductors. Therefore, the entrainment of sediment in a control volume of water will reduce the conductivity[1]. This conductivity drop due to the addition of sand grains can be calibrated to yield a local volumetric concentration of sediment.

2.2   Previous Sensors

An early example of a conductivity sensor fabricated for the purpose of detecting sediment concentration was Dick and Sleath's [1991] implantation of single electrodes in the sidewall of a U-tube to measure the sediment concentration in the boundary layer of oscillatory flow [29]. A second two-electrode sensor for measuring sediment concentration at a single point was developed by Horikawa et al. (1982) [30]. Their sensor differed from that of Dick and Sleath (1991) not only in that it used two electrodes, but that it was not fixed to a laboratory apparatus and could thus be re-deployed at arbitrary horizontal or vertical locations within a flume. It will be seen later that the CCP merges these two early designs.

Presently, the most widely used conductivity sensor for sediment transport is known as the conductivity concentration meter (CCM, Figure 2.1) manufactured by Deltares (formerly Delft Hydraulics). CCM's measure the sediment concentration at a single elevation using 4 electrodes oriented in a common plane. Electric current

---

[1] or increase the resistivity, as conductivity and resistivity are inverses of one another

is supplied to the inner 2 electrodes by the outer 2 electrodes. The conductivity of a solution in the vicinity of the sensor is detected by the inner 2 electrodes. From calibration procedures, the measured conductivity can be returned as a sediment concentration. Since the CCM yields a single point measurement, either the elevation relative to the at-rest bed must be adjusted under repeatable conditions or multiple CCM's must be deployed at different elevations at the same cross-shore location to determine a sediment concentration profile. Standard deployment involves the introduction of the CCM from below a laboratory flume where it can be raised or lowered using a linear actuator.

CCMs have been used to measure bedload concentrations and transport in the surf zone under non-breaking waves and under oscillatory flows in a U-tube [31], [32]. Under non-breaking waves it was found that the sheet flow layer varied between 10-60 grain diameters thick and that sediment fluxes in the sheet flow layer are much larger than those in the suspended load regime [33]. Sediment velocities for estimating flux were determined by cross-correlation of the signals from 2 CCM units separated a short distance in the along-flow direction. The swash zone study by Yu et al. (1991) also used CCMs but in a field application. Three CCM units were deployed from under the bed using a buried horizontal arm. A separation distance of between 0.002 to 0.003 m allowed for an estimation of the sheet flow thickness (0.008 m) and, what is believed to be, the first measurement of instantaneous swash zone bedload concentrations.
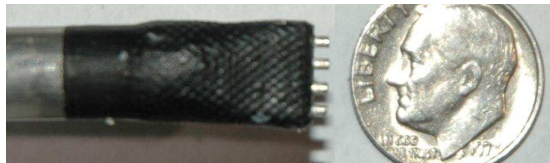
Figure 2.1: Photograph of CCM. Manufactured by Deltares, the outer pins of the CCM supply electric current to inner pins which detect conductivity.

11

2.3 Design Considerations

Our main interest is a sensor to profile nearbed sediment concentrations in the swash zone. None of the previously described sensors were specifically designed for swash zone research, even though the CCM has been used in the swash zone. Therefore, a new profiler has been developed. Several design considerations dictated the iterative process of developing a working CCP prototype. They include:

- Maximizing the dynamic range of the sensor

- Independence of each electrode pair

- Repeatability of calibrations

- Sensing volume of each electrode pair.

2.4 Evolving Prototypes and Circuitry Architecture

Over the past couple of years, several prototypes and test sensors had been constructed and tested. The difference between working prototypes and test sensors is that a working prototype fits the description of a concentration profiler and were used in laboratory tests while test sensors are crudely fabricated to tune the circuitry by conducting "bench top" tests. Each successive working prototype applied lessons learned from its predecessors in addition to a countless number of bench top observations.

2.4.1 Fundamental Component: The First Working Prototype

The fundamental component in the most recent CCP prototype circuitry is carried over from initial tests of very simple sensors. The first sensor was a single channel sensor that was created by attaching wires to an Integrated Circuit (IC) socket extender. The sensor wires were attached to a strain gage reader. A strain gage reader utilizes a Wheatstone bridge in which one of the resistors on the bridge

is a strain gage transducer. In the modified configuration, the simple IC sensor replaced the strain gage transducer. In this case, the fourth resistor in the bridge is the resistance of the medium that surrounds the sensor electrodes (IC pins).

Using Ohm's Law, and Figure 2.2 as a guide, the theoretical operation of a strain gage type application of a Wheatstone bridge can be quickly explained. The voltage supplied by a DC source (V_{in}) is equal to the voltage through each half of the Wheatstone bridge (V_{CDA} & V_{CBA})

$$V_{in} = V_{CDA} = V_{CBA} \tag{2.3}$$

By Ohm's Law,

$$V_{in} = I_{CDA}(R_{CCP} + R_3) = I_{CBA}(R_1 + R_2), \tag{2.4}$$

where I_{CDA} and I_{CBA} are the electric currents through leg CDA and CBA, respectively, and R_1, R_2, R_3 and R_{CCP} are the resistances in a given quarter of the bridge (Figure 2.2).

The logger records the difference between the voltage drop from C to D (V_{CD}) and the voltage drop from C to B (V_{CB}).

$$V_{CD} = I_{CDA}R_3 = \frac{V_{in}}{R_3 + R_{CCP}}R_3 \tag{2.5}$$

$$V_{CB} = I_{CBA}R_2 = \frac{V_{in}}{R_1 + R_2}R_2 \tag{2.6}$$

$$V_{logged} = V_{in}\left[\frac{R_3}{R_3 + R_{CCP}} - \frac{R_2}{R_1 + R_2}\right] \tag{2.7}$$

In the case of a balanced bridge, where the resistance in all quarters of the bridge is the same, the voltage that is sent to the logger is null. The initial approach was to tune the resistance in the strain gage reader such that the resistivity detected by the sensor in clear water was balanced. In this case, the addition of a sediment

concentration would increase the resistance of the water and would unbalance the bridge resulting in a voltage output to the logger.
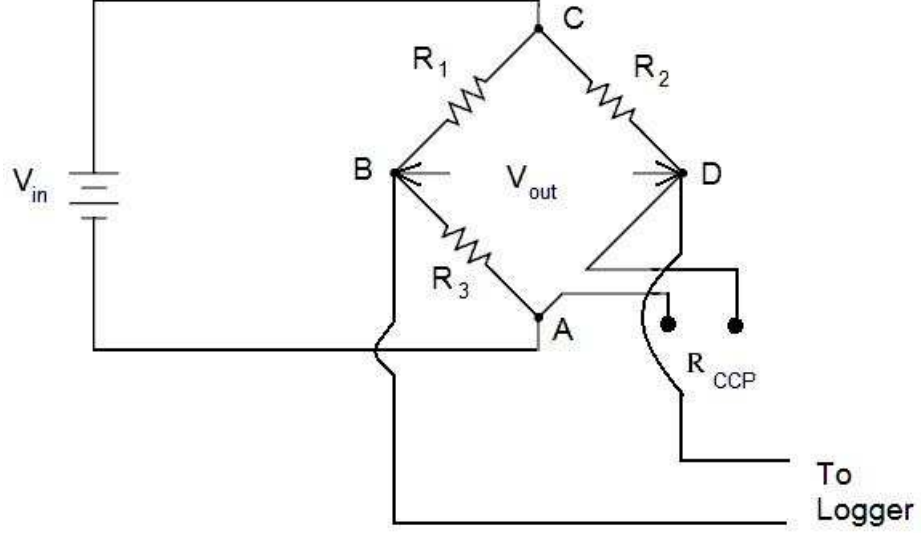
Figure 2.2: The earliest sensor merely copied a strain gage reader circuitry. A modification of this circuitry survives in the most current prototype.

It was found that it was not possible to keep the bridge balanced. This is because the resistance of the water as detected by the sensor is not steady. This is due to polarization which causes sensor drift (discussed briefly in Section 3.5.2.2). Therefore, the strain gage type circuitry was modified such that the resistance across the sensor electrodes acted in parallel to a quarter of an otherwise balanced bridge (Figure 2.3).

The equivalent resistance (R_{eq}) in the quarter of the bridge that contains the sensor is given by

$$R_{eq} = \frac{1}{\frac{1}{R} + \frac{1}{R_{CCP}}} \qquad (2.8)$$

14

The relationship governing the voltage output to the logger, Equation 2.7, now becomes:

$$V_{logged} = V_{in} \left[\frac{R}{R + R_{eq}} - \frac{1}{2} \right] \qquad (2.9)$$

The bridge resistance value R was set to 110kΩ. This was chosen to match the approximate resistance of tap water according to crude measurements using an Ohm meter. Further bench top tests resulted in the conclusion that 110KΩ yielded the best results.
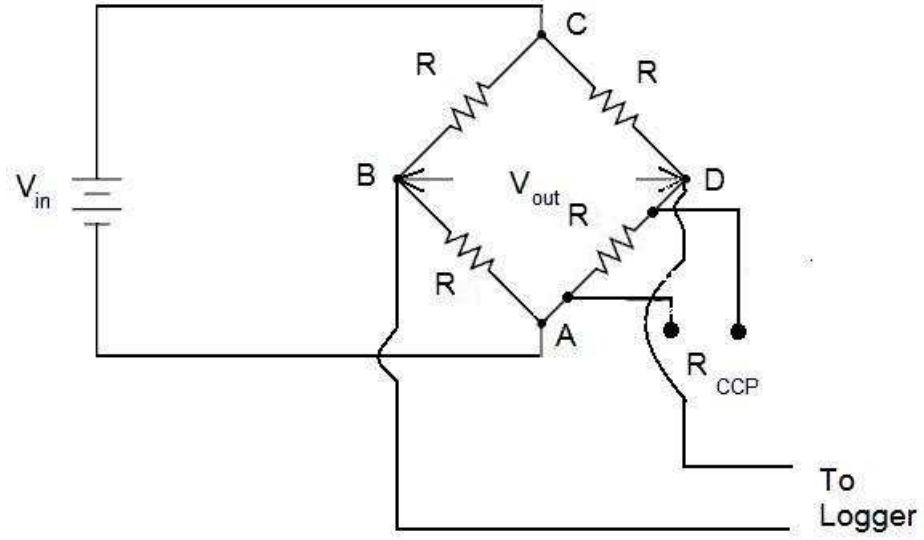
Figure 2.3: This slight modification of the basic strain gage bridge, with the sensor acting as a parallel resistor, has survived through the most recent prototype.

From these early tests, the first conductivity/resistivity profiler was fabricated and tested. The first working prototype was a three channel sensor built using #28 copper telephone wire (Figure 2.4, right). The copper wire protruded through a slim acrylic body by about 0.003 m. The direct current was supplied by a 9 volt (9V) battery. This first prototype showed promise in simple tests. The sensor

15

was able to clearly detect the interface between a packed sediment bed and a clear water column as the sensor was pulled up through the bed into the water column (Figure 2.4, left). While this simple design showed promise, the application of DC caused the deterioration of an electrode due to electrolysis. This effect was substantial enough to render the electrode pair useless after just a few tests. A second effect of this, is that the deterioration of an electrode represents the transfer of copper ions to the water. This, in turn, causes the chemical concentration of the water to be an uncontrolled variable (see Section 2.1). One of the earliest considerations was eliminating this effect.
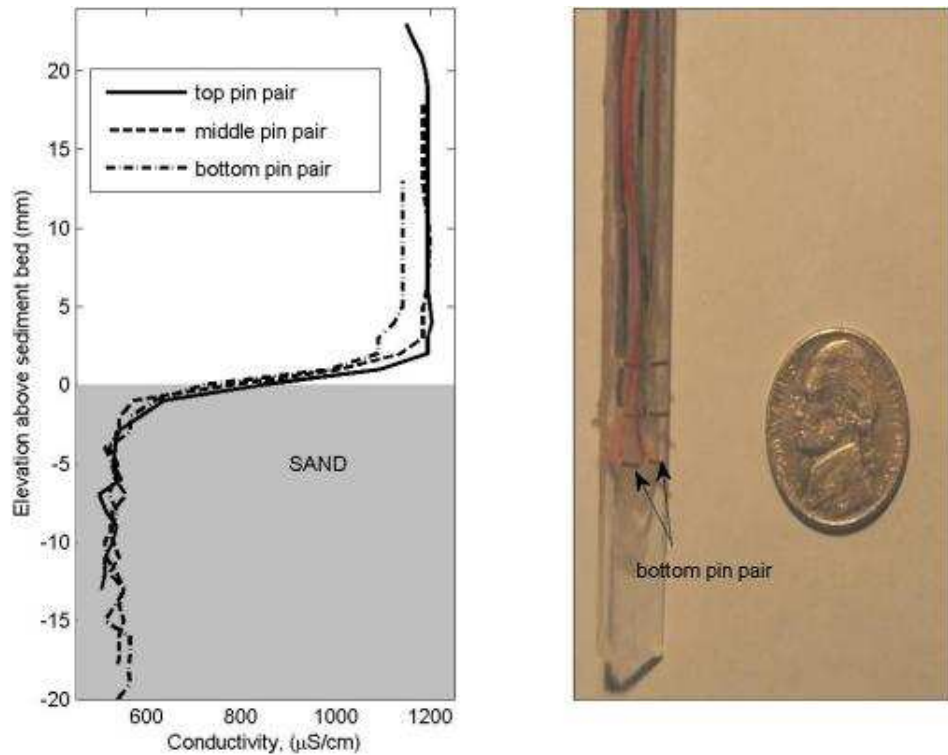
Figure 2.4: The plot (left) shows the response of the first working prototype (horizontal axis) at different sensor elevations relative to the bed/water interface (vertical axis). (Right) The first working prototype consisted of three electrode pairs made of copper wire.

16

The simple solution is to apply an alternating current (AC) to the sensing pair. However, doing so would cause an oscillating sensor response, which is undesirable. At a fixed sediment concentration, the sensor ought to respond consistently. If the time scales over which sediment concentration changed was slow enough to filter out the oscillations induces by AC, the mere application of AC would be sufficient. However, this is not the case for instaneous sediment concentrations in the swash zone. Therefore, it was necessary to recover a DC signal while applying AC to mitigate sensor deterioration.

To do so, a full wave bridge rectifier was designed to convert an AC sine wave to a full wave pulsating DC signal. The operation of a full wave bridge rectifier can be described in terms of current flow from higher potential to lower potential. Using Figure 2.5 as a guide, the physics by which a full wave bridge rectifier works can be explained. The sketch on the left in Figure 2.5 shows the bridge in the positive half of the AC wave. Point A has the highest potential causing current to flow to B. At this point diode D_3 is forward-biased and, therefore, allows current to flow to C while D_1 is reversed-biased and, therefore, does not conduct current. Now point C has higher potential than D and current flows from C to D through the load resistor R_L with the polarity shown in Figure 2.5. The current is now conducted from D to E through the common ground. At this point diode D_2 is forward-biased and D_4 is reverse-biased allowing current to flow strictly to point F. Finally current flows from point F (high potential) back to the negative terminal of the battery, point G (low potential). Similarly, in the negative half of the AC signal electrical current flows from G to F, F to C (through diode D_4), C to D (through the load resistor R_L), D to E (through ground), E to B (through diode D_1), and finally from B back to A. Notice, the polarity between C and D is the same for both the positive and negative half of the AC sine wave [34].

17
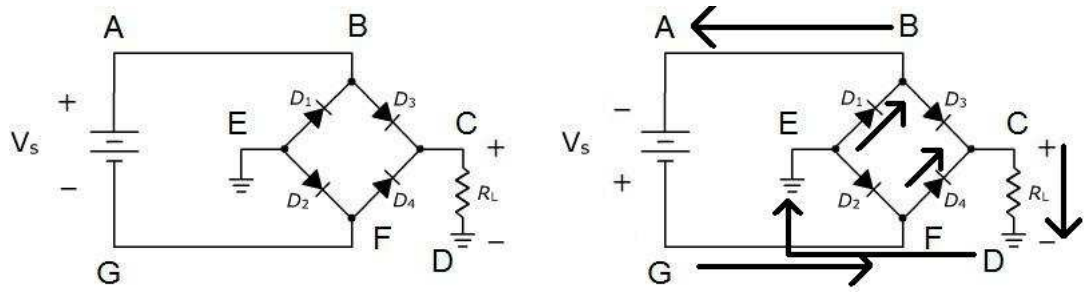
Figure 2.5: The flow of electrical current through the full wave bridge rectifier is driven by flow from high electric potential to low electric potential. The arrows in right hand figure represent the flow path of the electric current. The polarity at the sensing electrodes are the same in both the positive (left) and negative (right) portion of the AC sine wave.

Rather than a pure sine wave being sent to the logger, just the absolute value of the sine wave is sent (Figure 2.6, black). However, the result is still a fluctuating, periodic signal (a pulsating DC signal), not a pure DC signal. The application of a smoothing capacitor acts to smooth the ripple output of the rectifier to more closely resemble a DC signal (Figure 2.6, blue). The capacitor, which charges and discharges in every half AC cycle, only allows the diodes to conduct when the voltage is greater than the charge of the capacitor. The higher the capacitance, yields a smoother signal to the point that a DC signal is obtained. However, too great of capacitance would lead to lags in the circuitry due to the time required to overcome the capacitance. This is clearly undesirable as the CCP should respond instantaneously with a change in sediment concentration/conductivity. It was found that a 0.22 μF capacitor and a load resistance of 150 kΩ, yielded a DC signal without inducing lag.
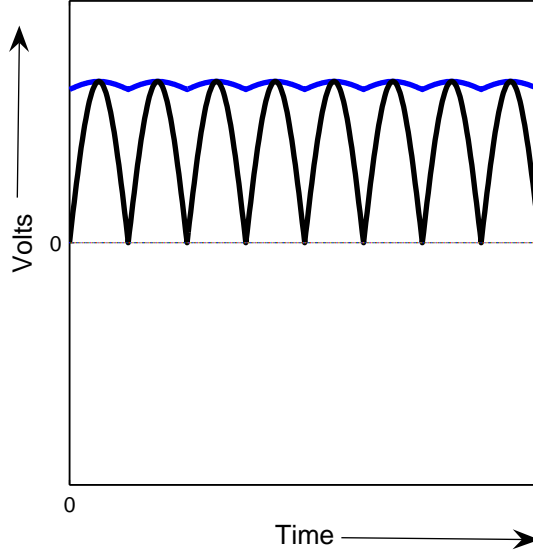
Figure 2.6: A smoothing capacitor is added to the rectifying bridge to yield smaller amplitude oscillations (blue) in the pulsating DC signal (black).

2.4.2 Single Electrode Approach: The Second Working Prototype

The use of AC introduces other complications in the circuitry, which the DC descriptions in the previous section fail to consider. Some of these effects will be addressed later. (Not all physics describing the effects of AC will be analyzed). In order to limit difficulties, the second working prototype was modeled after the type of fabricated conductivity probes that was most prevalent in the literature. This was done in hopes that the tests done by others would guide a successful prototype. Most other researchers investigating salt concentrations (e.g. [35]) or electrolytic properties of a fluid (e.g. [36], [37]), fashioned single electrode probes following the work of Gibson and Schwarz [38].

Physically, when a small electrode and a very large electrode are immersed in a conducting fluid, most of the resistance measured by the sensor is detected locally about the smaller electrode. It has been shown and well documented that

19

the measurement volume is contained within ten times the physical diameter of the smaller electrode [38].

The single electrode prototype consisted of eight sensing electrodes. Coated stainless steel wires each with a diameter of 0.25 mm constituted the smaller electrodes. The wires protruded through a pre-drilled acrylic body and ran up the back of the acrylic. The end of the wires that protruded through the body did so by about 2.0 mm and the tips of these wires were stripped of their coating. These stripped wire tips represent the sensing electrodes of the CCP. The other end of the wires were connected to shielded cables at a screw terminal. A stainless steel mesh attached to the face of the body acted as the large common electrode (Figure 2.7).
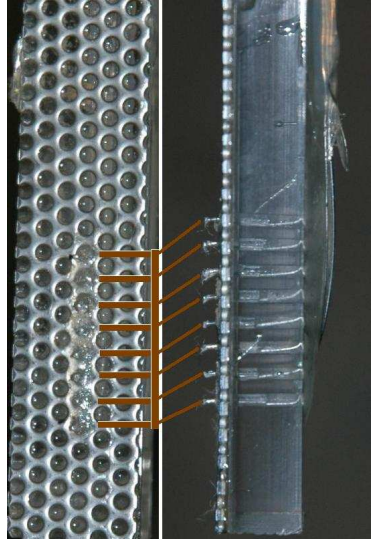
Figure 2.7: (Left) The front view of the CCP prototype. The steel mesh acts as the large common electrodes, the red lines point to the protruding smaller electrodes which are visible in the side view (Right).

In this circuitry, a resistor divider network (Figure 2.8) replaced the full Wheatstone bridge. The resistance of the control volume surrounding the sensing electrode acted as a resistor in parallel with a 680 kΩ resistor (R_P in Figure 2.8).

The effective resistance of this resistor pair is given by Equation 2.8. The choice of 680 kΩ was such that the resistance was large enough relative to the resistance of water (roughly 100 kΩ) such that small increases in resistance at the sensing electrode altered the effective resistance. A second resistor of 2.2 MΩ (R_S in Figure 2.8) acted in series with the effective resistance resistors in parallel. This worked to reduce the electric current to the electrode. Too high of a current to the electrode would cause heating of the water which is undesirable as temperature ought to be a controlled variable. The full wave rectifier with a capacitor remained in the circuitry to recover a DC signal.
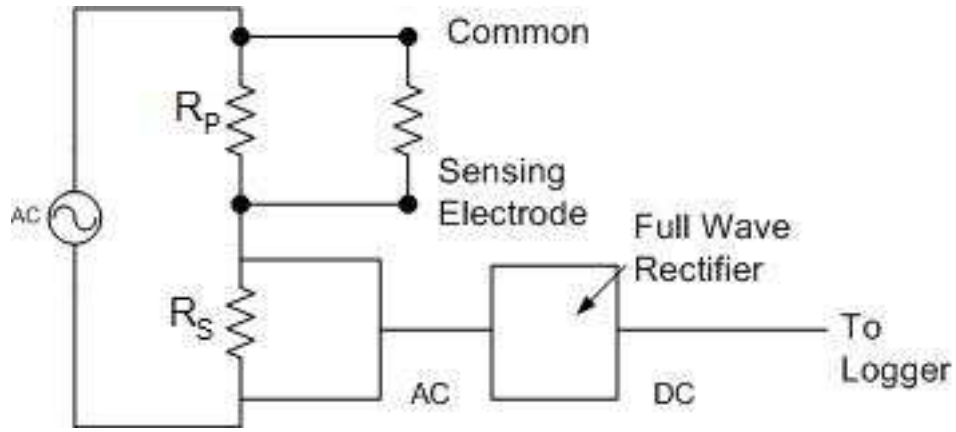
Figure 2.8: This circuitry replaces the Wheatstone bridge with a resistor divider network.

This prototype, as well, showed promise. The sensor was used to collect actual data from the swash zone in the lab. This data, however, was purely to test sensor performance rather than analyze swash zone sediment transport. The sensor was placed in the swash zone of waves generated in a large wave tank with a fine-sand beach. Swash depth and velocity at the same cross-shore location was recorded by a buried wave gage and an ADV, respectively. Random waves were generated and swash data were collected over a five minute time series of waves.

The data were then scanned for promising signals.

An example of a promising signal obtained from this prototype is shown in Figure 2.9. The data show the inverse of the CCP signal (a proxy for resistivity) for one of the electrodes that was roughly 2.0 mm below the bed in the top plot. The regions between a black and a brown line denotes where the resistivity decreased, while, in the region between the two brown lines, the resistivity increased. Since resistivity and sediment concentration are directly proportional, between black and brown are regions where sediment concentration decreases. This represents the bed being mobilized and occurs in the beginning part of uprush and the end of backwash when velocities are high. During flow reversal, the bed settles. This example time series shows that the CCP was able to detect bed mobilization events in the swash zone.
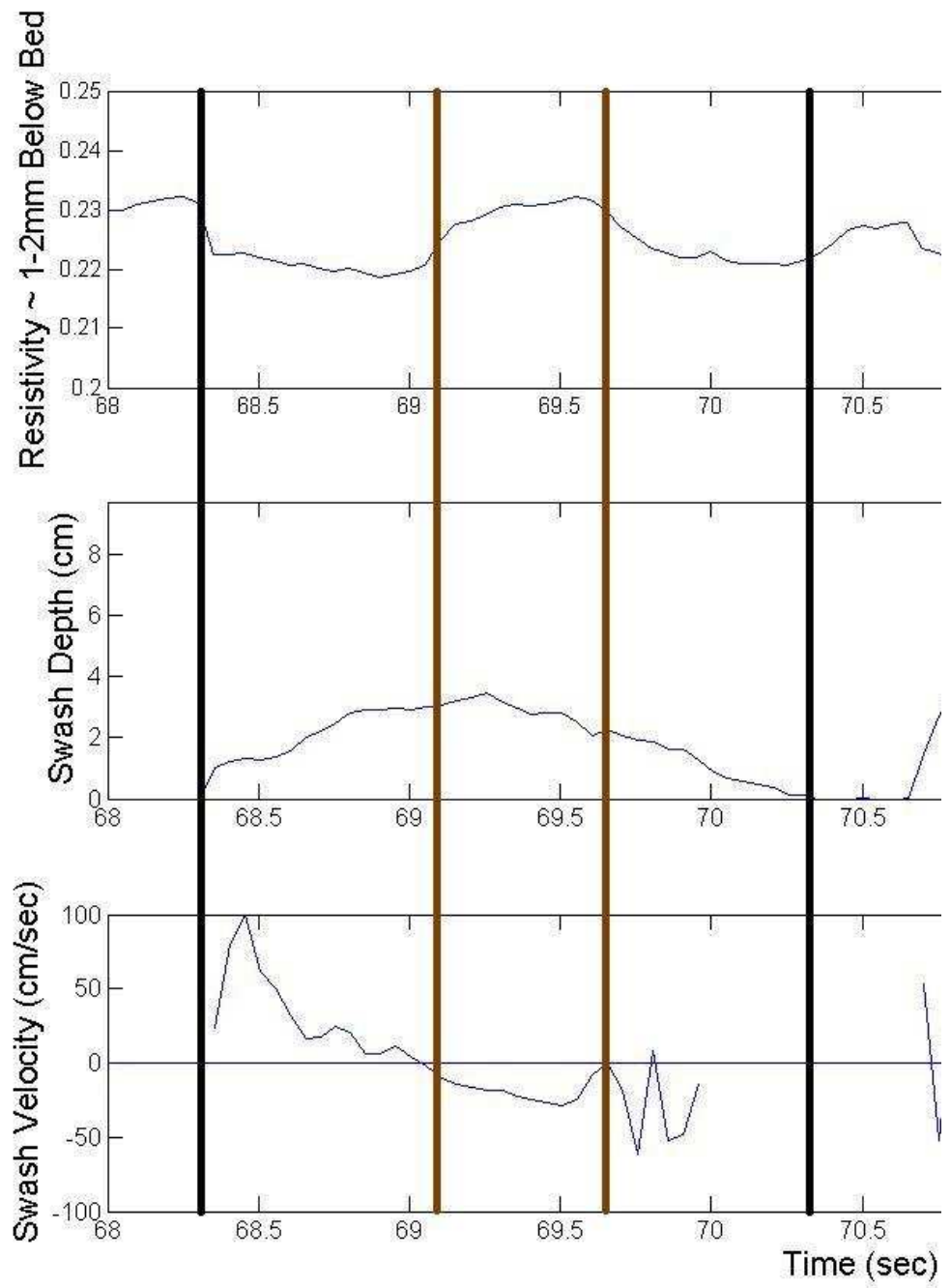
Figure 2.9: The sensor appeared to detect bed mobility (top plot) when swash velocity (bottom plot) was high, and bed stability as velocities were low.

23

Further bench top tests revealed a problem with the sensor. It was noticed that each individual electrode was not independent of the other electrodes. A change in voltage logged by one channel induced smaller changes in all other channels. Figure 2.10 exemplifies this cross talk amongst all of the channels. In the simple test, the sensor was incrementally lowered into a volume of water. A voltage change in a channel that was still in air due to a change in another channel's voltage due to its intrusion into the water suggests that cross talk exists. In Figure 2.10, three adjacent electrodes responses are shown through this test. All eight show the same behavior but only three are presented for clarity. Also, the signals are offset arbitrarily, again, for clarity. The large jump in sensor output corresponds to the electrode being submerged while the seven smaller jumps correspond to other electrodes being submerged. The magnitude of the smaller jumps was roughly 0.07 V. The sum of all of the smaller jumps was about 0.50 V (i.e. the difference between a sensor's output if it alone was submerged and a sensor's output if it and all others were submerged). To say the error introduced by this phenomenon is significant is an understatement, the total dynamic range (i.e. the difference between a sensor's reading in water and a sensor's reading in a packed bed) was roughly 0.40 V. Thus, cross talk effects would likely dominate the signal and obscure effects due to actual changes in conductivity (sediment concentration).
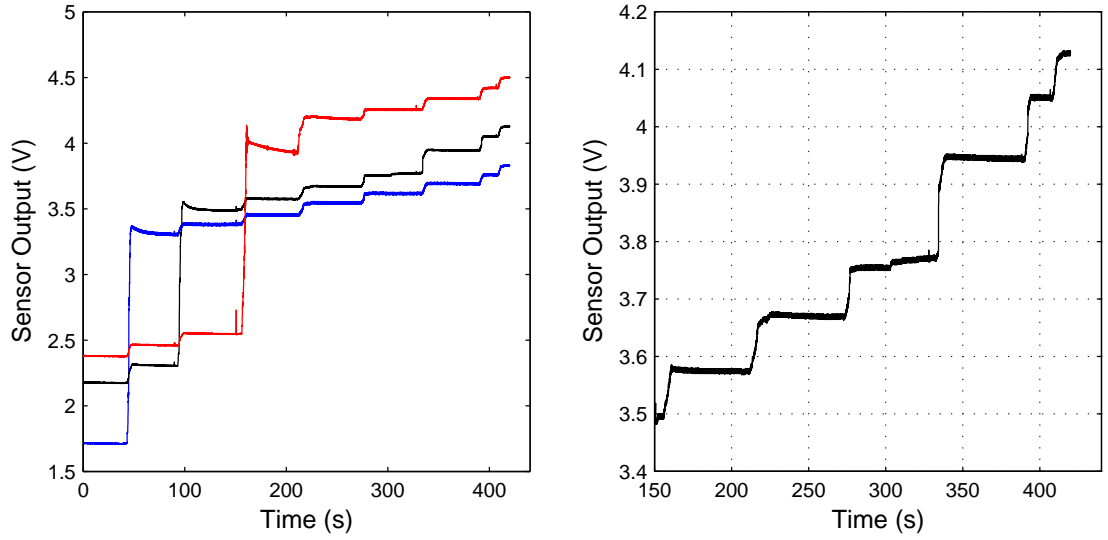
Figure 2.10: The sensor responses of 3 different CCP electrode pairs are shown on the left as the CCP was lowered incrementally into water. The right shows a closer view of one of these signals.

2.5 Current Working Prototype

The lessons learned from previous prototypes was that the use of AC was necessary, the sensors needed to be isolated, and nothing was apparently gained by switching from a Wheatstone bridge to a resistor divider network. Also, questions came to mind as to whether the common ground induced any cross communication between the electrodes. Therefore, the idea of using the sensor to unbalance a Wheatstone bridge has been carried over from the initial circuitry, a modification to isolate the sensors was made to the circuitry, and a two electrode approach was once again employed.

2.5.1 Physical Structure

The prototype CCP is constructed of acrylic glass as a stable, non-conductive unit. A small stainless steel tube is connected to the acrylic to enable the sensor to be

mounted into a deployment arm. The profiler consists of 8 electrode pairs comprised of 0.25 mm stainless steel wire. Each electrode pair is a conductivity sensor with the measuring portion of the electrode emerging slightly from one side of the sensor but being essentially flush with the acrylic (Figure 2.11). The use of stainless steel mitigates corrosion and is chosen as a cost-efficient alternative to platinum wires or platinization of the stainless steel. The electrode wire is shielded along its length except for the end that emerges from the acrylic. Thus, the unshielded portion is the circular cross-section of the stainless steel wire. The backside is made as slim as possible by gluing the wires in a single layer and covering them with silicone. The wires run up through the stainless steel tube and into a long section of Tygon tubing such that only the unshielded portion of the electrode is in contact with the sensing environment. The overall dimensions of the prototype CCP are 55.2 mm long x 9.6 mm wide x 6.6 mm thick. Each electrode pair is separated by 2.0 mm at the same elevation and adjacent electrode pairs are separated by 2.5 mm in the vertical (Figure 2.11).

The sensor was constructed by pre-drilling holes in the acrylic body of the sensor. Holes were drilled using an IC board as a guide. This ensured that each electrode pair had essentially the same separation and the same vertical spacing. The stainless steel wires were heat wrapped together and pulled through the stainless steel tubing. The individual wires were then pulled through the holes in the acrylic and the tubing and wires were glued to the acrylic body. After the glue cured, the wires were trimmed such that they were flush with the acrylic body. It was noted that the spatial relationship of electrodes in prior prototypes would change with use. This is because the electrodes protruded some distance away from the body allowing the wires to bend. Also, the coating on the wire would fray with use which changed the electrode geometry. Theoretically, the change in spacing and geometry of the electrodes would change how it responded in dynamic, small scale tests. The

trimming of the wire such that the electrodes were flush with the body attempts to eliminate these variables.
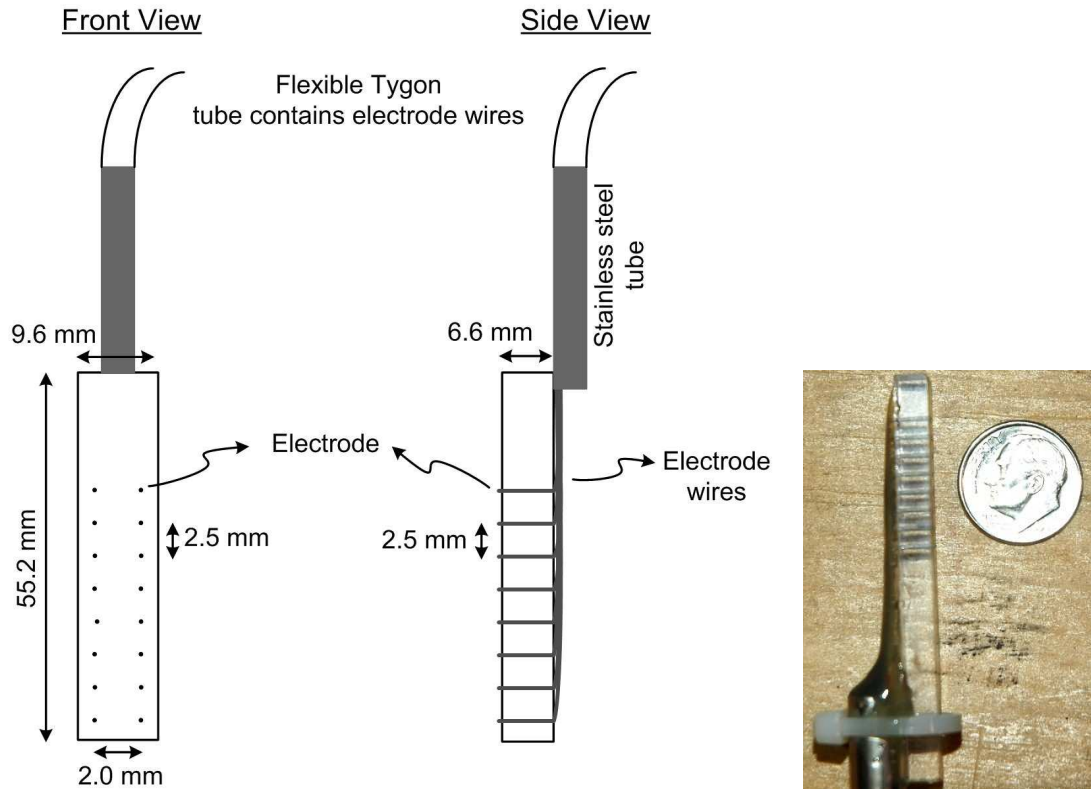
Figure 2.11: The most current CCP is shown in the photograph. The front view and side view schematic (not drawn to scale) of the Conductivity Concentration Profiler (CCP) is shown in the sketch.

An additional change in the physical nature of the sensor was making the sensor arm detachable from the circuitry. This not only promotes portability, but also better facilitates the creation of new physical sensors to both replace damaged sensors and to improve upon previous designs. The wires from the cables are connected to the coated wires running through the tygon tubing via a 25 pin D-SUB connection (only 16 pins are actually functional as there are two electrodes per 8

pairs). Also, the circuit board was placed in a waterproof box for protection and to promote portability (Figure 2.12).
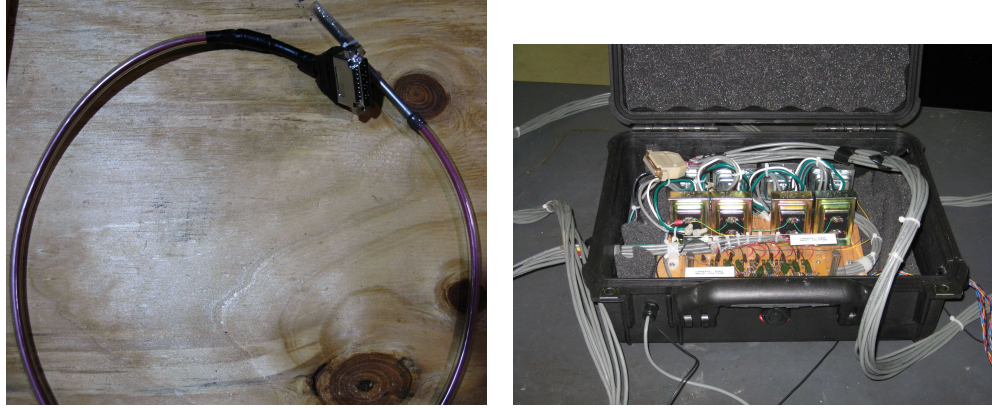
Figure 2.12: The actual sensor unit (left) is separated from the "black boxed" circuitry (right) to promote portability and allow the swapping of newly produced sensing units.

2.5.2 Circuitry Design

Figure 2.14 shows a wiring diagram for a single electrode pair. All other electrode pairs have the same configuration. A WAVETEK master oscillator provides an alternating current (AC) at V_{out} = 5 volts at 2.7 kHz. The AC mitigates electrolysis on one of the electrodes from each sensor pair that would occur with direct current (DC). A carrier frequency of 2.7 kHZ was used considering it yields a large dynamic range and a relatively stable signal. After generation, the AC passes through a series of 120V/16V EM57580 Zenith transformers to step up the voltage and isolate the current from each of the other electrode pairs, effectively eliminating the cross talk due to a shared AC signal. The voltage on the opposite side of the transformer is approximately V = 18 volts and supplies the input voltage to each respective bridge circuit. Each electrode pair is connected via cable to one leg of the Wheatstone bridge consisting of four 110 kΩ resistors. The output of the bridge

is connected to a full wave rectifier consisting of four 1N4148 switching diodes and a 0.22 μF filter capacitor with a 150 kΩ resistor connected in parallel to produce a full wave rectified signal (See Section 2.4.1) before logging on a DATAQ logger in differential mode at 16 Hz. On the opposite side of the active (electrode) leg of the bridge, a 0.47 μF capacitor is added to approximately balance the bridge with the electrode in air.

Unlike the DC analysis of the Wheatstone bridge described by Equation 2.9 the bridge elements are not purely resistive due to phase displacements in the AC case. Therefore the complex impedance must replace resistance in Equation 2.9. Placing an appropriate reactive element in a quarter of the bridge will ensure that magnitudes and *phases* of voltage at point B and D are the same (Figure 2.13).
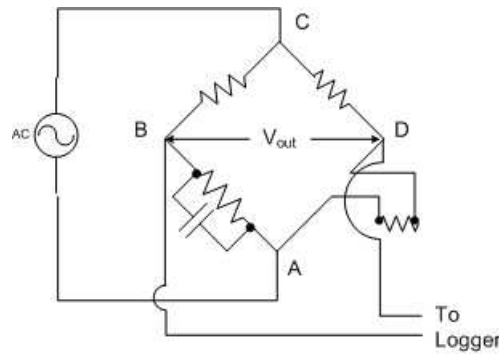
Figure 2.13: A schematic of a balanced AC Wheatstone bridge. A capacitor must be added to balance the bridge to account for phase.

In order to use the resistance of the fluid as detected by a pin pair to unbalance the bridge, a capacitor was placed in the bridge opposite the active (electrode) quarter of the bridge to attempt to balance the bridge when infinite resistance was supplied by the CCP. In other words, the capacitor acted to balance the bridge ($V_{out} = 0$) with the sensor in air such that the introduction of the sensor into water unbalanced the bridge to yield a voltage. A simple bench top test showed that, of

29

standard capacitors, a 0.47 μF capacitor most closely balanced the bridge. Due to imperfections in the circuitry components and ambient effects, the bridge is slightly unbalanced when infinite resistance is applied (sensor in air).
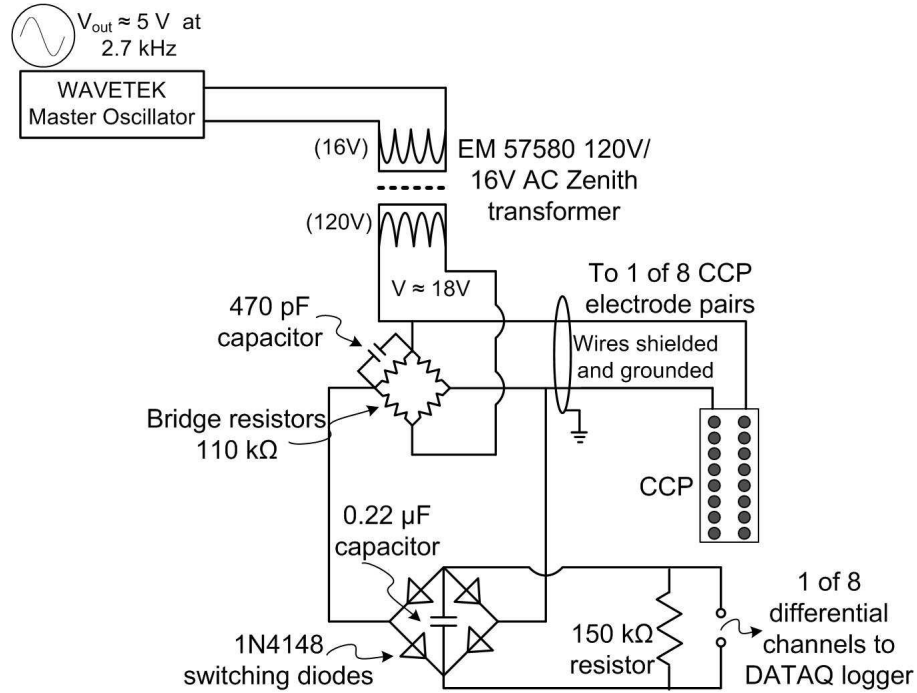
Figure 2.14: The current circuitry applies lessons learned from previous working prototypes in addition to a countless number of test sensors and circuitries.

2.6   Pertinent Sensor Properperties

2.6.1   Sensor Calibration

It has been well established in the previous sections that the sensor relies on a change in the resistivity/conductivity of a sand/water slurry to determine sediment concentration. Further, the greater the volumetric sediment concentration in the water, the lower the conductivity. However, resistivity/conductivity as a function of sediment concentration is not well established. Also, while the sensor response due

to changing resistance detected by an electrode pair can be analytically predicted via an AC circuit analysis, the actual sensor response is not so easily predictable. The ideal approach is to couple these two unknowns. In essence, the sensor outputs a certain voltage to the logger as a function of sediment concentration. Therefore, calibration curves are obtained by logging sensor responses to different known sediment concentrations. However, unlike salt or other electrolytes, sediments settle rapidly. Because of this, keeping a fixed concentration homogeneously mixed in a calibration vessel has proved to be beyond simple techniques (Figure 2.15). This makes the calibration of a conductivity/resistivity sensor for sediment concentration conceptually obvious, but practically non-trivial.

Figure 2.15: This photographs shows the difficulties in suspending sediment at a steady and uniform concentration in a calibration chamber.

There is little reference to a definitive calibration of conductivity-based sediment concentration sensors in the peer-reviewed scientific literature. Some researchers have used a tank with a stirrer or forced upward jet to suspend high concentrations of sediment (e.g. [30], [29]). At the instant a voltage measurement is recorded, a small amount of the fluid-sediment mixture is extracted to determine the sediment concentration. A calibration curve is developed after repeating this procedure for different sediment concentrations. The drawback to this approach is

that the calibration for a given concentration must be obtained at precisely the same instant a voltage is recorded unless the mixture is perfectly homogeneous in space and time. Due to this difficulty, other previous researchers have used a two point calibration. This simply uses conductivity/resistivity values obtained in a packed bed (the sediment concentration in the bed can be approximated from determined porosity of the sediment) and values obtained in clear water and fits a line between the two to obtain a calibration "curve." This technique assumes that the conductivity of a sand/water slurry is a linear function (F_{L1}) of sediment concentration

$$K = f(c) \rightarrow K = F_{L1}(c) \tag{2.10}$$

With this assumption, the calibration approach is decoupled and it is necessary to determine the response of the sensor (S) as function of conductivity.

$$S = f(K) \tag{2.11}$$

2.6.1.1 Sensor Response to Conductivity/Resistivity

Over a large range of resistivity the sensor response is nonlinear. However, the range of resistivity/conductivity from pack bed to clear tap water is relatively small. A test was devised to change the conductivity of a solution in small increments such that it resolved sensor response as a function of conductivity in this small range.

To achieve this calibration, a CCM was used as a conductivity meter. The CCM was calibrated with a standard conductivity solution. The premise that the conductivity of water is a function of (directly related to) temperature and chemical concentration was applied. The test started with about 20 fluid oz. of the lowest conductivity water which was obtained from the cold water tap of a drinking cooler. The drinking cooler water has less electrolytes than the tap water, hence lower conductivity. The conductivity was moderately increased by removing about 5 oz.

of cold drinking water and replacing it with 5 oz. of hot drinking water. The water was mixed in a cylindrical (0.37 m high, diameter = 0.11 m) vessel to ensure homogeneous properties. Then roughly 5 oz. of that mixture was replaced with 5 oz. of hot drinking water and again was well mixed in the vessel. In this way, the conductivity of the water was increased over several steps. For the higher range of conductivities, different temperatures of tap water were used. The CCP and conductivity meter were placed in the cylindrical mixing vessel with voltage readings taken at 16 Hz over 5 s durations for each of the different fluid conductivities. Mean values from the readings indicate that over the range of conductivities for sediment/water mixtures from 0.2 to 0.65 mS/cm the CCP response is linear (Figure 2.16). Two independent test were conducted on different days to show repeatability.
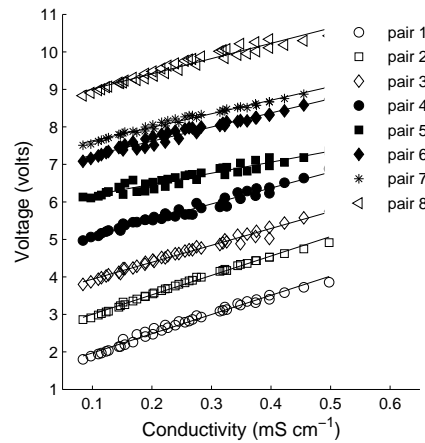
Figure 2.16: Calibration curves taken several days apart for each electrode pair. Data and the least squares solid line for each electrode are offset vertically by 1 volt for graphical clarity.

In all cases, the voltage (V) variability over each 5 s duration was less than 2.5 x 10^{-3} volts and the r^2 correlation coefficient for each electrode pair ranges between 0.91and 0.99 significant at the 99 % level. The linear fit slopes vary from 2.65 to 4.66 V / (mS/cm) and the y-intercepts range from 0.26 to 0.88 V. Slope and intercept

33

variability is likely due to slight differences in electrode pair spacing, the amount of unshielded electrode that is in contact with the mixture, and imperfections in the circuitry (e.g. the resistors are 5 % accurate). However, the fact that each electrode is calibrated independently and the fits are consistent from 2 different days of testing alleviates any difficulty with variation between the linear fits. Therefore, if conductivity is, in fact, a linear function of sediment concentration (Equation 2.10), and since sensor response has been shown to be a linear function (F_{L2}) of conductivity, sensor response is a linear function (F_L) of sediment concentration

$$S = F_{L2}(K) \rightarrow S = F_{L2}(F_{L1}(c)) \rightarrow S = F_L(c), \qquad (2.12)$$

and a two-point calibration for sediment concentration is sufficient.

2.6.1.2 A Crude Calibration with Sediment

Despite the difficulties in obtaining a homogeneously mixed sediment concentration, a calibration of the sensor at different sediment concentrations was attempted. This was attempted using a DC motorized mixer with a Teflon impeller stirring the sediment/water mixture in the cylindrical vessel described above. Calibrations were attempted for theoretical sediment concentrations of 0.06, 0.14 and 0.26 m^3/m^3 (Figure 2.17, but realized from visual observation that the concentrations were not homogeneous as a function of space and time, see Figure 2.15). To illustrate this variability, the CCP was extracted upward from the bottom of the chamber through the water column at 0.1 m intervals stopping to collect data for 5 s at 16Hz (Figure 2.17; mean values shown). For illustrative purposes, data are cast into sediment concentration using a two-point calibration rather than showing the data as raw voltage. In all cases, the individual calibrations cluster together, indicating the individual electrode pairs measure the same trends in concentration as a function of elevation.
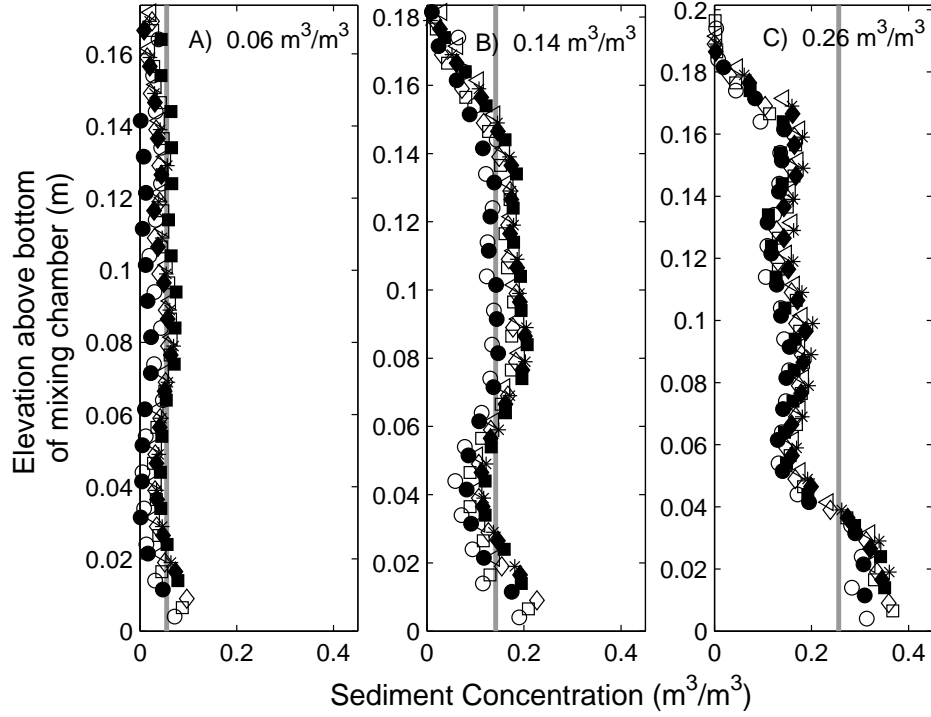
Figure 2.17: Calibration value as a function of elevation for each electrode pair of the CCP for three different sediment concentrations (A: 0.06 m3/m3; B:0.14 m3/m3; C: 0.26 m3/m3). The vertical gray line in each panel is the known sediment concentration. Symbols are as given in Figure 2.16

For the 0.06 m^3/m^3 case, the calibrated sediment concentrations are nearly equivalent to the known concentration in the chamber (gray lines in Figure 2.17) with little variability as a function of elevation. There is a slight curve in the profile near an elevation of 0.04 m, the elevation of the impeller blades. The low sediment concentration allows for the sediment to be essentially homogeneously mixed. When the sediment concentration increases to 0.14 m^3/m^3, the estimated concentration displays more variability as a function of elevation. Again the values for individual electrode pairs cluster together and are near the known sediment concentration.

Near the location of the stirrer, the concentration drops as sediment is mixed upward and downward due to turbulence. Near the free surface, the concentration drops to almost zero as a strong transition to essentially sediment-free water was observed. Finally, for sediment concentrations about half the packed bed limit, there is an increase over the known concentration by roughly 35 % due to mixer turbulence damping from the high concentration. Above the location of the impeller blades for most of the chamber, the concentration is nearly uniform, but incorrect by 38 %. Again near the free surface a well-defined layer of low sediment concentration is observed as the mixing turbulence is completely damped from the sediment in the water column.

2.6.2 Spatial Resolution

Spatial resolution is a critical parameter of the CCP in quantifying sediment concentration. On the one hand, too fine a spatial resolution is not desired because the electrode pair would essentially measure the presence or absence of only a few sand grains and the signal would be inherently noisy due to interstitial gaps and inhomogeneities in the concentration field. On the other hand, too coarse a resolution is not desired because it will overly-smooth the vertical profile and will blur any sharp gradients in concentration between the at-rest bed and above fluid or between the bedload and suspended load layer.

2.6.2.1 Theoretical Sensing Volume

Early experimental work on the dynamic response of a two-electrode conductivity probe suggested that roughly 99 % of the effective cell volume (CV) is contained within a sphere equal to the electrode spacing [39]. In that case the electrode diameter was 1 x 10^{-4} m. Hill and Woods (1988) presented a theoretical

approach in an effort to determine the spatial response of a two-electrode conductivity probe. They defined the electric potential, V_p, for two electrodes located an equal distance (+a, -a) from an origin (an electrode spacing of L = 2a) as

$$V_p = \frac{kq_1}{r_1} + \frac{kq_2}{r_2} \qquad (2.13)$$

where q_1 and q_2 are the electric charges, r_1 and r_2 are the radii from the charge locations and k is the electrostatic constant. The current flow between the electrodes must pass through a surface normal to the plane in which the electrodes are located. As an example, if the electrodes are located on the x-axis in the horizontal plane (x,y), the current must flow across the plane defined by coordinates (x = 0, y, z; shown as the gray line in two dimensional image in Figure 2.18). Integrating the current density $(\vec{j})$ over this planar surface $(d\vec{A})$ and assuming a homogeneous medium, the total current, J, passing between electrodes is

$$\vec{j} = K\vec{E} \qquad (2.14)$$
$$\vec{E} = -\nabla V \qquad (2.15)$$
$$J = \int_S K\vec{E} \cdot d\vec{A} \qquad (2.16)$$

$$J = 4\pi Kkqa \int_0^\infty \left(r^2 + a^2\right)^{\frac{-3}{2}} r\, dr \qquad (2.17)$$

where the charges are assumed to be of equal and opposite magnitude, q, $\vec{E}$ is the electric field and K is the conductivity of the medium. To determine the effective CV the integral in Equation 2.17 is decomposed into two parts [40] as

$$J = 4\pi Kkqa \left[\int_0^b \left(r^2 + a^2\right)^{\frac{-3}{2}} r\, dr + \int_b^\infty \left(r^2 + a^2\right)^{\frac{-3}{2}} r\, dr \right] \qquad (2.18)$$

where b represents the radial distance from the midpoint between the electrodes in the plane of the electrode pair. The ratio, J_b, between the first integral and the sum of both integrals in Equation 2.18 quantifies the effective CV as

$$J_b = -\frac{L}{\sqrt{4b^2 + L^2}} + 1 \qquad (2.19)$$
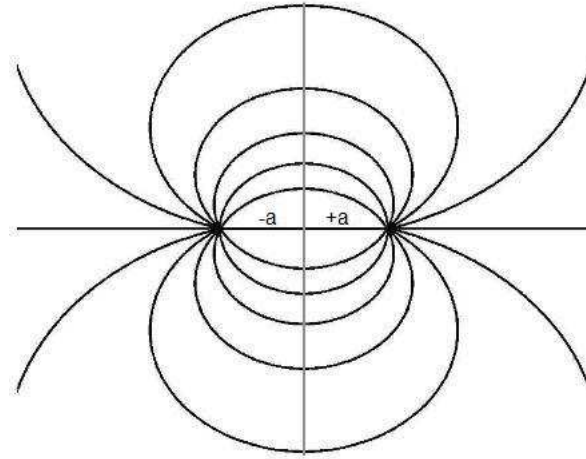
Figure 2.18: Lines of current flow for two electrodes of charge, q, a distance a from the origin. The vertical line is the plane between the electrodes that all current must pass through with a perpendicular orientation.

Figure 2.19 indicates that 55 % of the expected current flow occurs within a distance of b = 1, the electrode spacing. Ninety percent of the current flow occurs within a distance equal to 5 times the electrode spacing; 0.01 m for the prototype CCP based on this theory. It should be noted that Hill and Woods (1988) suggest the relevant volume is the volume within the lines of current flow that intersect the plane. Since this volume is not spherical, they conclude that the cell is primarily sensitive to conductivity fluctuations in the volume between the electrodes.
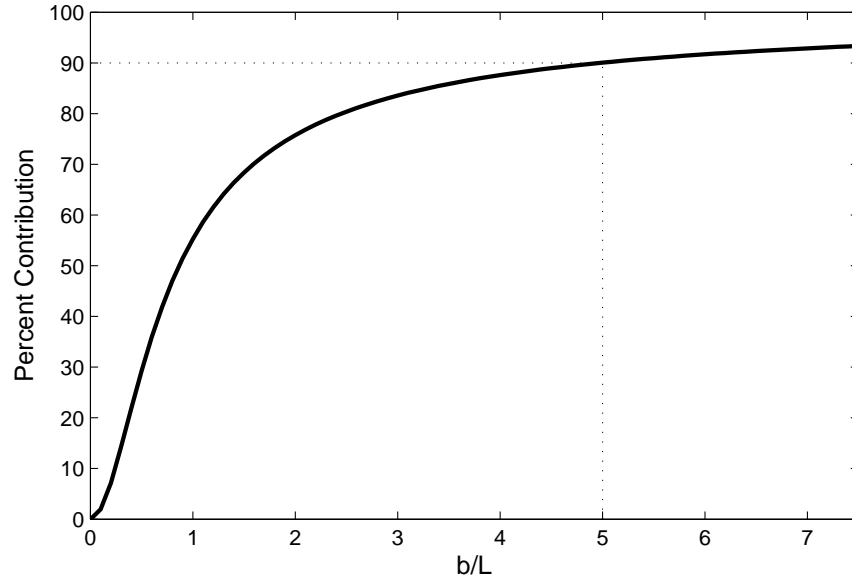
Figure 2.19: The relative current contribution from a spherical volume with radius, b compared to the total current (J_b expressed as a percent; Equation 2.19)

2.6.2.2 Experimental Approach

In the previous simplified approaches for estimating effective CV, necessary assumptions included a homogeneous conducting medium and a spherical electrode. Generally these assumptions are not valid. In the case of measuring sediment concentration, the conductivity of the medium changes considerably as a function of the relative concentration of water, sediment and air. In addition, the electrodes are not spherical but instead a circular cap of small but finite thickness (refer to description of the sensor where only the end of the electrode wire is unshielded). Thus, while the simplified theory provides one estimate of the spatial resolution, procedures were developed to estimate the resolution experimentally. Using previous experimental efforts as a guide [39], the sensor response was tested across an interface.

A sharp conductivity interface between fluid and air was created in the stirring vessel using isopropyl alcohol (isopropanol) with a minimal amount of dissolved sodium chloride. Isopropyl alcohol was used to reduce surface tension effects that were encountered when water was used as the fluid since water would readily adhere to the electrode pair when it was slightly above the fluid-air interface. The CCP was lowered through the interface at 0.001 m increments using a manually controlled stepper. At each stop, the voltage was recorded for 5 s at 16Hz (Figure 2.20). The voltage scale has been normalized between 0 and 1 using the lowest and highest readings representing air and fluid respectively. Profiles are intentionally not offset from each other to indicate similarity in the signal for all electrode pairs. It can be seen that the electrodes maintain a normalized voltage close to zero while in air and that there is an abrupt change in voltage as electrodes move across the interface. Once in the fluid mixture, the normalized voltages are nearly constant.

How well each electrode pair resolves the interface (assumed to be of infinitesimal thickness) yields an indication of the CV in the vertical direction, the direction of interest for sediment profiling capabilities. To determine the CV, the lowest elevation where the normalized voltage is below 0.05 (5 % of the normalized range) and the highest elevation where the normalized voltage is above 0.95 (95 % of the normalized range) are retained from each electrode pair. Taking the difference in these elevation values provides an estimate of the CV as $1.8 \times 10^{-3} \pm 2.5 \times 10^{-4}$ m (mean $\pm$ 1 standard deviation) from the 8 electrode pairs. As an example, for 2×10^{-4} m diameter sediment typical of many beaches, this would represent 7.5 - 10.5 grain diameters. It is anticipated that the actual CV is less than this value because the effect of surface tension could not be completely mitigated. Even using the isopropyl alcohol, some fluid adheres to each electrode pair causing a voltage reading higher than it should have been for a sensor that was deemed above the interface based on the experimental set up (visualize the meniscus for an adhering

fluid with a free surface in a cylinder). Nevertheless, this test indicates the electrode pairs can resolve several measurements in the vicinity of the at-rest bed based on the expected CV. Also, since the voltage registered by the electrode pairs drops off with radius squared according to electromagnetic theory, sediment grains closest to the electrode pair will have a larger impact on the recorded voltage than grains further away. Finally, this test indicates that for the profiler described here, electrode pairs should not be separated any closer than approximately 0.001 m if minimal overlap (smoothing) of signals is desired. If some smoothing of the vertical profile is acceptable, electrode pairs could have a vertical separation of perhaps 5×10^{-4} m , but any closer would be physically challenging due to the diameter of the electrode itself. Essentially, for the current CCP, the electrode spacing provides measurements at discrete vertical locations with no apparent overlap. For future sensors, the limit of the spacing is the physical fabcricating limitation rather than concern of overly smoothing the profile.
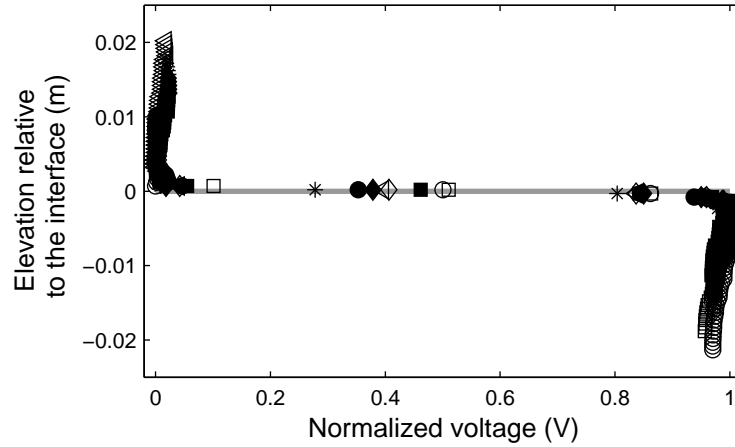
Figure 2.20: Experimental resolution test for each electrode pair across an isopropyl alcohol to air interface (the gray line). Symbols are as given in Figure 2.16

41

2.7 A Note on Cross Talk

Several bench top tests have shown that there is no detectable crosstalk resulting from electrode pairs interfering with one another. However, it has been observed that when recording multiple channels in differential mode on the DI-720 logger, a strong response in one channel induces small changes in other channels. A test was done to quantify this effect (Table 2.1).

The sensor was detached from the circuitry at the 25 pin D-sub connection and power was supplied to the circuitry. This state was logged for 5 seconds at 16 Hz. The values correspond to the voltage output of the bridge due to the slight imbalance from imperfections of circuitry components. A wire was used to short one of the sensors channels (no resistance), while the others were left open to air (infinite resistance). This was done for all eight channels, and each case was logged for 5 seconds at 16 Hz. Each of these signals were averaged over the entire sample for every case. The mean of the signal for the all open air case was subtracted off of the other signals to investigate the channel interference. The results are shown in Table 2.1. Shorting a channel resulted in roughly 0.12 V change in a neighboring channel.

Table 2.1: Inherent cross channel interference due to logger in differential mode? The entries indicate the voltage output change (relative to the case when all sensors are open to air) in each channel (columns) when a certain channel (rows) was short circuited.

	Δ Channel 1	" 2	" 3	" 4	" 5	" 6	" 7	" 8
Channel 1 Shorted	4.23	0.12	-0.00	-0.01	-0.02	-0.02	-0.02	-0.02
Channel 2 Shorted	-0.02	4.52	0.12	-0.01	-0.02	-0.04	-0.02	-0.02
Channel 3 Shorted	-0.02	-0.02	4.43	0.11	-0.03	-0.03	-0.03	-0.02
Channel 4 Shorted	-0.02	-0.02	-0.02	4.53	0.07	-0.02	-0.02	-0.03
Channel 5 Shorted	-0.02	-0.02	-0.03	-0.02	4.14	0.13	-0.01	-0.02
Channel 6 Shorted	-0.02	-0.03	-0.03	-0.02	-0.01	4.41	0.01	-0.01
Channel 7 Shorted	-0.02	-0.02	-0.03	-0.03	-0.02	-0.02	4.04	0.10
Channel 8 Shorted	0.06	-0.02	-0.02	-0.03	-0.02	-0.02	-0.02	4.23

The results of this test were somewhat troublesome as interference on the order of 0.10 V would introduce significant error in sampling. It was of interest to see if the cross interference scaled with the magnitude of the voltage change in the channel of interest. Therefore, a single two electrode test sensor was fabricated to replicate an electrode pair of the CCP. Instead of shorting each channel with a wire, the sensor was connected to each channel and the electrodes were placed in a cup of water. The results are shown in Table 2.2. The cross channel interference scales with the magnitude of voltage change as the interference is roughly 0.04 V in this case. This represents the worst case scenario when one electrode pair is in water and the others are dry. In this case the sensor interference would yield a signal that is much less than that of the packed bed. Therefore, it would still be determined that the sensor was dry even with this cross talk. Therefore, the cross talk between channels with different signals at different sediment concentration is likely to be on the order of noise and other implicit error.

Table 2.2: The cross channel interference scales with the magnitude of sensor response. The entries indicate the voltage output change (relative to the case when all sensors are open to air) in each channel (columns) when a certain channel (rows) was placed in water.

	Δ Channel 1	" 2	" 3	" 4	" 5	" 6	" 7	" 8
Channel 1 Water	1.24	0.04	-0.00	-0.00	-0.01	-0.01	-0.01	-0.01
Channel 2 Water	-0.01	1.37	0.04	-0.00	-0.01	-0.01	-0.01	-0.01
Channel 3 Water	-0.00	-0.01	1.35	0.04	-0.01	-0.01	-0.01	-0.01
Channel 4 Water	-0.00	-0.00	-0.00	1.46	0.02	-0.01	-0.01	-0.01
Channel 5 Water	-0.01	-0.01	-0.01	-0.01	1.32	0.05	-0.00	-0.00
Channel 6 Water	-0.00	-0.01	-0.01	-0.01	0.00	1.45	0.03	-0.01
Channel 7 Water	-0.01	-0.01	-0.01	-0.01	-0.00	-0.00	1.17	0.03
Channel 8 Water	0.021	-0.00	-0.01	-0.01	-0.00	-0.00	-0.00	1.29

Chapter 3

EXPERIMENTAL DESIGN

Due to the difficulty associated with nearbed measurements and measurements in the swash zone in general, it is desirable to start by analyzing measurements in the best controlled laboratory set-up. The data obtained from swash events of individual, solitary waves generated in a laboratory flume are theoretically the easiest to analyze. In a well-controlled setting, complications due to swash-swash interactions are eliminated and repeatability between consecutive tests is more achievable. While on a real beach waves are highly irregular and this simplified approach fails to replicate the morphodynamics on sandy beaches, it allows for the validation of measurements based on simple observations. If measurements are validated in the simplest case, the same set up can be used under more complex forcing (i.e. irregular waves in the lab and eventually field studies). Figure 3.1 shows the logical progression of experimentation. The work described in this thesis represents the first necessary test case in this progression.
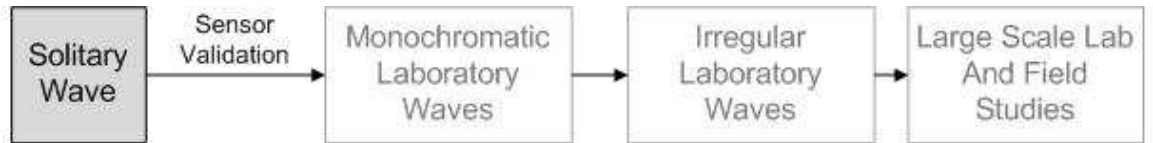
Figure 3.1: The schematic shows the logical progression of experimentation. The measurements described in this paper represents simplest test case.

The information contained within this chapter describes the details of the experimental set-up, instrumentation used, in situ calibration techniques, and some difficulties that were encountered.

3.1 Precision Wave Flume

In preliminary tests, sensors were deployed in the large Tow Tank in the basement of DuPont Hall at the University of Delaware. Most sediment transport studies at the University of Delaware had been conducted in the Tow Tank. However, another experiment being run in this tank and other factors (mentioned in Section 3.2) impeded on the control that is necessary to conduct the solitary wave experiments.

The best available setting for the experiment was the Precision Wave Flume located in the Center for Applied Coastal Research (CACR) laboratory at the University of Delaware. This flume is dimensionally much smaller than the Tow Tank with a length of 33 m but a cross-section of 0.6 m (width) by 0.76 m (depth). The Precision Wave Flume has a piston type wave maker. Sixty percent of its length consists of glass sidewalls aligned within an accuracy of 5 x 10^{-4} m. This feature along with its length helps ensure longshore uniformity in the wave as it propagates down the tank. This is one improvement over the Tow Tank whose sidewalls are much less precise. However, the Precision Wave Flume had never been used in sediment transport studies and therefore no sand had ever been in the tank. Because of this, no previous set-up could be followed exactly and, therefore, the design considerations were a pertinent component of the research experiment.

3.2 Sand

The first task necessary to set up the experiment was finding a source of sand to be placed in the flume. This was further complicated by an unforeseen difficulty due to a concentration of fines contained in a sediment sample. Fine sediments, i.e.

clays, carry surface charges (e.g. [41]). Again, the assumption is that the sediment is solely resistive, however fines are not concurrent with this assumption. The effects of fines were clearly evident. In the case when a small concentration of sand containing fines was suspended in the water column, the fines dominated the signal causing an *increase* in conductivity at low sediment concentrations.

A sieve analysis of the sand from the Tow Tank showed that 3.3% of the sample was finer than the No. 200 sieve which represents the lower limit of the sand regime. This relatively large concentration of fines proved to be problematic during calibration attempts with Tow Tank sand.

Therefore it was necessary to obtain silt/clay free sand. Sediment which was formerly used in a circular basin that was located in the CACR lab was selected as the source of sediment for the experiment. However, just like the Tow Tank sediment, a significant concentration of fines were contained in this sediment. When a sample of this sediment was dropped in a cup of water, the fines remained in the water column (Figure 3.2). The increase in conductivity from clear tap water to water contaminated with fines was 0.360 mS/cm to 0.395 mS/cm.
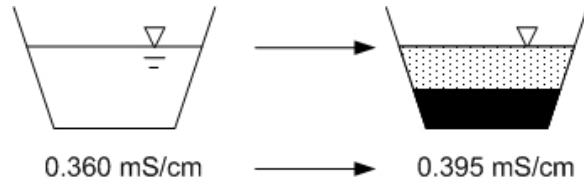
Figure 3.2: Sketch showing the effect of the silt/clay content in a sediment sample.

To rid the sand of the problematic fines, a washing technique was developed. A precision woven polyester mesh with 0.025 mm opening size, which is the same as a No. 200 sieve, was used. This mesh was stretched across a wooden frame essentially creating a large No. 200 sieve (roughly 1 m x 0.7 m). A volume of dry sand was placed on the sieve and was rinsed for 5 to 10 minutes allowing the water

to drain through the sand washing away the fines (Figure 3.3). After each portion was washed it was dropped through a cup of water to ensure the voltage increase due to the fine content was negligible. The washed sand was then placed in the flume.

Figure 3.3: This photograph shows the sand washing process. The arrows point to the fines that had passed through the sieve.

After the sand was washed, a sieve analysis was conducted. Table 3.1 and Figure 3.4 show the results of the sieve analysis. From these results important properties of the sediment size distribution were calculated.

The median grain size (d_{50}) was found to be 0.44 mm. The standard deviation of the grain size distribution (σ_ϕ) was calculated by

$$\sigma_\phi = \log_2 \sqrt{\frac{d_{84}}{d_{16}}} = \log_2 \sqrt{\frac{0.72}{0.26}} = 0.73, \tag{3.1}$$

where d_{84} and d_{16} is the diameter that 84% and 16% of the sample is finer (by weight), respectively. This σ_ϕ corresponds to a decently well-sorted grain size distribution.

The skewness of the distribution (α_ϕ) was then calculated by

$$M_{d\phi} = \frac{-\log_2 d_{84} + \log_2 d_{16}}{2} \qquad (3.2)$$

$$= 1.21 \qquad (3.3)$$

$$\alpha_\phi = \frac{M_{d\phi} + \log_2 d_{50}}{\sigma\phi} \qquad (3.4)$$

$$= 0.04, \qquad (3.5)$$

where $M_{d\phi}$ is the mean ϕ grain size (*phi scale*; $\phi = -\log_2 d$).

The positive skewness indicates that grains smaller than the mean grain size (0.43 mm) are slightly more prevalent. Relative to the Tow Tank sand, the sediment used in the experiment is far coarser. The scaling problem of laboratory sediment transport studies is worse in the case of the coarser sediment. However, for the purposes of the experimentation conducted the washed sand was more suitable not only because it contained a negligible concentration of fines but the sediment was transported almost solely as bedload/nearbed transport.

Table 3.1: Results from the sieve test.

Sieve #	Opening Size (mm)	Mass Retained (g)	Percent Finer
10	2.000	0	99.8
20	0.841	17	95.2
40	0.420	180	46.1
60	0.250	114	14.8
100	0.149	46	02.2
140	0.105	7	00.3
200	0.074	1	00.0
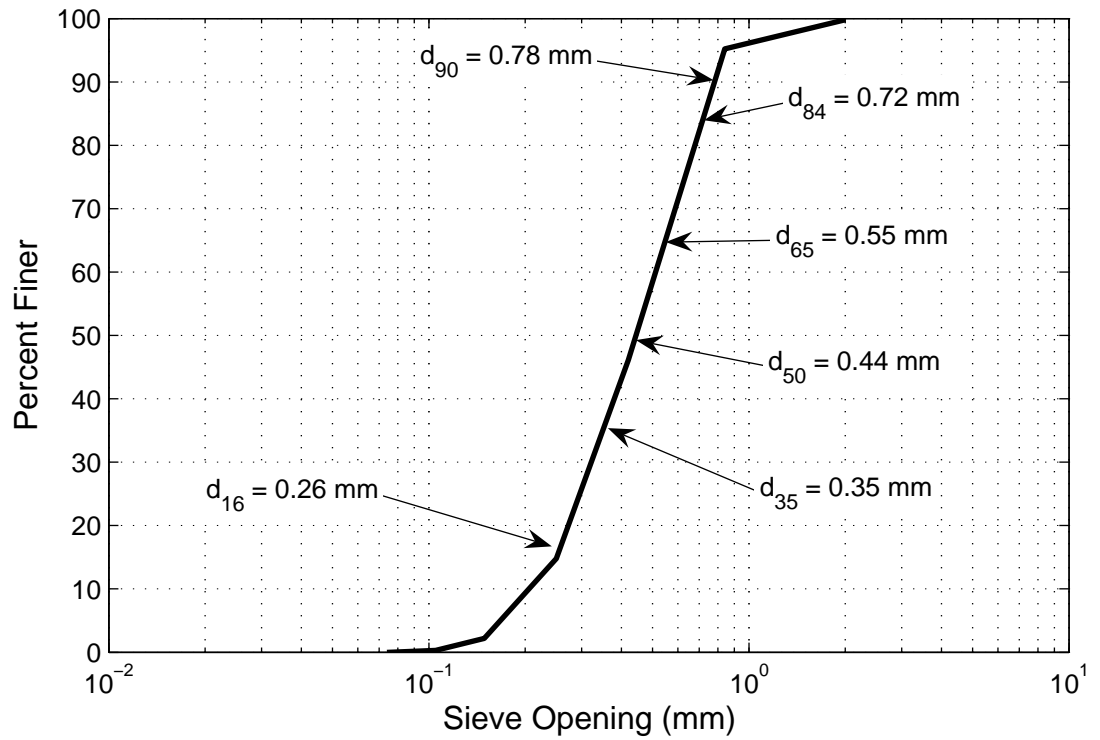
Figure 3.4: The grain size distribution of the washed sand from the data obtained from a sieve test (Table 3.1).

3.3 Wave Design

Since there is a lower limit in the forcing that is required to move sand, the limits induced by working in a smaller flume with coarse grains necessitated careful design of the solitary wave being driven. There were three main constraints that influenced the design of the wave:

(1.) Enough forcing to drive measurable sediment transport.

(2.) Not so large that the wave overflows the depth of the tank.

(3.) Limit uprush such that the sandy profile is not overwashed.

To achieve the desired wave, analytical solutions and empirical formulas were used as a guide. The design was tested before the beach was made to ensure the above criteria was met.

3.3.1 Analytical Solution: Wave Maker Theory

A solitary wave consists of a form entirely above the still water level (SWL) and is infinitely long. The solution of Boussinesq (1872) [42] for a solitary wave is given by

$$\eta(x,t) = H\mathrm{sech}^2 \sqrt{\frac{3}{4}\frac{H}{h^3}}(x - w_c t) \tag{3.6}$$

where x is the cross-shore coordinate, t is time, H is the wave height, h is the water depth, and w_c is the wave celerity given by

$$w_c = \sqrt{g(h + H)} \tag{3.7}$$

The governing equation underlying wave generation is a kinematic boundary condition, which states that the paddle velocity must match the water particle velocity due to the desirable surface wave at all elevations along the paddle.

$$x - \zeta(z,t) = 0 \tag{3.8}$$

$$\frac{d(x - \zeta(z,t))}{dt} = -\zeta_t + u - \zeta_z w = 0 \quad \text{at } x = \zeta, \tag{3.9}$$

where u and w are the horizontal and vertical components of fluid velocity, respectively and ζ is the horizontal position of the paddle. For a piston type wave maker, $\zeta_z = 0$ the boundary condition reduces to

$$\frac{d\zeta}{dt} = u(\zeta, t) \tag{3.10}$$

50

Unlike deep water sinusoidal waves, long wave velocity profiles are roughly constant with depth so the depth averaged water particle velocity $\bar{u}(x,t)$ is taken to be the representative water particle velocity. It has been shown, using continuity, that the mean velocity induced by permanent form waves is

$$\frac{d\zeta}{dt} = \bar{u}(x,t) = \frac{w_c\eta(x,t)}{h + \eta(x,t)} \tag{3.11}$$

In 1978, Goring solved for the paddle displacement for a wave of an arbitrary form before applying the solitary wave solution. The general solution for a wave whose form at the paddle position is

$$\eta(\zeta,t) = Hf(\theta)$$

where

$$\theta = k(w_c t - \zeta) \tag{3.12}$$

is given by

$$\theta^{i+1} = \theta^i - \frac{\theta^i - kct + \frac{H}{h}\int_0^{\theta^i} f(w)dw}{1 + \frac{H}{h}f(\theta^i)} \tag{3.13}$$

where the superscript denotes the iteration number and w is a dummy variable for integration. With θ solved for at each given time, the paddle displacement (from Equation 3.12) is given by

$$\zeta = w_c t - \frac{\theta}{k} \tag{3.14}$$

For a solitary wave, the wave function is

$$f(\theta) = \mathrm{sech}^2\theta \tag{3.15}$$

where $k = \sqrt{\frac{3}{4}\frac{H}{h^3}}$ (from Equation 3.6 and Equation 3.12). Substitution of the solitary form into the general iteration given by Equation 3.13 yields

$$\theta^{i+1} = \theta^i - \frac{\theta^i - kw_c t + \frac{H}{h}\tanh\theta^i}{1 + \frac{H}{h}\text{sech}^2\theta^i} \tag{3.16}$$

Though the free surface displacement of the solitary wave (η) approaches zero as t approaches $\pm\infty$, the practical definition of the time at which $\eta \approx 0$ to within three significant figures is

$$\pm t_0 = \pm\frac{3.80}{kw_c}$$

The maximum paddle displacement or stroke (P) as time approaches the infinite limit is

$$P = \sqrt{\frac{16}{3}\frac{H}{h}}h \tag{3.17}$$

The duration of the paddle stroke τ is computed by the times at which the trajectory of the solitary wave tails intersect the paddle trajectory $\zeta(t)$ and is given by

$$\tau = 2t_0 + \frac{P}{w_c} \tag{3.18}$$

Note that based on the definition of the solitary wave given by Equation 3.15, the origin of displacement $\zeta = 0$ and time t occurs under the wave crest. Also notice that a solitary wave of any height H can be generated depending only on water depth h [43]. Because of this, design consideration (2.) is easily met so long as design wave height plus the water depth does not exceed the depth of the tank (D). A factor of safety $SF > 1.0$ must also be used to account for shoaling.

$$(H + h)SF < D \tag{3.19}$$

The second limiting factor on the wave, as described by design consideration (3.), was dictated by the previous experiment conducted in the tank. A vertical wall had been constructed in the flume 22.7 m away from the paddle. The top of this barrier would eventually be used as upper limit of the sandy profile. The height

of this wall from the bottom of the flume was $D_{\text{eff}} = 0.67$ m. Therefore it was necessary that the run up did not breach this limit. If run up (R) is defined as the height of maximum wave uprush relative to the SWL, the limit of run up is given by

$$R + h <= D_{\text{eff}} \rightarrow R_{max} = D_{\text{eff}} - h \tag{3.20}$$

An empirical relationship to determine run-up due to a solitary wave based on a thorough set of laboratory experiments by Synolakis (1986) [44]

$$\frac{R}{h} = 0.918\frac{H^{0.606}}{h}, \tag{3.21}$$

was used as the governing equation for the wave height at a selected water depth.

The SWL was chosen such that depth was sufficient for a wave to propagate far away from the paddle before breaking and low enough to drive a large wave height. A design water level of 0.42 m was chosen. Once a water depth was selected, the maximum wave height could be determined (from the run up limit given by Equation 3.20 as determined by Equation 3.21), and the wave can be generated from the established wave maker theory.

$$(\frac{1}{.918}\frac{R_{max}}{h})^{\frac{1}{.606}}h = H_{max} \approx 0.205m \tag{3.22}$$

With these parameters (H and h), the paddle position as a function of time was solved using the iterative method described in Equation 3.16 in Matlab. To do so, the time step used was 50 Hz as that is the rate at which the wave maker reads an input file. The time vector, t, ranged from $-\frac{1}{2}\tau \le t \le \frac{1}{2}\tau$, with τ given by Equation 3.18 such that the paddle surged shoreward from a negative displacement. Initially, the paddle was programmed such that it was *slowly* drawn back to its initial negative displacement as to not significantly disturb the water surface. After surging forward the paddle was drawn *slowly* back to a displacement of zero as to

not generate a negative solitary wave (Figure 3.5, left). The stroke $P = 0.653m$ and duration $\tau = 2.32s$ of the surge were calculated from Equations 3.17 and 3.18, respectively. A factor of -18 was necessary to convert from displacement in meters to the corresponding voltage for the wave maker.
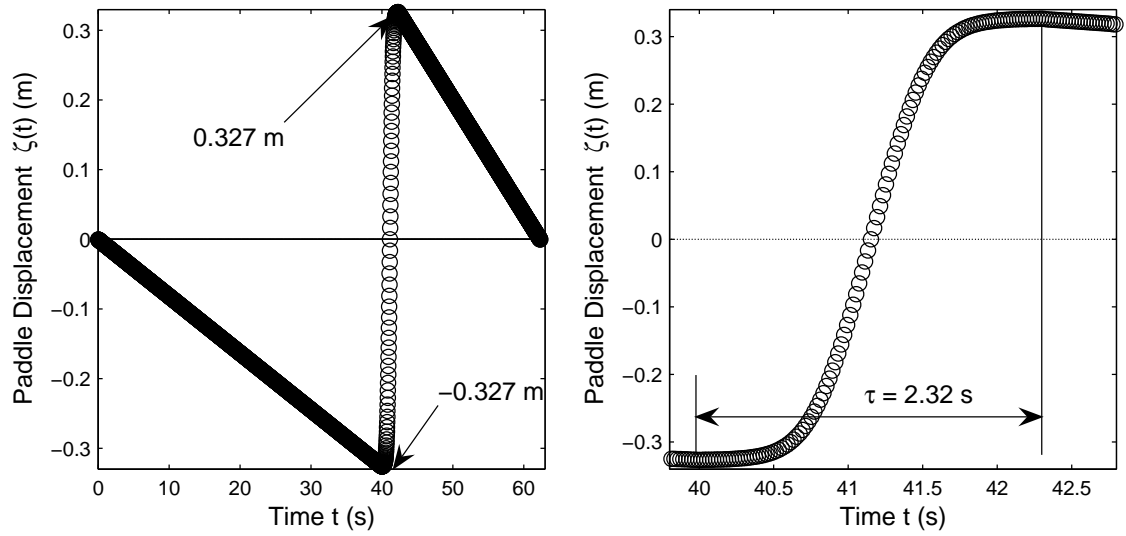
Figure 3.5: The left plot shows the entire time series of the paddle displacement. The right plot is a zoom to show the shape of paddle displacement for the surge that generates the wave.

This wave was tested to ensure that the swash run-up would not overwash the sandy profile and to ensure that the wave was forceful enough to move sand in the swash zone. To do so, the water level was raised to the design depth of 0.42 m, a small amount of sand was placed on the profile from the previous experiment and the wave was generated. It was observed that the uprush reached but did not breach the upper limit of the profile (as predicted by Equation 3.21) and there was significant sand motion.

54

3.4 Profile Design

The ultimate goal was to retrofit the existing geometry of the profile with a sandy beachface with a 1/12 slope. The existing profile consisted of a constant depth region that extended about 9.5 m from the paddle. At this point, a 1.22 m long section of Corian$^{(R)}$ is placed at a slope of 1/14.8. The slope that follows also consists of Corian$^{(R)}$ segments but are placed at a slope of 1/34.2.

Rather than laying a 1/12 slope directly on the existing slope, it was necessary to ensure that the sand was deep enough because the concentration sensors were to be deployed from underneath the bed (see Section 3.5.2.1). Therefore, three sections of the Corian$^{(R)}$ were removed and replaced with wooden platforms. Initially only two sections were removed and a foot long cut out in the platform was designed for the deployment of the sensors. Later the additional section was removed and another platform was designed such that sensors could be deployed at more locations along the beachface. Forms that lied upon the fabricated platforms and the 1/34.2 slopes to create 1/12 slope were placed along each wall of the flume. One form was made of sections of acrylic glass so that visual observation could be made while the other was sections of plywood.

Figure 3.6: This is the experimental beach profile (not drawn to scale). WG represents the location of the offshore gage. x is measured from the intersection between the SWL and beach profile. The solid line represents the rigid bottom while the dashed line represents the sandy slope. The faint dotted line was the existing beach profile before changes were made.

After the profile was retrofitted with the desired geometry, the washed sand was placed in the flume. A wooden 2" x 4" was used to smooth the sandy profile across the forms (Figure 3.7). A level was placed across the smoothed profile to ensure longshore uniformity. The result was a composite profile with a mild sloping rigid surf zone with a steep sandy beachface.

Figure 3.7: The profile was smoothed manually across the 1/12 forms. The profile was reset this way before every set of waves.

3.5   Instrument Array

In the swash zone, measurements of swash depth, velocity, and sediment concentration were made at the same cross-shore location over a series of waves. For different sets of waves, this cluster of instruments was moved to different locations on the beachface to make measurements in different portions of the swash zone.

3.5.1   Swash Depth

A capacitance wave gage was used to determine the local swash depth. The wave gage was buried about 0.05 m into the bed and the profile was smoothed locally around the gage. In order to calibrate the wave gage, the water level was raised such that the wave gage was submerged. The water level and voltage output of the wave gage were recorded. The water level was lowered in 0.005 - 0.01 m increments and corresponding voltages were recorded until the water level was below the sensor line. A typical result from a calibration of the buried wave gauge is shown in Figure 3.8. This calibration was done every time the beach profile was smoothed.
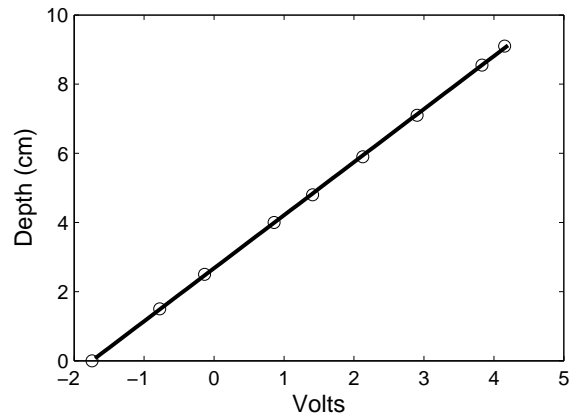
Figure 3.8: This is a typical example of a buried wave gage calibration curve. The wave gage voltage output is linear with depth

The offshore wave gage is also a capacitance type wave gage. It is located 10 m from the wave maker as shown in Figure 3.6. This wave gage was on an instrument cart and was attached to a stepper motor. Rather than a manual calibration, once the still water level was established, a LabView program ran the calibration. The stepper motor lowers the wave gage into the water in 0.01 m steps. The program automatically logs the calibration data. The offshore wave gage is the only instrument that was not logged on the local logger. This data was logged by the computer that ran the wave making program. The calibration is automatically applied, therefore data obtained from the offshore wave gage required no manual calibration nor additional treatment.

3.5.2 Sediment Concentration

To measure sediment concentrations the CCP (described thoroughly in Chapter 2) was used in addition to 3 CCMs (described briefly in Chapter 2). The calibration technique for the CCP has been well described. For the CCMs, the calibration is straight forward. The CCM can be set to measure conductivity in two ranges, 0 - 3 mS/cm or 3 - 60 mS/cm. Since the conductivity of the tap water used in the flume was roughly 0.4 mS/cm, the CCMs were always kept in the 0 - 3 mS/cm setting. The voltage output of the CCM is from 0 to 10 Volts corresponding to 0 and 3 mS/cm, respectively. The conductivity, K (in mS/cm), of solution as measured by a CCM is given by

$$K = \frac{V_{CCM}}{10} 3$$

where V_{CCM} is the voltage output of the CCM. The CCM output can be adjusted using fine and coarse adjustment knobs. A standard conductivity solution (0.4471 mS/cm at 20°C) was used to calibrate each CCM using the adjustment knobs.

Like the CCP, the CCM was calibrated for the determination of sediment

concentration assuming that conductivity varies linearly with sediment concentration. Just like the wave gage, the concentration sensors were calibrated in situ each time the profile was reset and a new set of waves was ran. To do so, the sensors were buried by hand and data was collected for 5 seconds at 16 Hz. The sensors were then uncovered such they were in clear water and data was collected for 5 seconds at 16 Hz. This cycle was repeated such that 5 - 10 records each for packed bed conditions and clear water conditions were recorded. Assuming a porosity of 0.35, the concentration in the packed bed was assumed to be 0.65 m^3/m^3. The averages of the voltage output for all water tests (V_{wat}) and of all packed bed tests (V_{bed}) were obtained for each sensor (the 3 CCMs and 8 sensors of the CCP) individually for the following calibration for sediment concentration, c, corresponding the sensor reading, V

$$c = \frac{-0.65m^3/m^3}{V_{wat} - V_{bed}}V + \frac{0.65m^3/m^3}{V_{wat} - V_{bed}}V_{wat} \tag{3.23}$$

3.5.2.1 Deployment

As previously mentioned, the CCPs and CCMs were deployed such that they came through the bed. To accomplish this, an aluminum bar was fabricated to hold the three CCMs and the CCP at fixed distances from one another (Figure 3.9). This arm laid horizontally below the bed with the sensors pointing upward. The end of the bar was attached to a vertical rod which was attached to a manually controlled stepper.

The sensors are placed in pre-drilled holes in the arm such that they are offset in the vertical. The sensor heights relative to the others was measured using a digital micrometer with 0.01 mm precision. When the sensors were placed in the flume, a circular level was used to ensure that the arm holding the sensor was level.
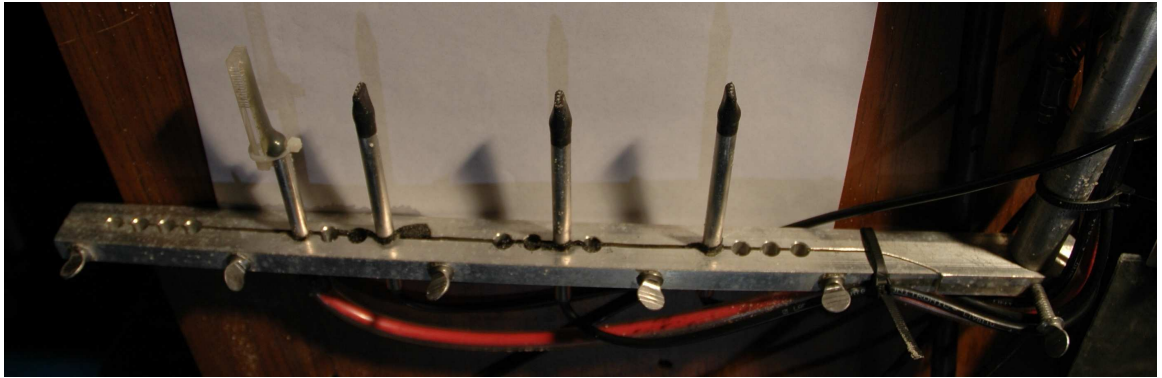
Figure 3.9: The CCP and CCMs are held in position by a horizontal arm which lies below the bed.

3.5.2.2 A Note of Drift

A major concern was that drift may effect the CCP reading during a swash event. The effect of drift was investigated in the tank. Power was applied to the CCP as the water level in the tank was being raised. The moment the CCP was wetted data were collected for several minutes. The drift was such that the voltage dropped as much as 1.3 V over the first 6 minutes of being submereged (Figure 3.10, left). The water level was left high such that the CCP was submerged without power being applied over night. The next day, before the in situ calibration, a second "drift" test was conducted. After soaking overnight, the CCP was unaffected by drift as voltage was essentially constant over time (Figure 3.10, right). Therefore, it is expected that drift effects were minimal during each swash event.
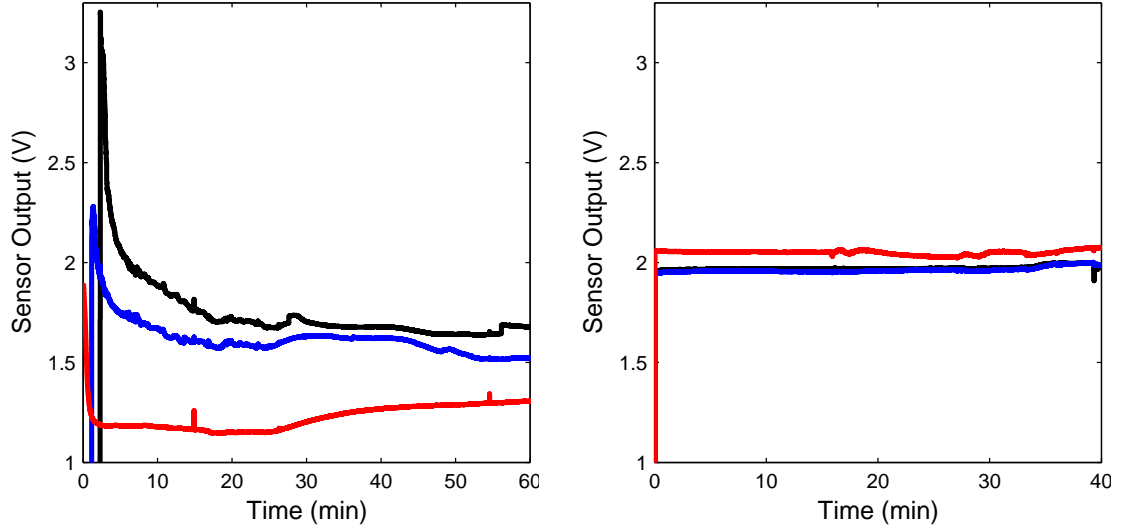
Figure 3.10: The left plot shows the entire time series of drift of three representative CCP sensors (denoted by different colors) as the sensors were being submerged. The right plot shows the time series of the same CCP sensors in water after soaking for several hours. This represents a typical observation.

3.5.3 Velocity

EMCMs were used to measure swash velocity. A set of two sensors, staggered 0.02 m in the vertical, was deployed. Unlike the other sensors in the array, the EMCM required no additional calibrations. They are calibrated by the manufacturer to output a voltage equal to the velocity (m/s). However, the closest proximity to a boundary, i.e. sea bed, that an EMCM can be placed and still output reliable data is uncertain. To test this, the EMCMs were placed in a steady, uniform, open-channel flow generated by a recirculating flume. The velocity was logged for 20 seconds at 16 Hz at different elevations relative to the bottom. A sharp decrease in measured velocity occurred between 20 mm and 03 mm above the bed (Figure 3.11). It is not certain whether this is an actual effect due to a boundary layer or if it represents

61

a sensor error due to its close proximity to the bed. Based on these tests, there is confidence in EMCM measurements at all elevation higher than 20 mm from the bed.
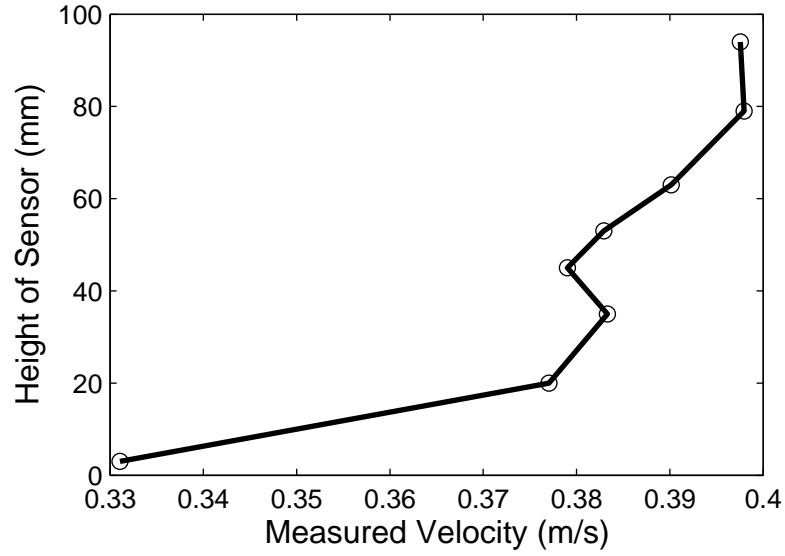
Figure 3.11: The plot shows velocity measurements by an EMCM at different elevations in a steady, uniform flow relative to a boundary.

3.5.3.1 Independent Measurements

A difficulty arose due to the CCMs interfering with the EMCMs. The CCMs disturb the electromagnetic field of the EMCMs such that when the CCMs are turned on and are in the same local area of the water column as the EMCM, the EMCM signal is noisy and obviously erroneous. Figure 3.12 shows a comparison between a velocity signal with and without CCM interference.
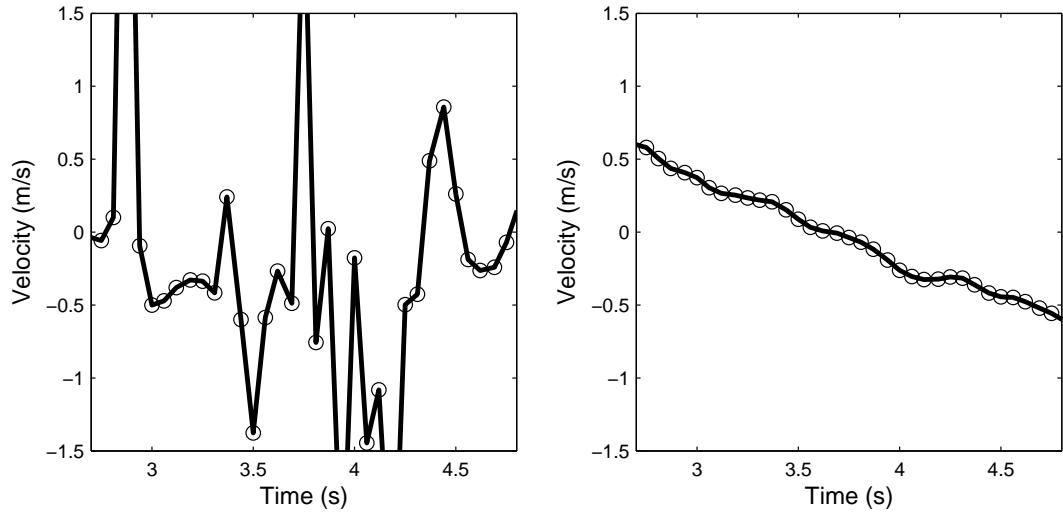
Figure 3.12: The left plot shows a noisy velocity signal from an EMCM due to CCM interference. The right plot shows the velocity signal from an EMCM without power supplied to the CCMs.

Because of this problem, velocity signals were collected independently of the concentration signals. To do so, the profile was smoothed to the planar 1/12 slope. The EMCMs were placed and the depth wave gage was buried at the cross shore location where concentration signals had been collected. The EMCMs were positioned vertically such that the lower EMCM was roughly 0.02 m above the bed. After calibrating the buried wave gage and establishing the water level at 42 cm, 10 individual solitary waves were generated. For each wave, velocity from both EMCMs, swash depth from the depth wave gage, and the offshore profile from the offshore wave gage was collected. Throughout the test the EMCM height was lowered in an attempt to ensure the lower velocity signal was about 0.02 m above the bed as the bed eroded locally at the sensor location.

3.5.4 Profile Measurements

A Leica DISTO^{T}M D2 laser distance meter (1.6 mm precision) was used to measure the beach profile as it evolved throughout a set of waves. The distance meter was suspended from one of the instrument carts that run the length of the flume. The cart was moved in 0.05 to 0.10 m increments and the distance from the laser meter to the bed was recorded to obtain bed elevations relative to the SWL.

Chapter 4

IDEAL EXPERIMENT AND RESULTS

The original experimental approach was to use the CCMs as a means to validate the CCP signal. The arrangement of the sensors shown in the sketch below was such that the CCMs were offset in the vertical and spanned part of the vertical measuring length of the CCP. This allows a three point profile measured by the CCM to be compared with the 8 point profile collected by the CCP. Assuming longshore uniformity, the concentration profiles obtained by the CCMs should agree with the profile obtained by the CCP.
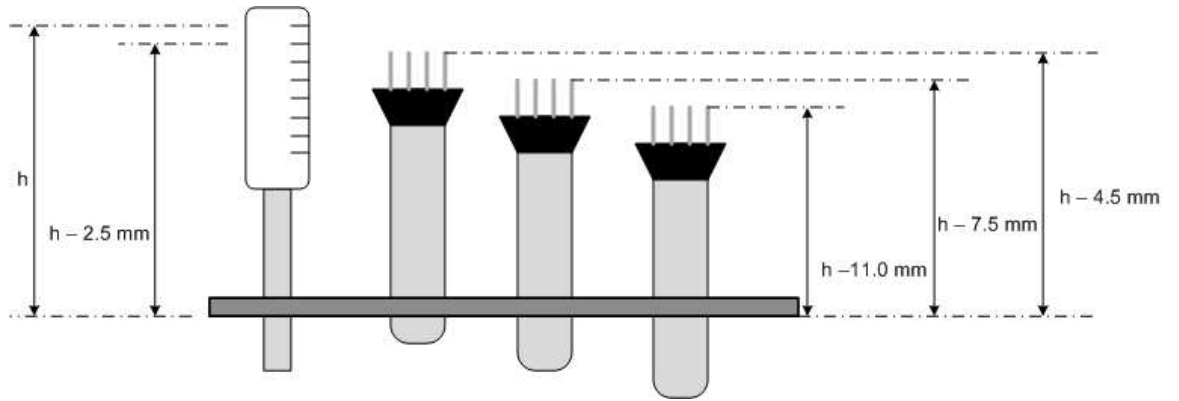
This sensor arrangement was buried at several cross shore locations for measurements of sediment concentration along with swash depth and velocity for sediment transport calculations. After the concentration sensor elevation was such that the intial bed level was roughly 0.002-0.003 m below the highest CCP electrode pair,

the profile was smoothed to achieve the initial planar profile. The water level was raised such that the sensors and most of the sandy beach was submerged. This water level was left over night in most cases in order to eliminate drift problems (described in the previous chapter). The following day the water level was lowered incrementally (to the SWL, 0.42m) and the buried wave gage and sediment concentration sensors were calibrated. Before waves were ran, the cross shore beach profile was collected using the laser distance meter. Profile elevation measurements spanned from the upper limit of the sandy profile (x = 2.91 m) to the shoreline (x = 0 m). Measurements were taken every 0.10 m in general and every 0.05 m within 0.35 m of the sensor location.

After the initial measurements were complete a set of 20 individual solitary waves were ran. A board was placed in the flume after the swash event for the individual wave was complete in order to prevent reflected waves reaching the sandy profile. After the reflections were dampened, the concentration sensor height relative to the bed level was measured and the next wave was generated. For waves 3, 7, 11, 15, and 19, the CCM's were turned off to ensure that several reliable velocity signals would be obtained during each set. After every fourth wave, the cross shore beach profile was measured in the same way as the initial profile. However, as the profile evolved, the shoreline migrated towards the upper beach so subsequent beach profiles could not be collected out to x = 0.00 m (the initial shoreline location).

This set of 20 waves was ran four times with the sensors located at x = 0.98 m and one time each with the sensors at the following cross shore locations: x = 1.04 m, x = 0.80 m, x = 0.28 m , x = 0.32 m, and x = 0.46 m. The four sets taken at the same location were done so in order to investigate repeatability. If the concentration signals were similar from the same wave number in different sets at the same cross shore location, the net transport calculations from the closely grouped sets (x = 1.04 m, 0.98 m, 0.80 m and x = 0.46 m, 0.32 m, 0.28 m) could be compared with

the beach profile changes within those regions for validation (see end of Chapter 5).

It was immediately noticed, however, that the CCM and the CCP measurements disagreed with one another significantly. The top plot in Figure 4.1 shows the swash depth signal resulting from the run-up of a broken solitary wave. The middle and bottom plot in Figure 4.1 show the sediment concentration profiles obtained by the CCM and CCP, respectively. The swash depth shows a rapid increase at the beginning of the signal representing the front edge of the swash passing the sensor location. Based on the depth signal, flow reversal occurs sometime between 3 and 4 seconds. The slow decrease in depth at the tail end of the swash event is due to the thin sheet of water moving seaward as well as residual infiltration of fluid at this location on the beach face (The treatment of this portion of the depth signal and its implications on transport estimates will be discussed in Chapter 5). At the beginning of the event, there is a rapid response of the sediment concentration below the at-rest bed level. Unlike suspended sediment concentration measurements under swash forcing, the response is a decrease in concentration as the packed bed dilates and sediment is carried upslope and into the lower water column. During flow reversal (from 3 to 4 seconds), the sediment concentrations below the initial bed level increase as the sediments settle. During backwash, the concentrations again decrease indicating bed dilation as the grains are sheared due to increasing velocity. In the event shown, the CCP detected sediment mobility as deep as 1.2×10^{-2} m while the deepest bed agitation as detected by the CCMs is 2.5×10^{-3} m (relative to the initial at rest bed level). Also, the concentration detected by the CCP (0.1 - 0.3 m^3/m^3) is much lower than the concentrations detected by the CCM (0.4 - 0.5 m^3/m^3).
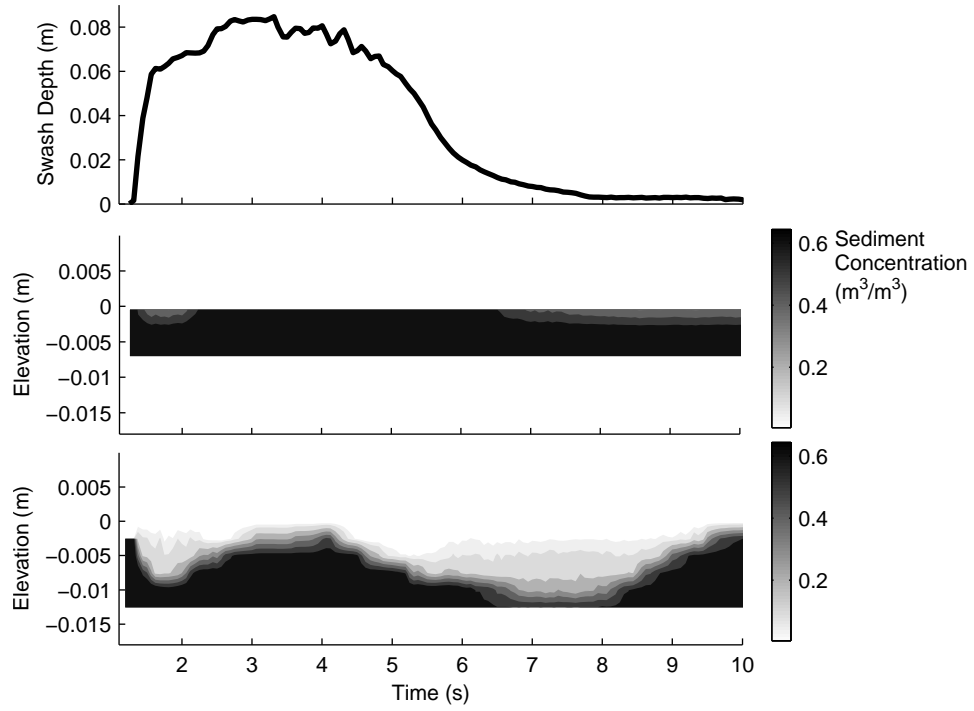
Figure 4.1: The top plot shows the instantaneous sediment concentration profiles (color) throughout a swash event as measured by the CCMs. The bottom plot shows the concentration profiles measured by the CCP for the same swash event.

It was not immediately certain what caused such a discrepancy. One possible explanation was that the CCM has a much larger sensing volume than the CCP and therefore might miss slight bed mobility that the CCP detected. However, if such low concentrations, as detected by the CCP, were present the CCM would certainly detect mobility. Also the length scale over which the bed was mobilized according to the CCP is large enough such that the 'large' measuring volume of the CCM would not have been an issue.

The likelier explanation was scour. Some scour was certainly expected since any rigid instrument much larger than the sediment grain size disturbs the flow field. Based on visual observations scour did not seem to be as substantial as suggested

68

by the data. If any, only slight perturbations in the beach profile formed around the CCP. However, during the actual swash event it is hard to visually determine whether or not scour was occurring during the uprush and backwash when the bed dilation occurs. After evaluating each of the data sets, definitive evidence of scour being the source of the disagreement between the CCM and CCP was found. For the data set collected when the sensors were placed at x = 0.28 m, the initial elevation of the concentration sensors was such that the CCP was completely buried. During the first 4 swash events, no bed mobility was detected by the CCP. However, after the fourth swash event the tip of the CCP was exposed. Figure 4.2 shows swash events 3-8 for this data set. After the fourth event, the CCP measures mobility deeper into the bed as the tip of the CCP becomes more exposed. For swash event 3, when the tip of the CCP was still buried, no mobility was measured by the CCP 3.00×10^{-3} m and deeper. During swash event 5, before which the tip of the CCP was slightly exposed, the CCP detected mobilization as deep as 4.00×10^{-3} m. Proof of scour is more evident in later events when the CCP is more exposed. For example, during event 8, the CCP measured mobilization 1.30×10^{-2} m deep.
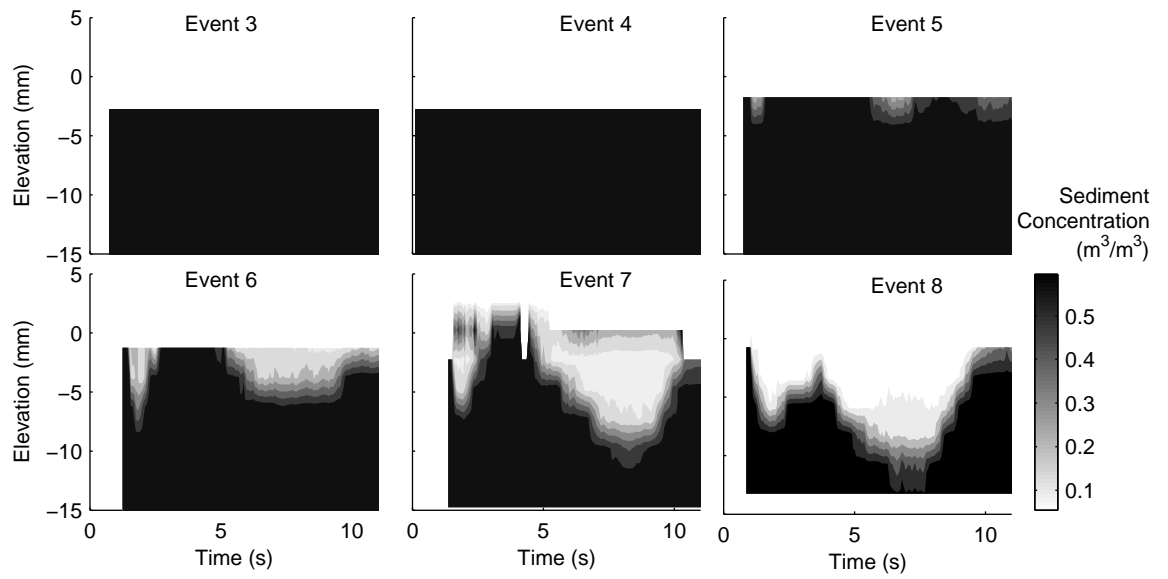
Figure 4.2: The plots show the instantaneous sediment concentration profiles (color) throughout different swash events as measured by the CCP. The tip of the CCP was buried in the earlier events and became more exposed during the later ones.

Chapter 5

RESULTS

As has been explained in the previous chapter, the ideal experimental approach yielded unrealistic results. A second experimental approach, while less ideal and likely contains errors induced due to the assumption of longshore uniformity, still produced promising results. Rather than using the CCMs as validation for the CCP signal, the CCMs were used to supplement the CCP in obtaining concentration profiles (See Figure 5.1). Since the CCP yielded realistic measurements so long as it was physically buried and no evidence of scour about the sensing volume of the CCM has been observed, the sensors were arranged such that the CCMs obtained measurements closer to the bed level while the CCP was situated deeper into the bed. Rather than a set of 20 waves being run and repeated, waves were run until the bed eroded locally to the point that the CCP was exposed and scour affected the CCP data as determined by visual observations.

Since less waves were run, local profiles (spanning about 0.20 - 0.30 m across either side of the sensor location) were collected after each wave. The profile measurements were also used to determine sensor elevation relative to the at rest bed. The sensor array was initially set such that all of the sensors were buried. Comparing bed elevation when the highest sensor became exposed and previous bed elevations when the sensors were buried yielded approximations for sensor elevations for cases in which all sensors were buried. After the sensor(s) became visible, visual measurements were used to approximate sensor elevation.

71
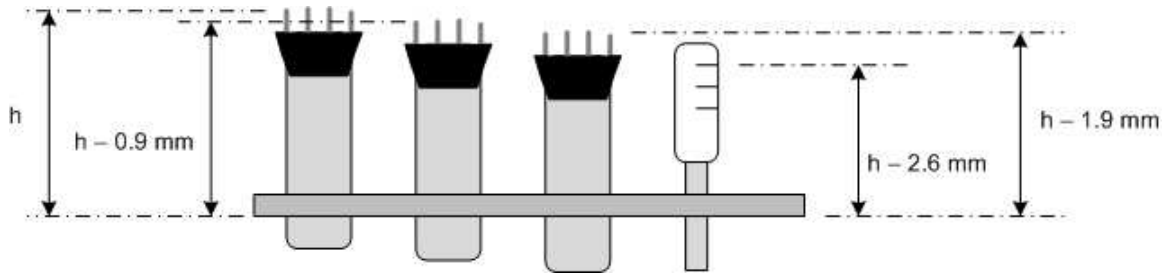
Figure 5.1: This sketch shows the sensor arrangement for the experimental set-up from which data will be presented. The CCMs are offset slightly from each other and from the CCP to supplement the concentration profile.

Of the ten data sets collected using this approach, two seemed to be complicated the least by longshore irregularities. (Evidence of longshore irregularities effects on a concentration signal will be shown in Section 5.4). These two data sets were taken at two different cross shore locations (0.90 m and 0.37 m away from the initial shoreline, x = 0.90 m and x = 0.37 m). The data from these two sets were analyzed in detail and are presented.

5.1 Depth Signal

While the calibration of the depth wave gage was relatively simple to apply, additional adjustments were necessarily applied to the calibration throughout a set of waves. First of all, the depth signal had to be adjusted for the changing bed level. An investigation showed that the wave gage output depended not only on the water depth, but also on the depth it was buried in a saturated bed. As the buried wave gage became more exposed due to local bed erosion, the voltage corresponding to a depth of zero changed i.e. the voltage output by the wave gage at the start of each subsequent swash event was typically less than that of at the start of the previous event and, therefore, less than that of the voltage corresponding to zero depth from the calibration. To account for this, the difference between the voltage

from the depth signal at the beginning of each swash data collection (before the uprush reached the sensor location) and the voltage corresponding to zero depth from the wave gage calibration was applied to the swash depth calibration such that the depth signal was zero before the swash event reached the sensor location. The second adjustment was required due the lack of consistency between depth signals at the end of backwash.

There is difficulty in verifying the tail end of the backwash as there is a very thin layer of water that resides after the dynamic portion of the backwash ends (See Chapter 4, Figure 4.1). It is uncertain exactly when this thin layer is no longer present and, therefore, it is uncertain when the depth signal should actually be zero. However, the depth signal in this portion of the backwash ought to be similar from event to event. This was not observed in the measurements (Figure 5.2); the depth of this residual flow in the backwash varied in magnitude from event to event and sometimes went negative. The top plots in Figure 5.2 show the last 4 seconds of the depth signal for two swash events in the same set. The magnitude of swash depth in the left plot is higher than that on the right. This is likely due to the effect of bed level change throughout the swash event. To provide consistency in this portion of the signal from test to test, the depth value at the end of the signal was set to zero. The depth values between flow reversal and the last time step were adjusted linearly such that the final depth was zero. The adjusted bed signal to account for inconsistencies due to bed level change are shown in the lower plots in Figure 5.2.

Throughout the swash event, the depth signal is relatively insignificant in terms of quantitative measurements. However, the special attention paid to the beginning and end of the signal was essential because the depth signal was ultimately used to define the starting and ending point of the swash event during data analyses. The start of each swash event was defined as the time step before that at which the depth signal first exceeded 5 x 10^{-4} m. The end of the swash event was defined

as the time at which the depth was less than 3×10^{-3} m because extrapolating the measured forcing is likely erroneous for the thin layer at the end of the cycle (described in Section 5.3.2).
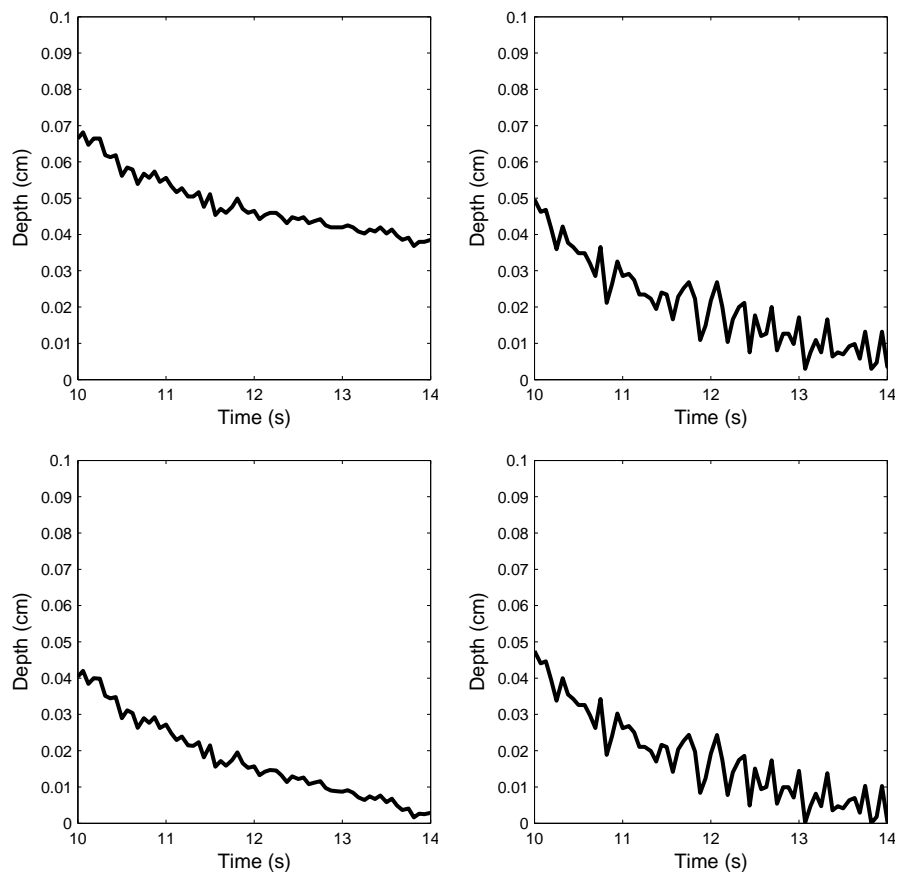
Figure 5.2: The top plots show the end of the depth signal for two different swash events. The bottom plots show the same two signals after the adjustment at the end of the signal.

5.2 Concentration

Like the depth signal, the simple two point calibration described in the previous chapters required adjustments for each swash event. The adjustments were

necessary due to the variability in the concentration signals. For example, a particular CCM or CCP sensor does not record the same exact voltage every time it is introduced into the packed bed or into the water column. Additional uncontrolled variables such as slight change in temperature, suspension of the small concentration of fines and changes in compaction of the bed were unaccounted for in the in situ calibration. Therefore, the values for V_{wat} or V_{bed} from Equation 3.23 were adjusted for each particular sensor for each particular swash event. Any adjustments were within ± 1 standard deviation of the mean water and bed signals obtained from the in situ calibration.

To adjust the signals, every signal from every event was analyzed. If the sensor was known to be buried at some given time (before the swash reached the sensors for example) and the calibration at those times yielded concentrations slightly different from 0.65 m^3/m^3 (the assumed sediment concentration in the packed bed), the voltage at those times were used to replace V_{bed} in Equation 3.23. On the other hand, if the concentration was known to be essentially clear water (i.e. when the sensors were high above the bed or if the measured concentration values were slightly negative) and the concentration was slightly different than 0.00 m^3/m^3, the voltages at those times replaced V_{wat}. The top plots in Figure 5.3 shows representative concentration signals that required slight adjustments in the two point calibration. The left and right plots show a portion of the swash where the sensor is known to be in the packed bed and in clear water, respectively. The bottom plots show the concentration signals after the calibration adjustments are applied.
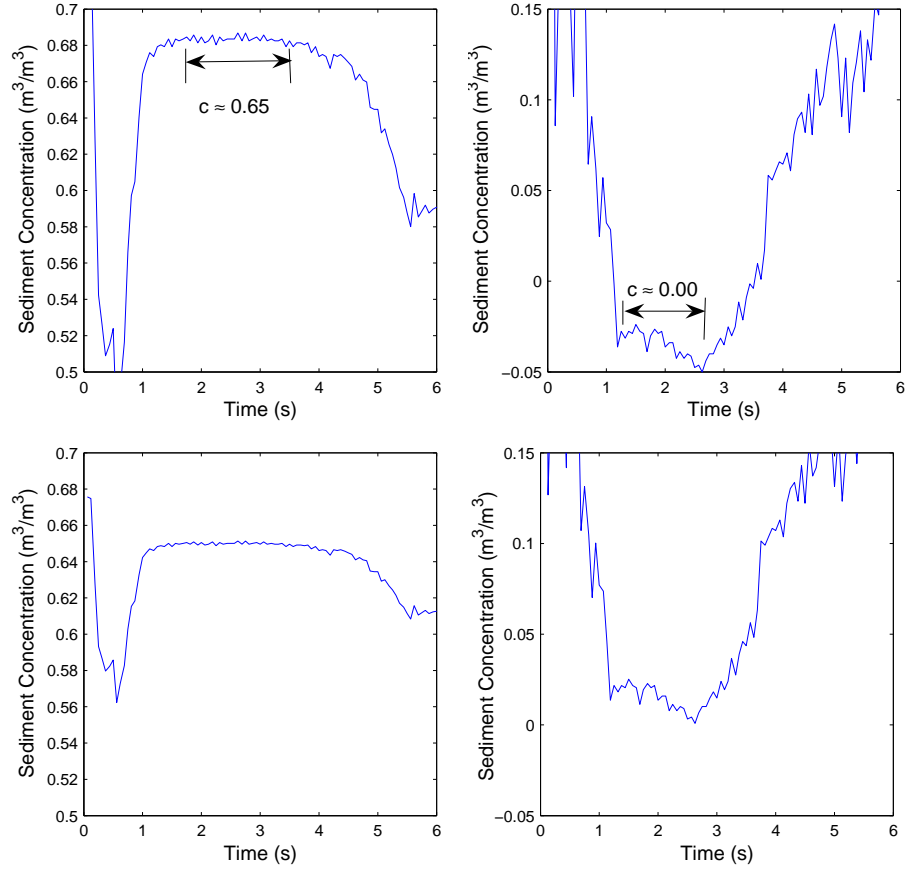
Figure 5.3: The top plots show parts of the concentration signal for different sensors during different waves. The bottom plots show the same two signals after appropriate adjustments to the two point calibration due to changes in uncontrolled variables.

After the calibrations were adjusted for each event, the concentration signals were used to determine the instantaneous bed level relative to the initial bed level throughout each swash event. The elevation of each concentration sensor relative to the initial bed level was recorded based on visual estimates before each swash event. The measured resolution of the concentration profile was determined by the sensor spacing. To obtain a better resolved concentration profile a linear interpolation of

the concentration signal between the known elevations was done such that the resolution of the interpolated concentration signal was 1 x 10^{-4} m. The instantaneous bed level at each time step was defined as the maximum elevation (relative to the initial bed level) for which the concentration was above the packed bed value (0.65 m^3/m^3). The time/space grid obtained from this interpolation scheme (Figure 5.4) was used to extrapolate the velocity profile and to make transport estimates (Section 5.4).
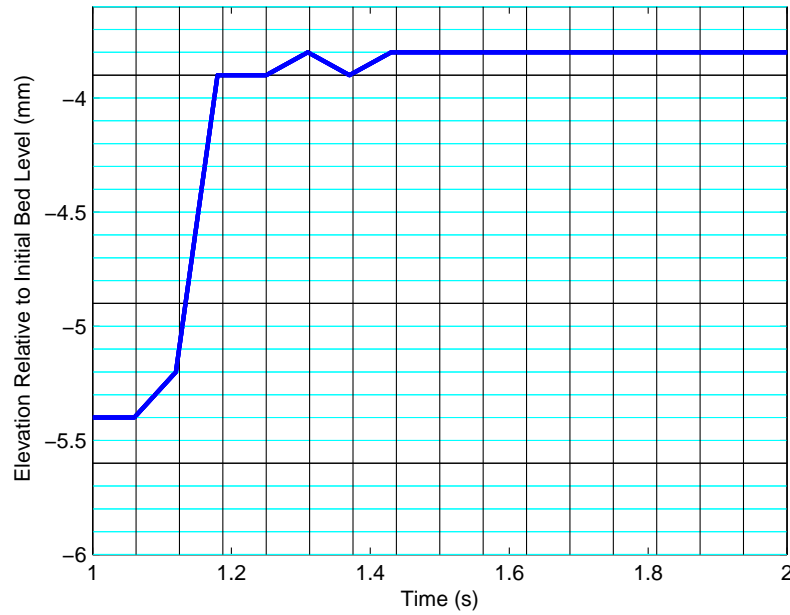
Figure 5.4: The concentration was interpolated to a 1 x 10^{-4} m resolution. This grid was used to find the instantaneous bed level (blue), in the extrapolation of the velocity profile and in transport calculations. The black lines indicate the elevations of actual measurements and the cyan represent the elevations of interpolated values. The time resolution is 16 Hz (no interpolation).

5.3 Velocity

As mentioned in Chapter 3, the velocity data was collected assuming that the forcing is practically constant between different sets of waves and any deviation in velocity from set to set would be within the range of accuracy of the EMCMs. This was necessary due to the interference of the CCMs on the EMCMs (See Figure 3.12).

5.3.1 Filtering

Since the data was logged such that the entire swash event was sure to be captured, a significant portion of the signal captured contains noise from before and after the event. Further, since the EMCMs are some distance above the bed, a portion of the swash event itself is not actually captured by the EMCMs.

The first thought would be to simply use the depth signal to determine the start and end of the velocity signals. Since the height of the EMCM could be measured before each wave, whenever the depth signal determines that the swash depth is less than the height of the EMCM, the EMCM certainly cannot detect the velocity. However, doing this would leave too much of the signal during uprush. This is because, based on observations, the EMCM takes some finite time to yield a coherent response after being wetted. Further this could potentially leave too much or leave too little of the signal during backwash because the sensor height could not be measured as precisely (due to the care that is necessary not to disturb the sandy bed locally around the sensors) as the swash depth is measured by the wave gage. Since the velocity of a solitary swash event is qualitatively well defined, the points at which the velocity signal was obviously erroneous due to the sensor being dry could be determined by visually inspecting each signal.

Figure 5.5 shows the velocity profiles for both EMCMs and the swash depth throughout a swash event. It is clear that before the sensor is wetted and after the sensor dries out, the velocity measurements are noisy. Also, the EMCMs does

not instantaneously record velocties accurately as evident by the difference in depth between the beginning and end of the cycle during which the signal seems reasonable. The dots denote the points before and after which the velocity is inaccurate.
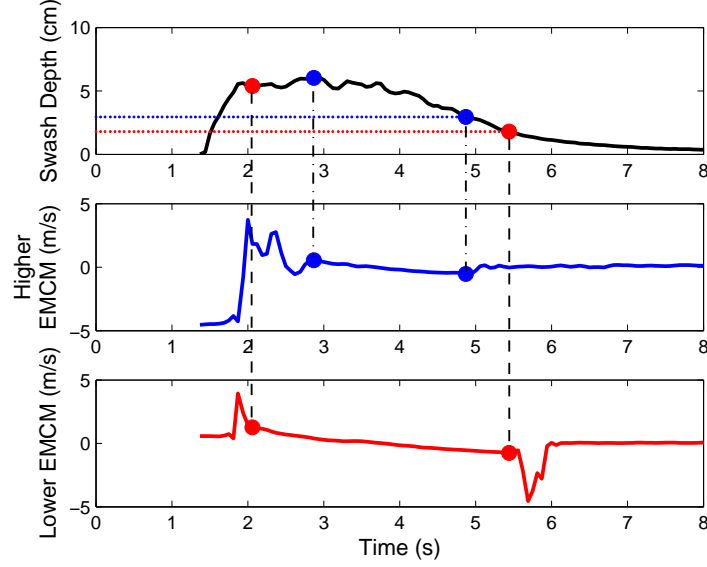
Figure 5.5: The lower two plots show the velocity signal from either EMCM throughout a swash event while the plot shows the swash depth throughout the corresponding event. The blue dots and red dots denote the times between which the velocity signal are not obviously erroneous due to the depth being shallower than the instrument height.

After removing points from the velocity signals during which the sensors were dry or clearly responding inaccurately, an additional quantitative method was applied to filter out erroneous velocity measurements within the retained signals. This was necessary because after further examination of the retained velocity signals, the accelerations based on a forward difference method were far greater than one would physically expect. This was particularly true in the begining and end of the retained velocity signal (Figure 5.6), presumably as the sensor was being wetted and drying out, respectively. Figure 5.6 shows an example of the begining of a the

retained portion of a velocity signal. The acceleration based on a forward difference calculation between points in the begining of this signal was - 2.06 m/s^2 while the mean calculated acceleration over the entire retained signal was - 0.5 m/s^2.

To filter the velocity, the magnitude of the swash acceleration was assumed. Though it has been shown that pressure gradients may have short lived effects on acceleration and friction certainly dampens acceleration, to first order, the dominant force is gravity. Therefore, the value of gravity along a 1/12 slope was used as a proxy for the maximum magnitude of acceleration.

$$a_{max} = -g\sin(\theta) = -9.81m/s^2 \frac{1}{\sqrt{145}} \approx -0.815m/s^2 \qquad (5.1)$$
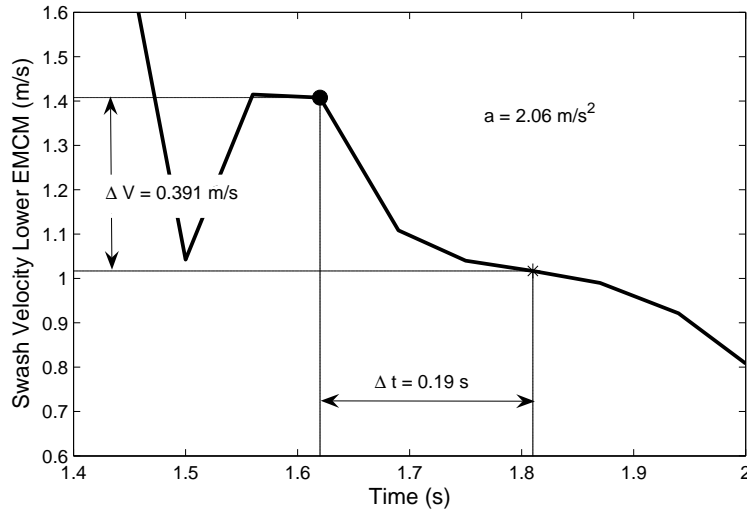
Figure 5.6: Acceleration based on a forward difference method were clearly erroneous at some points, particularly in the beginning and end of the retained velocity signal as the sensor is being wetted and drying out, respectively.

The change in velocity determined by a forward difference calculation (δV in Equation 5.2) divided by the time step (δt in Equation 5.2) was used to determine

the acceleration as measured by the EMCMs ($a_{measured}$). At locations where the magnitude of $a_{measured,i}$ exceeded the magnitude of a_{max} from Equation 5.1 the velocity measurement was removed from the signal.

$$a_{measured,i} = \frac{\delta V}{\delta t} = -1(V_i - V_{i+1})16s^{-1} \tag{5.2}$$

$$|a_{measured,i}| >= |a_{max}| \rightarrow V_i = NaN \tag{5.3}$$

For the removed velocities that were in between two retained velocities, a linear interpolation was used to replace the removed value.

5.3.2 Respresentative Velocity

Though the same wave was generated for every event, as the profile evolves from a plane to a concave shape, it is possible that the second order effects of a slight local change in beach slope on actual velocity would be detected in the velocity signal. Therefore, after the velocities were filtered, the velocity signals for every wave for a given EMCM at a given location were compared. Figure 5.7 shows three of the velocity signals from the lower EMCM at x = 0.37 m from the initial shoreline. As this comparison shows the difference in the measured velocity from wave to wave shows no coherent pattern that could be attributed to the changing profile. This was also observed in the higher EMCM and in both EMCMs at the other cross shore location (0.90 m). Therefore, the mean velocity signals from the set of 10 waves at each time step in the swash cycle for which all of the filtered velocities had real values was used as the representative velocity.
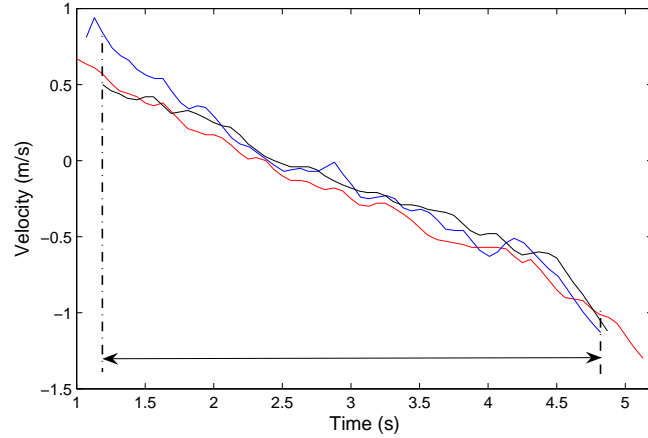
Figure 5.7: A comparison of three velocity signals at the same cross shore location where the red blue and black lines represent the filtered velocity from the first, fifth, and ninth swash event at x = 0.37 m. The mean velocity signal was obtained from all times in which the filtered velocities had real values (as illustrated by the dashed-dotted line),

Since the velocity signal is being applied to a different set of waves for which no accurate velocity signals could be obtained, it was necessary to compare the forcing between the velocity tests and the concentration tests by some means. The assumption is that the first order forcing is the wave itself. Even though the same paddle stroke was sent for each wave, for all tests, the wave generated is a function of water depth (see Chapter 3 for Solitary Wave Maker Theory). It is likely that the still water level was slightly different ($O(10^{-4}$ m)) from set to set. Therefore, it was necessary to compare the offshore wave profile to show repeatability. Figure 5.8 shows the agreement in the average wave profile during the concentration tests and velocity tests at x = 0.37 m. The mean wave from the velocity measurement lies within $\pm$ 1 standard deviation of the wave signals recorded during the concentration measurements. The waves for both tests are practically equivalent to within the accuracy of the measurement. The comparison of data recorded from 0.90 m

landward of the SWL show similar agreement. Since the first order forcing is practically the same and the second order effects such as profile change were shown to be negligible, using the velocity signal obtained in the separate test can be applied to the concentration runs with confidence.
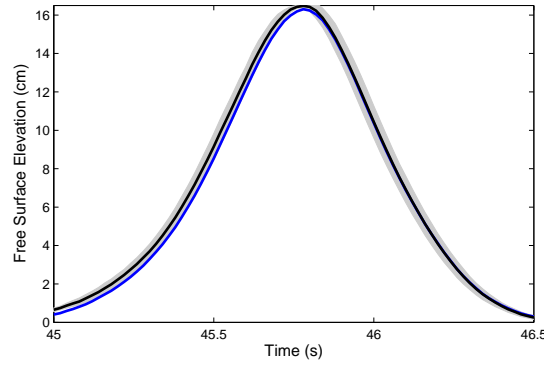
Figure 5.8: The black and blue line represents the mean offshore free surface profile from the concentration waves and velocity waves taken 0.37 m landward of the SWL, respectively. The gray represent ± 1 standard deviation of the wave signals recorded during the concentration measurements.

Further treatment of the velocity was still required. The mean velocity signals clearly contained noise. A linear fit through the mean signals was used as the representative velocities. This approximation is reasonable because the measured acceleration for each subsequent swash event were essentially constant. The final treatment that was required was extrapolating the velocity signal. Figure 5.9 shows the average measured velocities from both EMCMs at x = 0.90 m above the extrapolated linear fit through the mean signals (middle plot) and the concentration signal from a swash event recorded at x = 0.90 m. If the velocity was not extrapolated, transport calculations described in Section 5.4 would be bound by the times denoted by the vertical dash-dot lines in Figure 5.9. Doing so would clearly underestimate sediment transport in a given swash event. Most of the apparent mobility

in the backwash, based on the concentration signal occurred when the depth was below both current meters. Therefore, it was necessary to extrapolate the velocity to include sediment transport throughout the entire cycle.
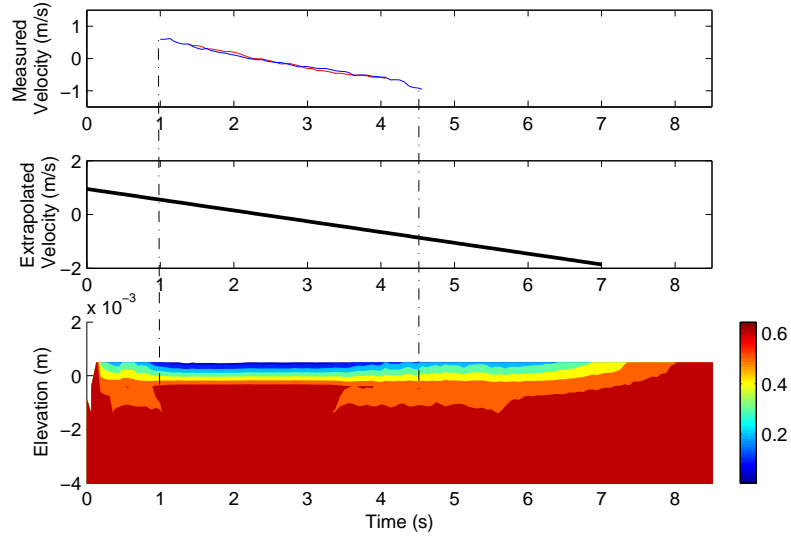
Figure 5.9: The red and blue lines in the top plot represent the mean measured velocities from the higher and lower EMCM, respectively. The black line in the middle plot represents the linear fit through the mean signals. The bottom plot shows the concentration profile for a representative swash event.

The velocity was extended to the beginning of the swash event as determined by the clear initial increase in the depth signal. The "end" of the velocity signal was less clear (as mentioned before). It is quite clear, however, based on visual observations that the latter portion of the backwash becomes dominated by frictional forces and is no longer accelerating in the offshore direction. Therefore, the duration of the swash was determined as the average time when the depth becomes less than 3 x 10^{-3} m at each cross-shore location. This omits some small sediment movement at the very end of the swash event as it was observed that a few individual grains moved in the shallow water seconds after the obvious backwash ended. However, the linear

extrapolation of the velocity signal to these shallow depths would likely be more inaccurate than the omition because velocity would be significantly overestimated.

5.3.3 Velocity Profile

Figure 5.10 shows the average velocity signal recorded at x = 0.37 m (solid) and x = 0.90 m (dotted) with respect to time. The agreement between the two velocity measurements at a given location indicates that both sensors were situated outside of the boundary layer. Otherwise, the lower EMCM would detect lower velocities than the higher one at each given time. Therefore, it has been approximated that the lowest height of the EMCM for the measurements made indicates the lower limit of free stream velocity. This approximation, however, is only verified for the times in which there are concurrent measurements of the velocity from both EMCMs. Therefore this approximation is not verified for portions of the swash event when the depth was less than the height of the higher EMCM. The velocities in the portion of the swash cycle measured by the higher EMCM and low EMCM concurrently are lower than velocities occuring during the initiation of uprush and end of backwash when the depth was shallower than the higher EMCM. Since the boundary layer grows with the magnitude of velocity, the boundary layer thickness may be under predicited during the event when depths were too shallow for concurrent velocity measurements based on the approximation made.

Even more difficult than predicting the boundary layer thickness throughout the swash cycle is modeling the velocity profile in the boundary layer. This difficulty has been shown in discrete particle modeling in which the physics of individual grains are modeled. The velocity profile in the bedload/sheetflow layer is highly nonlinear owing to the constant feedback of momentum between the fluid and sand grains and intergranular collisions [45]. Because of the present lack of knowledge pertaining to the velocity structure in a mobilized bed, two simple approaches to extending the velocity through the bed have been used for comparison.

85
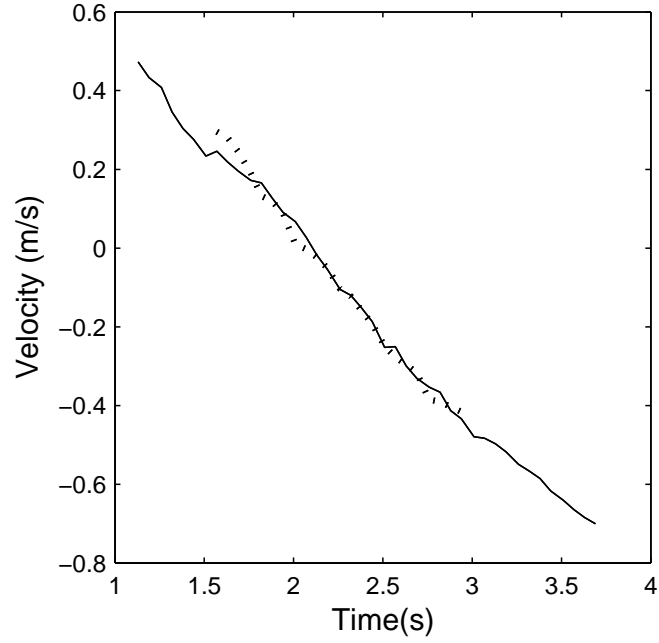
Figure 5.10: The solid line represents the mean velocity signal from the higher EMCM while the broken line represents the mean velocity signal from the lower EMCM. The shown data is from x = 0.90 m.

5.3.3.1 Linear

One simple treatment of the velocity profile is assuming a linear decrease in the magnitude of velocity from the free stream value at the assumed free stream location to zero velocity at the elevation of the instantaneous bed level as determined by the concentration signal during each individual swash event. An example velocity profile resulting from the linear boundary layer assumption throughout a swash event is shown in the left plot in Figure 5.11. Based on the comparison of the velocity measurements it was determined that the lowest EMCM was likely outside the boundary layer, as described in Section 5.3.2. The lowest EMCM was typically 15 mm from the initial bed level. Therefore, for this approximation of the velocity profile in the boundary layer, at elevations from the free surface down to an elevation

86

of 15 mm the velocity was set equal to the free stream velocity as determined by the extrapolated mean signal described in Section 5.3.1. When the depth was below 15 mm, the free stream velocity was set to the free surface at that time step. Essentially, the boundary layer at each time step extended from the minimum value of 15 mm or the free surface elevation down to the instantaneous bed level as determined by the gridded concentration signal. The right plot in Figure 5.11 shows where the free stream boundary is the free surface rather than the predefined elevation (15 mm). A vertical resolution of 0.1 mm was used to extend the velocity profile in the boundary layer as to match the grid resolution for the concentration signal (Figure 5.4).
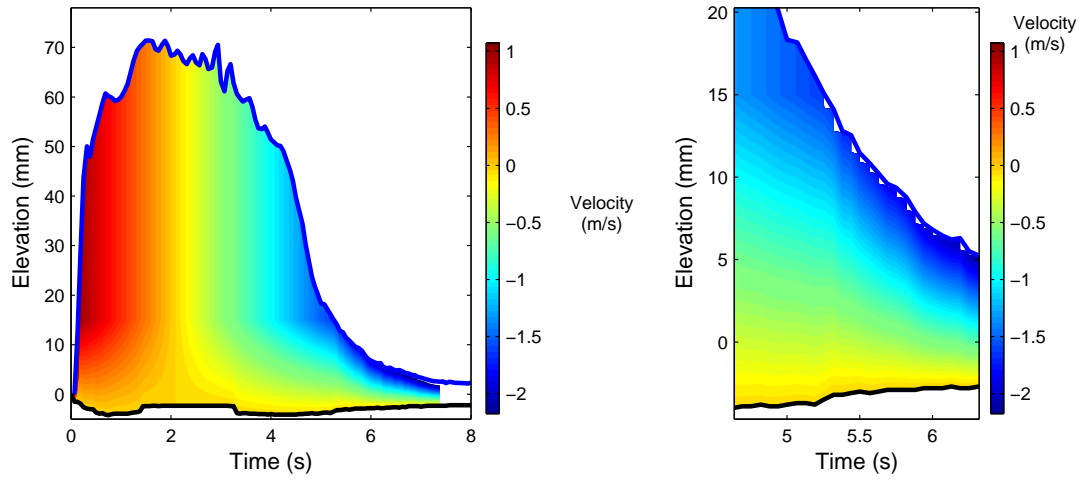
Figure 5.11: The plots shows the velocity profile throughout a swash event where the color corresponds to the value of velocity in space and time. The solid blue line represents the swash depth (free surface elevation) while the black line represents the instantaneous bed level. This is a representative plot taken at x = 0.37 m.

5.3.3.2 Law of the Wall

The vertical velocity structure within the boundary layer of steady, hydrauli-
cally rough, and turbulent flows is typically defined according to the Law of the
Wall

$$u(z) = \frac{u^*}{\kappa} \ln \frac{30z}{k_s},$$ (5.4)

where z is the elevation relative to the instantaneous bed, k_s is the Nikuradse rough-
ness length, $\kappa = 0.4$ is the Von Karman's constant and the shear velocity, u^*, is given
by

$$u^* = \sqrt{\tau/\rho},$$ (5.5)

where ρ is the density of the fluid (water) and stress, τ, in the constant stress or
boundary layer is typically given by the quadratic drag law

$$\tau = \frac{1}{2}\rho f |u| u,$$ (5.6)

where f is the Darcy-Weisbach friction factor. The difficulty in applying the Law
of the Wall is the dependence on two empirical parameters (k_s and f). A typical
inferred value for f during uprush is roughly 0.005 - 0.01 (e.g. [46], [15]). However,
inferred friction factors during backwash have been shown to be greater than uprush
values (0.01 - 0.07) [15]. Table 5.1 shows friction factors that have been infered from
swash zone measurements as well as typical friction factors.

Table 5.1: Typical friction factors found in the literature based on lab and field
observations.

	Inferred f	Typical f
Uprush	0.005 - 0.01	0.01
Backwash	0.01 - 0.07	0.01 - 0.03

The Nikuradse roughness length (k_s) also varies widely throughout the literature. The values used are a function of d_n where n is the percent of sample finer than the specific grain diameter, d. Table 5.2 (after [15]) presents values of k_s used by past researchers (See Figure 3.4 for d_n values).

Table 5.2: Different Nikuradse Roughness Lengths (k_s) used by past researchers.

Researcher	Formula	Value (mm)
Einstein (1950) [47]	d_{65}	0.55
Engelund and Hansen (1967) [48]	$2d_{65}$	1.10
Mahmood (1971) [49]	$5.1d_{84}$	3.67
Ackers and White (1973) [50]	$1.25d_{35}$	0.44
Kamphius (1975) [51]	$2d_{90}$	1.58
Hey (1979) [52]	$3.5d_{84}$	2.52
Van Rijn (1982) [53]	$3d_{90}$	2.37

To avoid errors induced by assuming a friction factor and, therefore, the value of shear stress and shear velocity, u^* is calculated by

$$u(z_{freestream})\kappa \ln \frac{30z_{freestream}}{k_s}^{-1} = u^* \tag{5.7}$$

where u($z_{freestream}$) is known from the extrapolated mean signal with

$$z_{freestream} = \min\left[1.5 \text{ x } 10^{-2} \text{ m}, \text{Swash Depth}\right] \tag{5.8}$$

The sensitivity to choice of the roughness length k_s was investigated by using the highest (Mahmood, 1971) and lowest value (Acker and White, 1973) to extend the velocity profiles and comparing the results.

5.3.3.3 Profile Comparison - Linear vs. Log

The velocity resulting from the linear profile has been compared with the profiles according to the Law of the Wall (logarithmic). Figure 5.12 shows the difference

between the logarithmic velocity profiles and linear profile throughout a swash event at each cross shore location. The magnitude of the difference between the profiles varies significantly with elevation relative to the at-rest bed due to the difference in the shape of the velocity profile in the boundary layer. Also, the magnitude of the difference is proportional to the magnitude of the free stream velocity. Therefore, the greatest difference in velocity occurs at the end of backwash when the magnitude of the extrapolated velocity is the highest. The greatest differences in velocity for a typical swash at 0.90 m from the initial shoreline are 0.921 m/s and 0.606 m/s (for $k_s = 0.44$ x 10^{-3} m and 3.67 x 10^{-3} m, respectively) while at 0.37 m from the initial shoreline, differences are as great as 1.391 m/s and 0.996 m/s (for $k_s = 0.44$ x 10^{-3} m and 3.67 x 10^{-3} m, respectively).
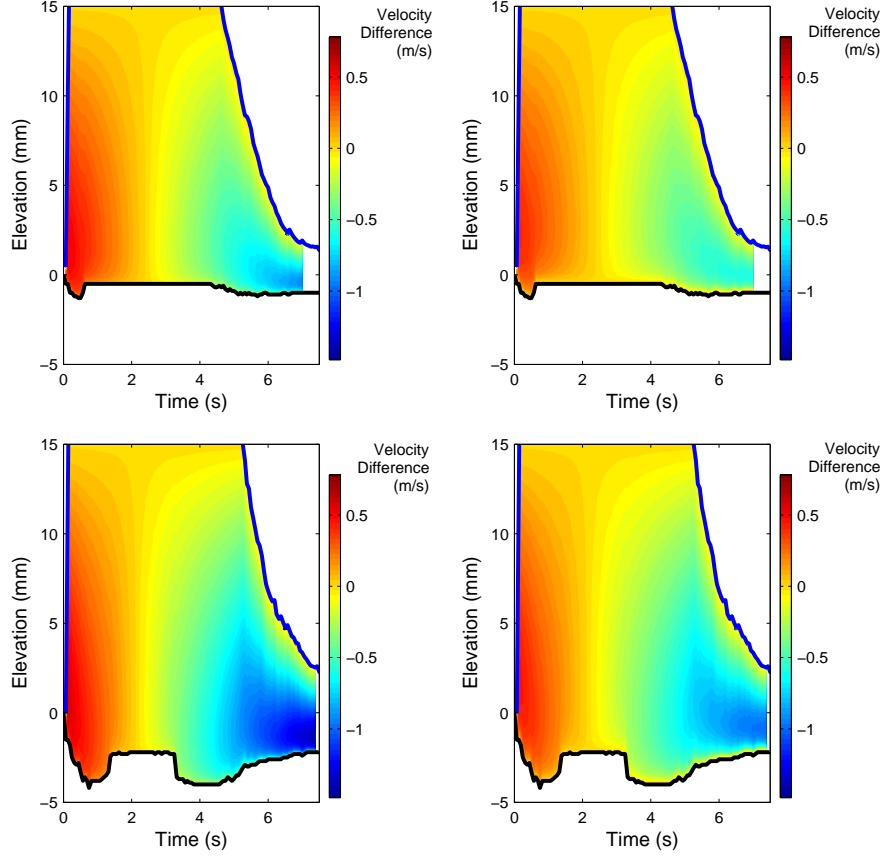
Figure 5.12: The plots shows the differences between the linear boundary layer profile and those according to the Law of the Wall (logarithmic boundary layer profile). The left and right show the differences between either logarithmic profiles and the linear profile, ($k_s = 0.44$ mm and $k_s = 3.67$ mm) respectively. The top plots show data from representative swash event at x = 0.90 m and the bottom plots show data from x = 0.37 m.

91

5.3.3.4   Profile Comparison - $k_s = 0.44$ x 10^{-3} m vs. $k_s = 3.67$ x 10^{-3} m

The magnitude of the velocity differences between the two logarithmic profiles corresponding to the range of k_s values is also significant. Figure 5.13 shows the difference between the two profiles throughout a representative swash cycle from each cross shore location. Again, the greatest difference occurs in the end of backwash when the magnitude of the free stream velocity is the largest. Near the bed, the magnitude of the velocity corresponding to the smaller k_s is significantly greater. The maximum difference in the magnitude of the velocity is 0.441 m/s and 0.222 m/s at x = 0.37 m and 0.90 m. The importance of these deviations will be highlighted in the sediment transport estimates described in the next section.
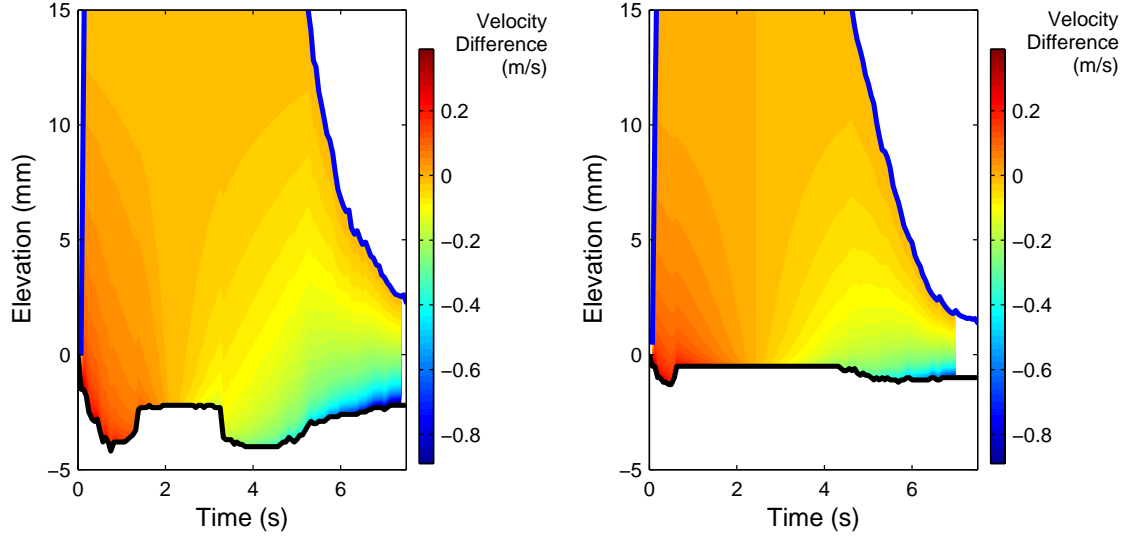
Figure 5.13: The plots show the difference in the logarithmic velocity profile due to different values of k_s. The left and right show the difference between the logarithmic velocity profiles at x = 0.37 m and x = 0.90 m, respectively. The magnitudes of velocity are significantly higher for the smaller value of k_s

5.4 Sediment Transport

The treatment of the concentration signals to obtain a concentration profile and the treatment and uncertainties pertaining to the velocity signal and boundary layer profile have been described. This section presents instantaneous sediment transport profiles from which net transport measurements have been made. Later, in Section 5.4.2, the beach profile measurements (described briefly in previous chapters) have been used to crudely validate the transport measurements in a quantitative sense. Rather than looking at individual representative events, which has been done in the previous sections for demonstration purposes, a set of events from each cross-shore location will be analyzed.

The last events in each set were scrutinized for evidence of false signals from the CCP due to scour. As described in the beginning of the chapter, the data was collected until the CCP was exposed enough to result in obvious scour, therefore, the last few events may have contained false signals that were not immediately noticed upon visual observations.

Figure 5.14 shows the concentration signals from all of the events collected at x = 0.37 m. The first event shows mobility slightly deeper than the subsequent events. While it is possible that this is due the bed being loosely compact before waves were ran, the likely explanation for the difference is the inaccuracy of measuring the conductivity sensor heights relative to the initial bed level, particularly when all sensors were buried. Therefore, the first swash event is retained for further analysis. The fourth event excludes concentration measurements from depths below the lowest CCM during uprush because the Wavetek, which powers the CCP, was not turned on until a short time after the swash event started. Further, the CCP concentration signal immediately after power supplied may be a result of the voltage lag associated with turning on the Wavetek rather than bed dilation. Therefore,

transport calculations from this event likely contains inaccuracies particularly during uprush. There is clear evidence of scour in the last event. The dilation at the very end of the backwash starting at about 7.5 seconds is a result of scour as the thin layer rushes past the exposed CCP. However, the termination of the swash event as determined by the depth signal (described previously) occurs before this obvious scour. So, while scour possibly effects events 6 and 7 because the CCP protruded from the bed slightly, it is not clear that scour will effect the accuracy of a transport calculation.
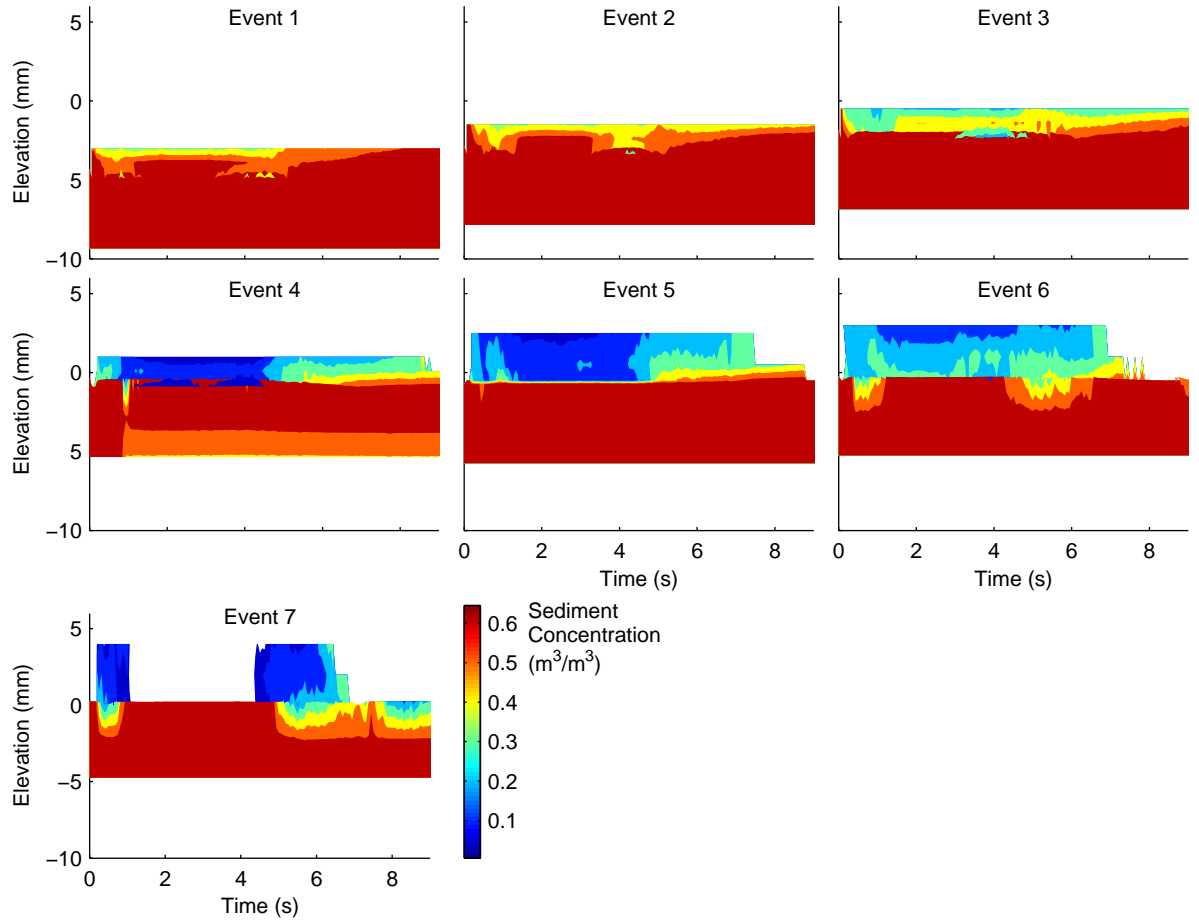
Figure 5.14: The measured concentration profile through every swash event collected at x = 0.37 is shown. While it is possible that scour around the CCP may have occurred during event 6 and 7, the concentration signal shows no overwhelming evidence of scour problems. Event 4 has inaccuracies due to the power not being applied to the CCP until some time after the swash event started.

Figure 5.15 shows the concentration signals from all of the events collected at x = 0.90 m. Like the other set of swash events, there is no clear evidence that the first couple of events are inaccurate due to loose compaction. The first three events show very little mobility at the elevations of the sensors. The fourth event exemplifies possible errors due to longshore differences. In this signal, the middle CCM detects a lower sediment concentration than the highest CCM. The highest CCM was closer to the initial at rest bed level and, therefore, should detect lower concentrations than the middle CCM during bed dilation. This is likely due to a longshore irregularity that caused the middle CCM to actually be closer to the instantaneous local bed level than the higher CCM. Evidence of this longshore irregularity was observed. After the fourth event, the profile displayed longshore non-uniformities due to an "erosional fan" in which the profile is a couple of grain diameters lower than the other locations in the longshore. This longshore irregularity was smoothed with a trowel before subsequent waves were run. The final wave in the set is likely erroneous due to scour around the CCP as evident from the depth of mobility being significantly greater (by roughly 3 x 10^{-3} m) than prior events. Therefore, the last event has been omitted from the transport analysis.
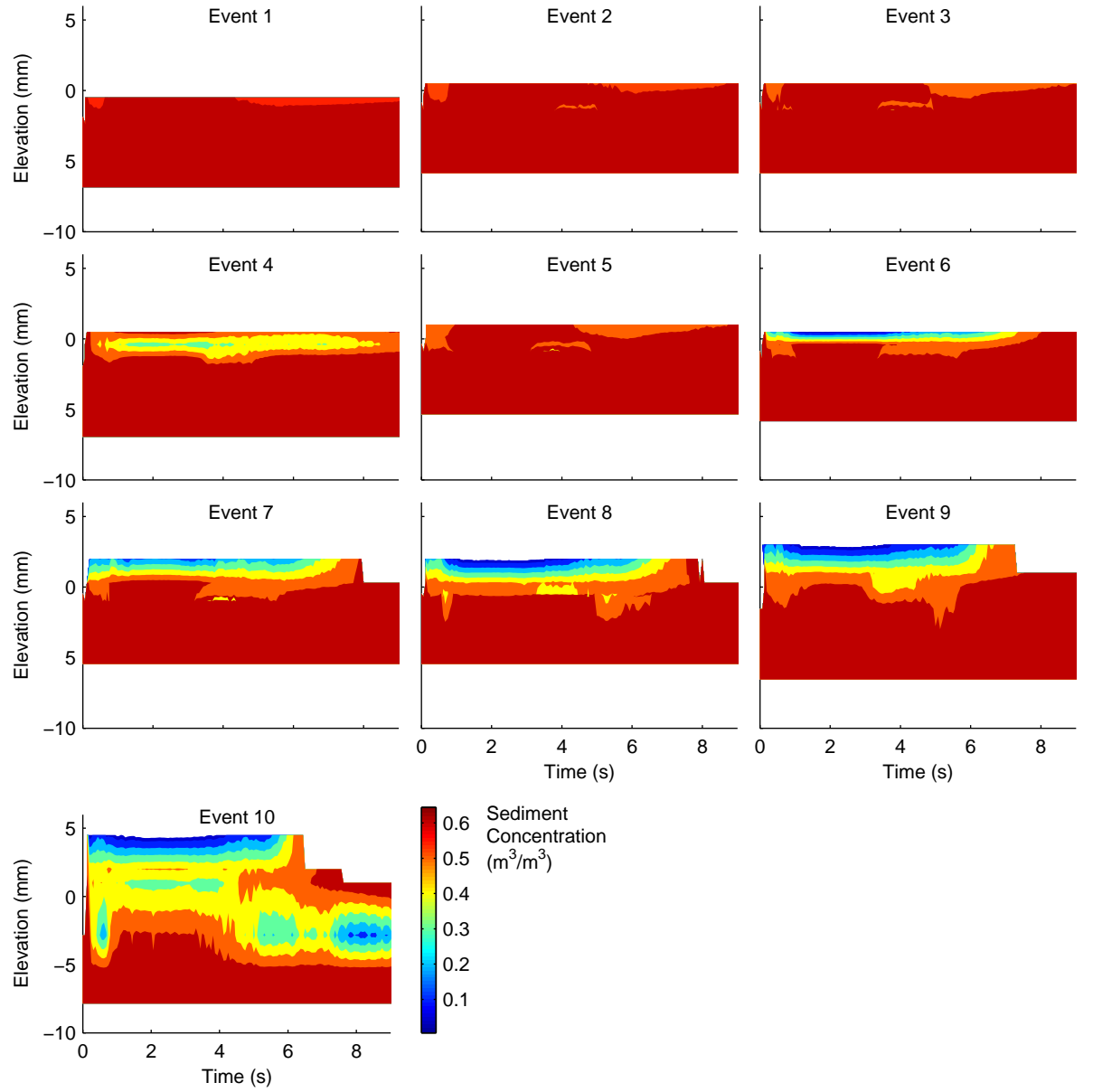
Figure 5.15: The measured concentration profile through every swash event collected at x = 0.90 is shown. Event 4 exemplifies possible inaccuracies due to longshore differences as the concentration profile shows lower concentrations deeper in the bed during some portion of the swash event. The last event is clearly effected by scour.

97

Rather than using the packed bed concentration (0.65 m^3/m^3) to find the instantaneous bed level, a concentration of 0.60 m^3/m^3 was used to determine the "instantaneous bed level" as the lower limit for sediment transport profiles. This prevents potential errors induced by the logger cross talk (discussed in Chapter 2) and other background noise that might cause the concentration sensor to falsely detect less than packed bed values. Further, other treatments of the transport calculations likely over predict actual transport. The first such treatment is in the extension of the velocity profiles. The velocity profiles are typical of fluids with uniform density. Close to the bed, where the fluid is likely a sand/water slurry with high sediment concentrations the fluid density is significantly higher than the fluid in the free stream. Therefore, it is likely that velocities *may* be over predicted.

To obtain instantaneous transport profiles (q_i, kg/m^2/s), the concentration signal is converted from volume concentration (V_c = m^3/m^3) to mass concentration (kg/m^3) assuming a typical density for sand, $\rho_s = 2650$ kg/m^3, and multiplied by the corresponding velocity ($\vec{v}$) at each elevation and time grid points. The instantaneous transport profiles are summed over depth (z) and time (t) and multiplied by the time and depth grid spacings ($\Delta t = 1/16$ s and $\Delta z = 0.1$ x 10^{-3}) to yield total and net transport values (Q).

$$V_c \rho_s \vec{v} \quad \rightarrow \quad kg/m^2/s \tag{5.9}$$

$$Q \quad = \quad \sum\sum q_i(z,t)\Delta z \Delta t \tag{5.10}$$

Figure 5.16 and Figure 5.17 show the calculated sediment transport profile using the linear velocity profile from x = 0.37 m for events 1-4 and events 5-7, respectively. Table 5.3 shows the calculated total sediment transport in the uprush and backwash and the net sediment transport per unit length in the longshore direction for the x = 0.37 m events assuming a linear velocity profile.
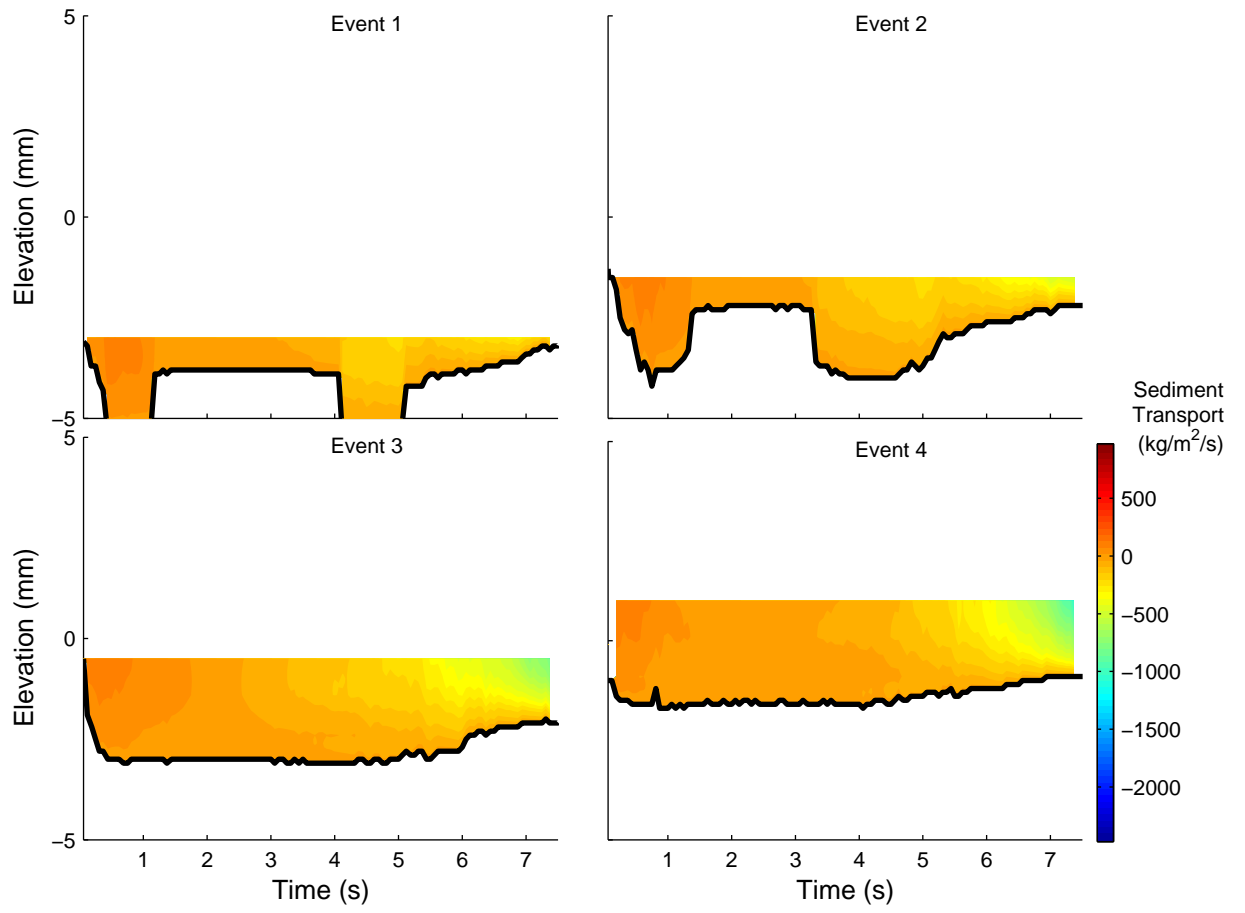
Figure 5.16: The calculated transport profiles by applying the linear velocity boundary layer profiles throughout swash events 1-4 collected at x = 0.37 are shown.
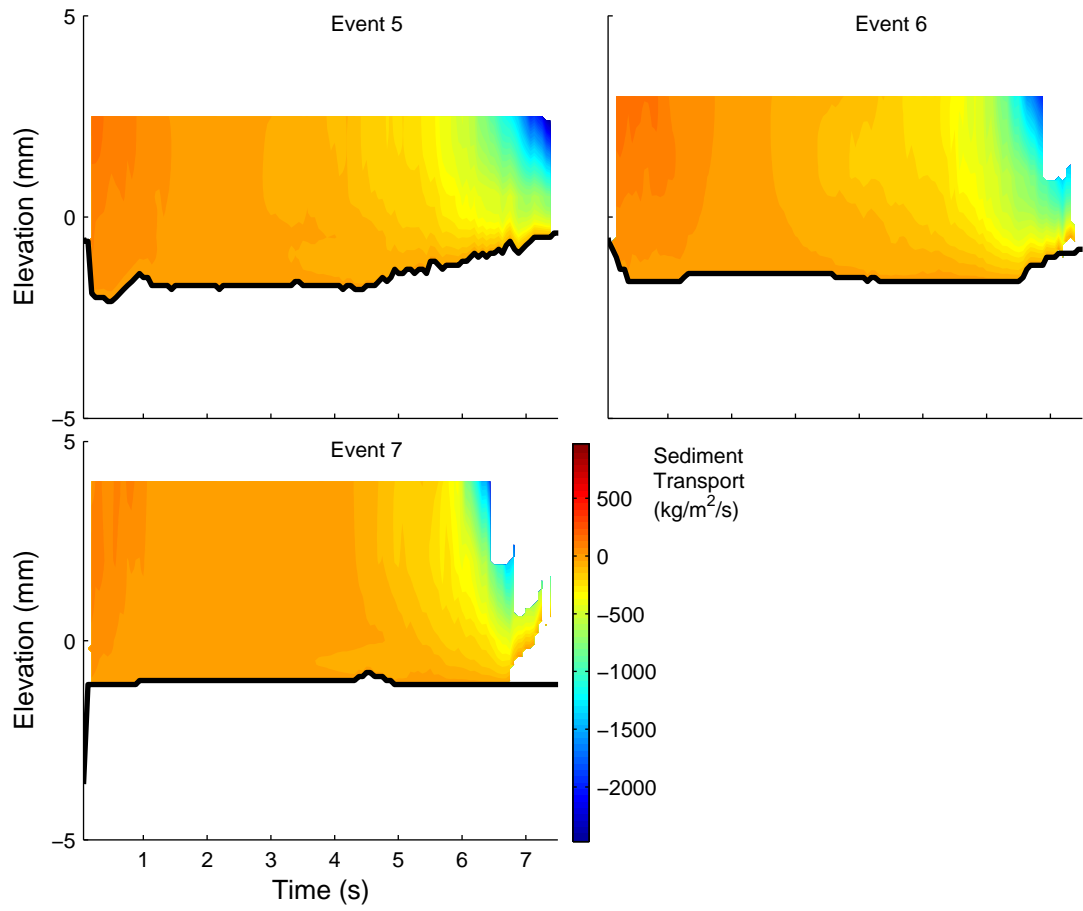
Figure 5.17: The calculated transport profiles by applying the linear velocity boundary layer profiles throughout swash events 5-7 collected at x = 0.37 are shown.

Table 5.3: Total and net sediment transport values calculated using the linear velocity profile for each event at x = 0.37 m.

Event	Onshore Transport (kg/m)	Offshore Transport (kg/m)	**Net Transport** (kg/m)
1	0.1204	(-) 0.4852	- 0.3648
2	0.1265	(-) 0.8554	- 0.7289
3	0.1893	(-) 1.7061	- 1.5167
4	0.1347	(-) 1.6399	- 1.5052
5	0.3352	(-) 4.6285	- 4.2933
6	0.4457	(-) 5.2187	- 4.7730
7	0.2303	(-) 3.1160	- 2.8857

The instantaneous transport profiles show that the transport rates are maximum at the end of backwash. This is expected as the velocity magnitudes are the highest at the end of backwash and the bed is typically still fully mobilized (as determined by the concentration signal) at the termination of the transport signal. It is also clear, from the net transport numbers that the transport is dominated by the backwash. This agrees with the accepted assumption that transport in the uprush is possibly dominated by suspended sediment advection from the surf zone and suspension due to bore generated turbulence while backwash is likely dominated by sheet flow/bed load transport. It is also observed that the net transport magnitudes increase from event 1 to event 7. This is likely because in the first 2-3 events, the concentration sensors were buried below the sheet flow layer. Therefore, the fact that less transport was measured in the first few events is the result of the sensors being situated too deep within the bed rather than less actual transport. In the later events the sensors were closer to or above the initial bed level and were able to capture sediment moving as sheet flow. The net transport rates ranged from -0.3648 kg/m to -6.7226 kg/m for event 1 and 6, respectively.

Figure 5.18 and Figure 5.19 show the calculated sediment transport profile using the linear velocity profile from x = 0.90 m for events 1-4 and events 5-9,

respectively. Table 5.4 shows the calculated total sediment transport in the uprush and backwash and the net sediment transport per unit length in the longshore direction for the x = 0.90 m events assuming a linear velocity profile. Again, the transport in the backwash dominates the net transport and the magnitude of the transport increases as the sensors become closer to the initial bed level. The net transport magnitudes ranges from -0.1369 kg/m to -4.2094 kg/m for events 2 and 8, respectively.
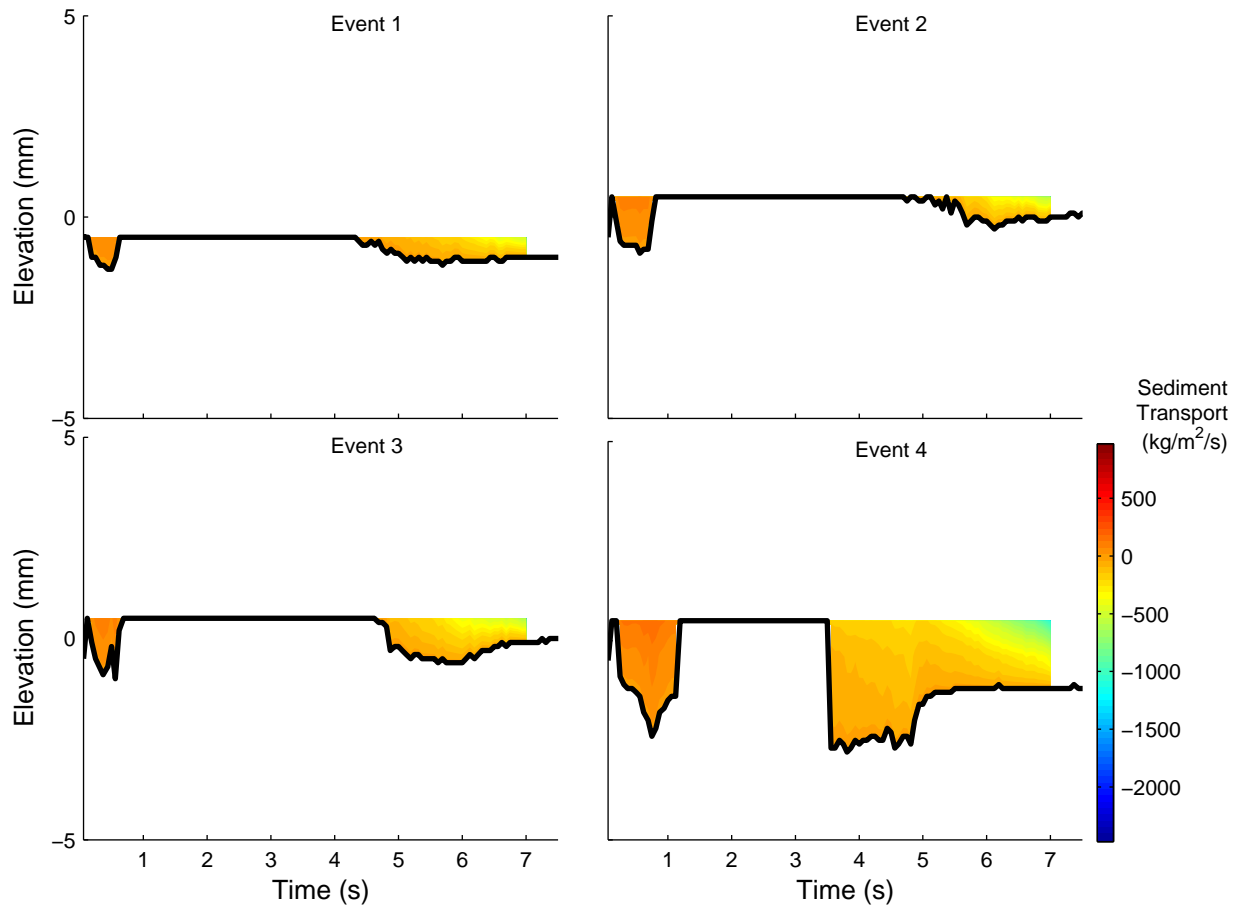
Figure 5.18: The calculated transport profiles by applying the linear velocity boundary layer profiles throughout swash events 1-4 collected at x = 0.90 are shown.
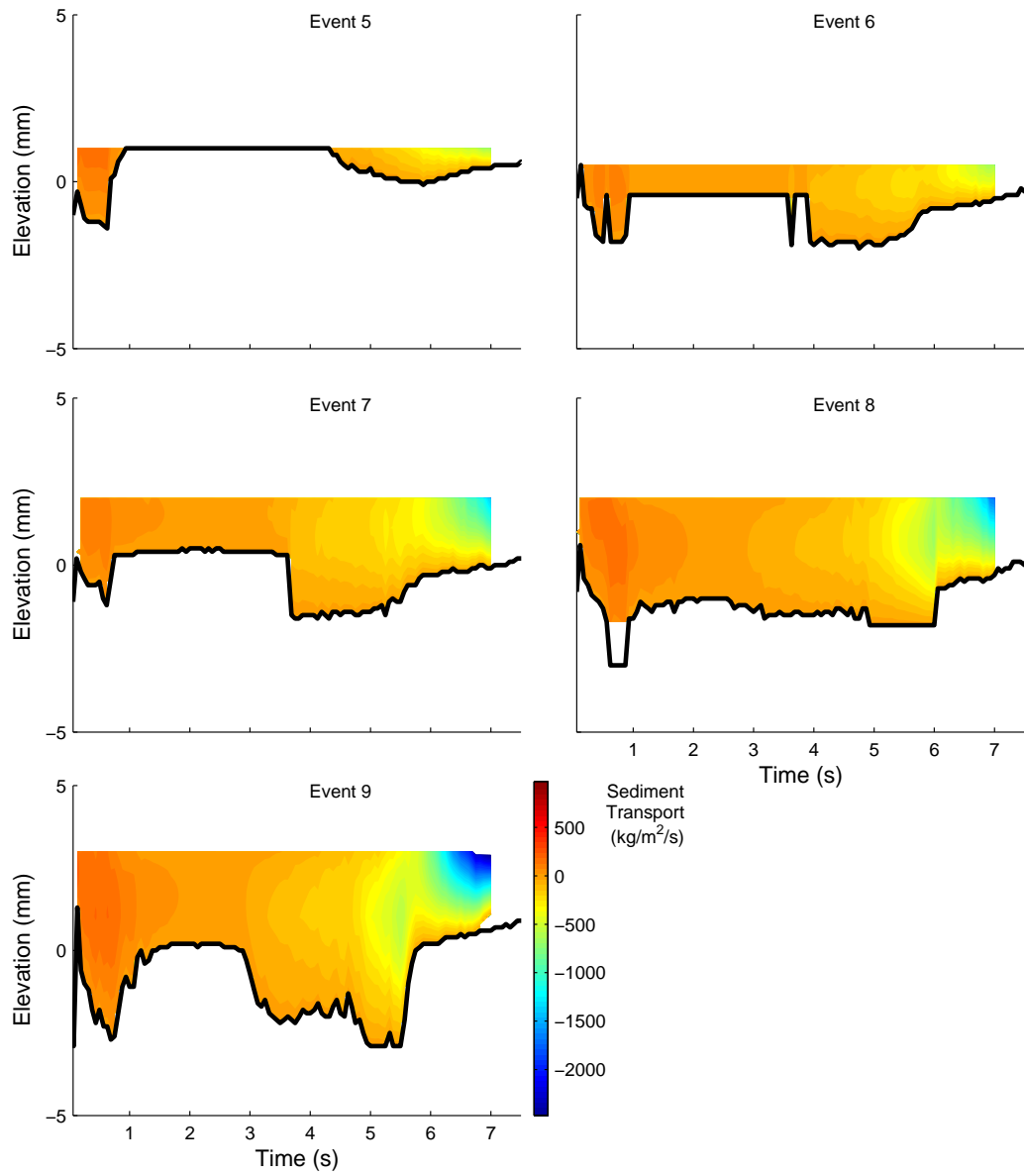
Figure 5.19: The calculated transport profiles by applying the linear velocity boundary layer profiles throughout swash events 5-9 collected at x = 0.90 are shown.

Table 5.4: Total and net sediment transport values calculated using the linear velocity profile for each event at x = 0.90 m.

Event	Onshore Transport (kg/m)	Offshore Transport (kg/m)	Net Transport (kg/m)
1	0.0118	(-) 0.1700	- 0.1582
2	0.0391	(-) 0.1760	- 0.1369
3	0.0288	(-) 0.3303	- 0.3015
4	0.1344	(-) 1.2573	- 1.1229
5	0.1128	(-) 0.3452	- 0.2324
6	0.1043	(-) 0.8490	- 0.7447
7	0.1727	(-) 2.2283	- 2.0556
8	0.4251	(-) 3.1091	- 2.6840
9	0.5991	(-) 4.8085	- 4.2094

5.4.1 Transport Profile Comparisons

The same trends are observed in the transport estimations using the logarithmic velocity profiles (Appendix A-1 contains figures showing all instantaneous tranport profiles for every swash event using both logarithmic velocity profiles). However, the magnitudes of the transport for the logarithmic cases are significantly higher due to the higher velocities near the instantaneous bed. Figure 5.20 shows the difference between the sediment transport profile calculated using the linear velocity boundary layer profile and the transport profile calculated using either logarithmic profiles ($k_s = 0.44$ mm and k_s - 3.67 mm) in the left and right plots, repectively. The top and bottom plots correspond to representative swash events from x = 0.90 m and x = 0.37 m. The magnitude of the differences in instantaneous transport for all cases over most of the instantaneous profile are significantly large, particularly at the end of backwash as the magnitude of free stream velocity increases continuously until the end of the signal. The magnitude of these differences are larger for $k_s = $ 0.44 mm (up to -1,230 kg/m^2/s and -1,650 kg/m^2/s, at x = 0.90 m and x = 0.37

m, respectively) than for $k_s = 3.67$ mm (up to -865 kg/m²/s and -1,025 kg/m²/s). The largest differences between onshore transport (occuring at the start of the cycle when onshore velocity is greatest) are much less. Again, the magnitude of the differences in onshore transport are larger for $k_s = 0.44$ mm (up to 735 kg/m²/s and 575 kg/m²/s, at x = 0.90 m and x = 0.37 m, respectively) than for $k_s = 3.67$ mm (up to 545 kg/m²/s and 335 kg/m²/s, at x = 0.90 m and x = 0.37 m, respectively).

In the direct vicinity of the bed (from about 0.2 - 0.3 mm above the instaneous bed to the instantaneous bed) the differences in transport approaches zero since velocities equal zero at the bed level for all boundary layer profiles. For the $k_s = 3.67$ mm velocity profile, the velocity equals zero $\frac{k_s}{30} = 0.12$ mm above the instantaneous bed to the instantaneous bed. Therefore, the linear profile predicts greater transport magnitudes from 0.2 mm above the instantanoues bed to the instantaneous. The magnitude of these differences are small in comparison to the rest of the instantaneous transport profile and occur over a small elevation (2 grid points) such that their effect is miniscule when the profiles are summed over the entire depth.
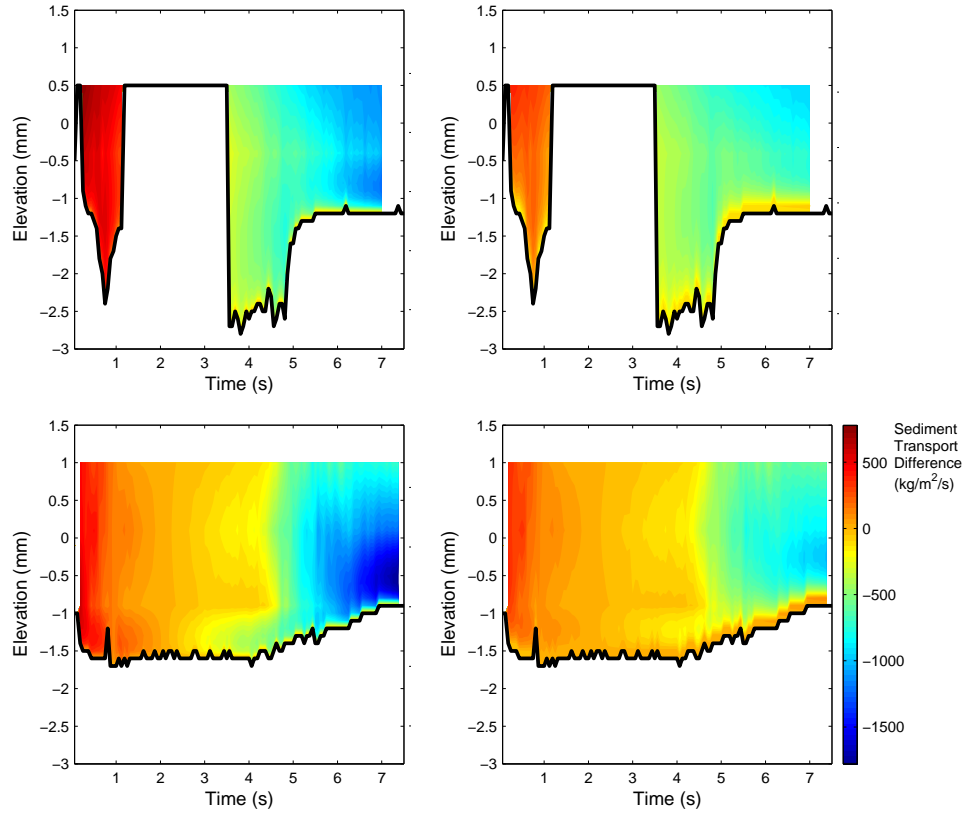
Figure 5.20: The plots show the differences between the sediment transport profiles calculated using the linear boundary layer profile and those calculated using the boundary layer corresponding to the Law of the Wall (logarithmic boundary layer profiles). The left and right show the differences between either logarithmic profiles and the linear profile, ($k_s = 0.44$ mm and $k_s = 3.67$ mm) respectively. The top plots show data from representative swash event (Event 4) at x = 0.90 m and the bottom plots show data (Event 4) from x = 0.37 m.

The sediment transport profile differences between the two values of k_s are shown in Figure 5.21. As expected, the magnitudes of transport for the velocity profile corresponding to the smaller k_s are greater. Again, the differences are greatest at the end of backwash when the approximated free stream velocity is the greatest. Unlike magnitudes of the transport differences between the linear and logarithimic

profiles, the difference between the two logarithmic profiles are largest over a small portion of the instantaneous profile near the bed (0.1 mm to 0.5 mm above the bed). Further away from the bed, the transport profile differences approach zero as the velocity profiles converge.
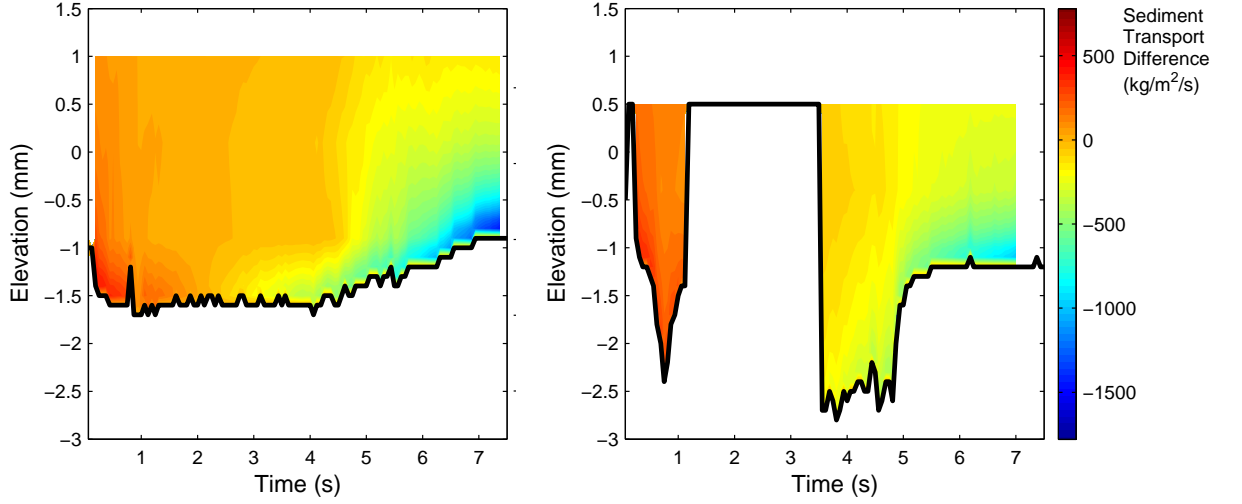
Figure 5.21: The plots show the difference in the sediment tansport profile due to different values of k_s. The left and right show the difference between the sediment transport profiles at x = 0.37 m and x = 0.90 m, respectively. The magnitudes of sediment transport are higher for the smaller value of k_s

The following tables (Table 5.5 to 5.8) shows the total onshore and offshore transport as well as the net sediment transport resulting from each logarithmic profile at each cross shore location. The net transport values at x = 0.37 m ranged from -2.2894 kg/m to -12.2339 kg/m and from -4.0173 kg/m to -15.3874 kg/m for $k_s = 3.67$ and $k_s = 0.44$ (Tables 5.5 and 5.7), respectively. The net transport values at x = 0.90 m ranges from -0.2997 kg/m to -9.2429 kg/m and from -0.7300 kg/m to -11.2562 kg/m for $k_s = 3.67$ and $k_s = 0.44$ (Tables 5.6 and 5.8), respectively. The largest difference between the net transport for the different roughness lengths at x

= 0.37 m is 3.2518 kg/m (event 6) and at x = 0.90 m is 2.0133 kg/m (event 9). As expected, the net transport values resulting from the logarithmic velocity profiles are significantly higher than the net transport values corresponding to the linear velocity profile.

Table 5.5: Total and net sediment transport values calculated using the logarithmic (k_s = 3.67 mm) velocity profile for each event at x = 0.37 m.

Event	Onshore Transport (kg/m)	Offshore Transport (kg/m)	**Net Transport** (kg/m)
1	0.7825	(-) 3.0719	- 2.2894
2	0.7853	(-) 4.6198	- 3.8345
3	1.0730	(-) 7.4111	- 6.3382
4	0.6908	(-) 5.6239	- 4.9331
5	1.4137	(-) 11.7115	- 10.2978
6	1.7412	(-) 13.9750	- 12.2339
7	0.8548	(-) 7.3735	- 6.5187

Table 5.6: Total and net sediment transport values calculated using the logarithmic (k_s = 3.67 mm) velocity profile for each event at x = 0.90 m.

Event	Onshore Transport (kg/m)	Offshore Transport (kg/m)	**Net Transport** (kg/m)
1	0.0733	(-) 0.6039	- 0.5306
2	0.2433	(-) 0.5430	- 0.2997
3	0.1769	(-) 1.2344	- 1.0575
4	0.7382	(-) 4.6905	- 3.9523
5	0.5958	(-) 1.2209	- 0.6252
6	0.6036	(-) 3.4668	- 2.8632
7	0.9080	(-) 6.8562	- 5.9482
8	1.9000	(-) 8.7306	- 6.8306
9	2.4346	(-) 11.6774	- 9.2429

Table 5.7: Total and net sediment transport values calculated using the logarithmic (k_s = 0.44 mm) velocity profile for each event at x = 0.37 m.

Event	Onshore Transport (kg/m)	Offshore Transport (kg/m)	Net Transport (kg/m)
1	1.2071	(-) 5.2244	- 4.0173
2	1.2092	(-) 7.2967	- 6.0876
3	1.5696	(-) 10.6637	- 9.0941
4	1.0151	(-) 8.1300	- 7.1150
5	1.9080	(-) 15.1190	- 13.2110
6	2.2509	(-) 17.6383	- 15.3874
7	1.1455	(-) 9.4439	- 8.2985

Table 5.8: Total and net sediment transport values calculated using the logarithmic (k_s = 0.44 mm) velocity profile for each event at x = 0.90 m.

Event	Onshore Transport (kg/m)	Offshore Transport (kg/m)	Net Transport (kg/m)
1	0.1589	(-) 1.3436	- 1.1845
2	0.4189	(-) 1.1489	- 0.7300
3	0.3096	(-) 2.2052	- 1.8956
4	1.0807	(-) 6.6208	- 5.5401
5	0.8853	(-) 2.2275	- 1.3422
6	0.9651	(-) 5.2385	- 4.2733
7	1.3677	(-) 9.1917	- 7.8240
8	2.5282	(-) 11.2890	- 8.7608
9	3.1982	(-) 14.4544	- 11.2562

5.4.2 Beach Profile Change Comparison

The cross shore profiles taken after each swash event for either set provide a means by which the net transport calculations can be roughly validated. Basic mass conservation yields the continuity equation that can be applied to sediment as

$$Q_{in} - Q_{out} = (1 - n)dV_{prof}\rho_s, \tag{5.11}$$

where Q_{in} and Q_{out} are the net mass sediment fluxes into and out of a control volume, dV_{prof} being the change of sediment volume within the same control volume, $n = 0.35$ being the porosity of the sediment, and sediment density, $\rho_s = 2{,}650$ kg/m³. Essentially, the difference between the net transport rates at different cross shore locations is equal to the profile change between the two locations. The sediment continuity equation (Equation 5.11) is illustrated in Figure 5.22.
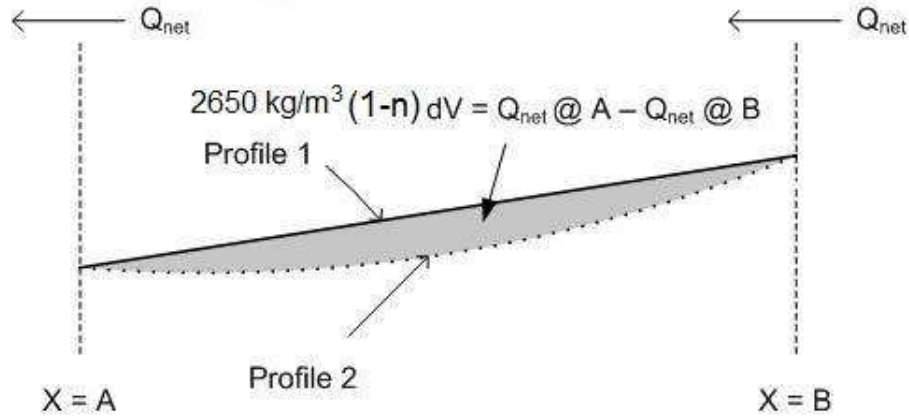
Figure 5.22: Illustration of the sediment continuity equation (Equation 5.11).

The profiles collected after swash events when the sensors were located at x = 0.90 m spanned from x = 0.67 m to x = 1.15 m while the profiles collected after swash events when the sensors were located at x = 0.37 m spanned from x = 0.12 m to x = 0.65 m. As previously mentioned, the profiles were collected before the first wave was ran and then after each individual event (Therefore, 11 total profiles were measured around x = 0.90 m and 8 were measured around x = 0.37 m). The profiles measured from each set that corresponded to one another (i.e. profile after wave 1 for either location) were combined to form a composite profile which spanned the space between the two locations.

The difference between subsequent profiles is used to calculate the volume change between the two cross-shore locations of interest (x = 0.37 - 0.90 m) per unit

length in the longshore direction. Ideally, transport measurements would have been collected at two locations simultaneously. If this was the case the measured profile change should correspond exactly to the difference between the net transport across the two locations. Unfortunately, this was not the case; the profile measurements are composite measurements to account for the application of transport measurements made at different times (events). The composition of the profiles eliminate some of the error associated with applying measurements taken at different times which would require exact repeatability. The profile evolution, to the first order, was basically repeatable as was the initial profile. Therefore, the profile comparisons can provide a check for order of magnitude and, certainly, the direction associated with the difference of net transport calculations at the two cross shore locations.

The average profile change per swash event was calculated by finding the difference between the initial composite profile (P0, represented by the black circles in Figure 5.23) and final (after 7 waves, P7, represented by the red circles in Figure 5.23) composite profile and dividing by the number of waves (N = 7) at each cross shore location of profile measurement (x_i), thus obtaining an average profile elevation change (dv_i) at each cross shore location. Because the distance meter used to collect profile elevations is 1.6 mm precise, each profile elevation is $\pm$ 1.6 mm accurate. Therefore, the error bounds of each profile elevation change is $\pm$ 3.2 mm (additive error).

$$dv_{av,i} = \frac{(P_7@x_i - P_0@x_i) \pm 3.2mm}{7} \tag{5.12}$$

The average profile changes at each cross shore locations were then used to calculate the mean profile volume change per swash event. The cross shore locations are bounded by the sensor locations ($x_1 = 0.37$ m and $x_I = 0.90$ m, denoted by the blue stars in Figure 5.23).

$$\Delta V_{av} = \sum_{i=1}^{I-1} \frac{dv_{av,i} + dv_{av,i+1}}{2}(x_{i+1} - x_i) \tag{5.13}$$

The average profile change eliminates the variable profile change from event to event. For example, it is quite likely that the profile erodes more during the third event than the second event. To investigate this variability, the profile elevation change $dv_{j,i}$ due to each individual event (j) was calculated at each x_i. The profile elevations were then used to calculate the profile volume change during each event (j).

$$dv_{j,i} = (P_j@x_i - P_{j-1}@x_i) \pm 3.2mm \tag{5.14}$$

$$\Delta V_j = \sum_{i=1}^{I-1} dv_{j,i} + dv_{j,i+1} \pm 3.2mm(x_{i+1} - x_i) \tag{5.15}$$
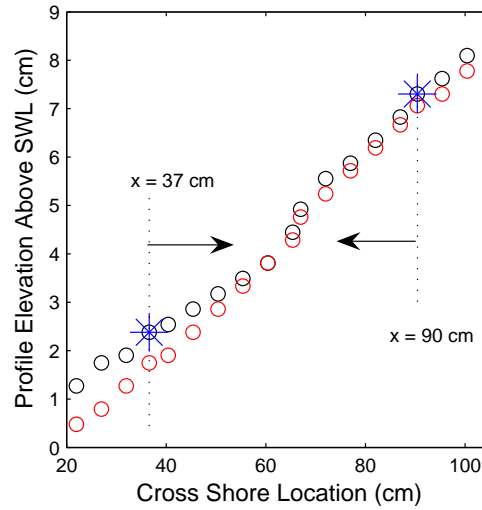
Figure 5.23: In the plot, the black circle represents the initial composite beach profile before any waves were generated (P_0) and the red circle represents the composite beach profile after the last (seventh) swash event (P_7). The blue stars mark the cross shore location of the sensors during data collection.

The volumetric profile changes were converted to mass of sediment eroded or accreted using Equation 5.11. The left plot in Figure 5.24 shows the comparison of

113

the mass of sediment eroded (-) or acreted (+) for each swash event and the mean mass of sediment eroded (-) over all swash events based on measured profile changes. The largest erosion measured was (-)0.9830 kg resulting from the second swash event while the greatest mass acretion measured was (+)0.3514 kg resulting from the first event. The large error bounds on each individual event correspond to the $\pm$ 3.2 mm possible error over the entire profile. The error bounds (represented by the blue dashed lines) on the average mass of sediment eroded (represented by the solid blue line) corresponds to the possible error due to the precision of the instrument averaged over 7 measurements. Only two of the erosion/acretion measurements for an individual event (events 5 and 6) are within the error band of the mean profile erosion. The mean erosion measured was -0.3459 $\pm$ 0.4141 kg.

The variability in net erosion/acretion from wave to wave is most likely attributable to the accuracy and precision of the profile measurement rather than actual differences. This affect is evident in mass change measurements for events 1 and 3. According to these measurements, the profile acreted, yet, it was clearly observed that the profile eroded slightly after every event. The fact that for the events that follow the acretion measurements (events 2 and 4), the erosion lies outside the error bound of the mean reflects the additive error that accumulates for each individual measurement. Due to this lack of precision and accuracy, the average profile erosion is most appropriate for comparing the transport calculations.

In order to compare profile measurements with the calculated net transport difference, swash events for which the sensor height at each location was the same relative to the initial bed level must be compared. Further, these events must be such that the sensors were close enough to the at rest bed to detect the dominant transport signal (as shown previously, in the earlier events the sensors were seemingly too deep to capture the dominant sediment mobilization). Based on this criteria, comparing events 6 and 9, 5 and 8, and 4 and 4, from x = 0.37 m and x = 0.90

m seems reasonable. The sensor elevation for the highest concentration sensor for these sets were 0.003 m and 0.003 m, 0.002 m and 0.0025 m, and 0.001 m and 0.0005 m, respectively.

The left plot in Figure 5.24 shows the net transport differences between x = 0.37 m and x = 0.90 m for different events along with the average sediment erosion predicted by the profile measurements. The linear velocity profile calculations best agrees with the profile measurement estimates. Of the three profile changes calculated based on net flux differences, two of the linear velocity profile estimates lie within the error bounds of the average erosion from the profile measurements. The agreement for the linear velocity profile ranges from a factor of 1.11 to 4.6554. The logarithmic velocity profile with $k_s = 0.44$ mm agrees least with the profile measurement estimates with agreement from a factor of 4.55 to 12.87. This is expected since the transport magnitudes increase from the linear to log profiles due to the larger magnitudes of velocity near the bed for the log profiles. Therefore, the difference between the transport rates scales between the different velocity profiles. In all cases, the net transport differences overpredict the average measured erosion. Table 5.9 shows the calculated mass loss from the calculated net sediment transport differences.
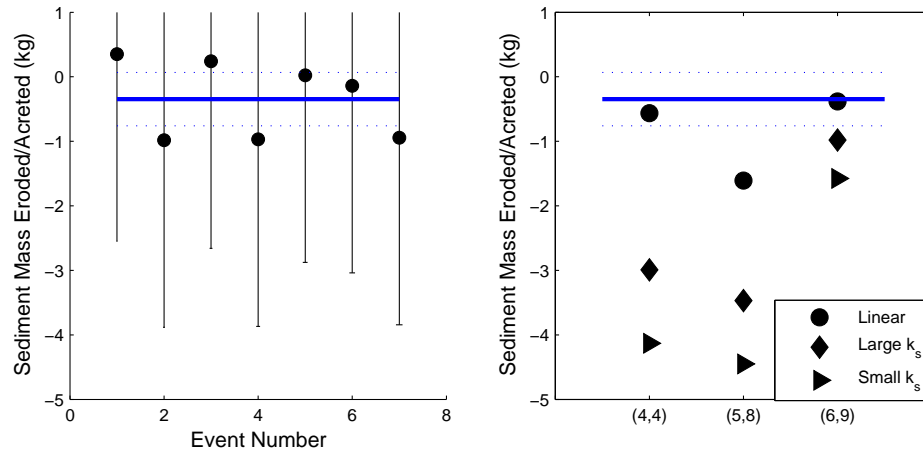
Figure 5.24: The left plot shows the mass eroded or acreted based on the profile measurements. The black circles represent the total erosion/acretion for each individual event and the error bars representing the error-bounds on each measurement. The solid blue line (in either plot) represents the average erosion over 7 events. The dashed blue lines (in either plot) represent the error bounds on the average erosion. The right plot shows a comparison between the calculated net transport differences for events (i,j) where i and j are the event numbers from x = 0.37 m and x = 0.90 m, respectively. The different symbols correspond to the estimates from the different velocity profiles.

Table 5.9: The numeric entries in the table represent the calculated mass loss between x = 0.37 m and x = 0.90 m based on Equation 5.11 in kg/m in the longshore direction. The rows correspond to the events (i,j) used for comparison where i and j are the event numbers from x = 0.37 m and x = 0.90 m, respectively. The columns correspond to the different boundary layer velocity profiles.

|	Velocity Profile		
	Linear	Log $(k_s = 3.67$ mm)	Log $(k_s = 0.44$ mm)
Events (6,9)	-0.3823	-0.9808	-1.5749
Events (5,8)	-1.6093	-3.4679	-4.4502
Events (4,4)	-0.5636	-2.9910	-4.1312

Chapter 6

CONCLUDING REMARKS

What is thought to be the first measurements of sediment concentration within 0.005 m of and below the instantaneous bed in the swash zone since the limited data present by Yu et al. (1990) has been presented. This task has proved its difficulty and the development of an adequate sensor to measure nearbed concentration profiles (CCP) is not complete. Over the past few years, a succession of prototypes have been built and tested. This process has yielded a sensor that is robust, clearly detects varying concentrations of sediment, produces repeatable results in simple tests, and collects independent measurements at different elevations simultaneously. The most essential improvement required is to eliminate the scour effects on the concentration measurements.

This next step can be approached in two ways. The first approach is to eliminate scour around the CCP by reducing its size and/or modifying its shape. Reducing its size alone is not likely to completely eliminate scour since the placement of any sensor that is rigid and much larger than the sediment grain size (which the CCP must be in order to house several electrode pairs each with a proper spacing to measure over an appropriate volume) would effect the local flow field. Shrinking the sensors size and making it more streamlined to reduce adverse pressure gradients along the CCP body could practically eliminate scour. For example, a CCP body that is an ellipse with tappered edges (like an 'eye' shape) with its major axis (oriented in the flow direction) being much longer than the minor axis, which is as

small as possible, would be much less prone to scour than the current body shape. Since reducing scour to the point that it is practically non-existant may prove too difficult, the second approach is to mitigate the scour effects on the measurements. For example, the CCM's (about which scour certainly occurs) pins are oriented such that the scour about the body of the sensor seemingly does not interfere with the sensing volume. This can achieved by displacing the sensing electrode from the body of the sensor. Recall that early prototypes had electrodes that consisted of uncoated ends of wires that protruded through the body of the CCP. The inadequency of this design was that the coating could fray off the wire and the wires could bend changing electrode geometry and spacing. By using small, rigid conduits (possibly hyperdermic needles) through which each electrode wire runs and at the end of which the exposed electrode is located, it would be possible to remove the electrode from the CCP body without concern of maintaining electrode spacing and geometry. A dense grid of electrode conduits would likely cause scour in addition to the scour about the body of the sensor. Therefore, offsetting the electrode displacement from one another and/or putting electrodes on either side of the CCP (Figure 6.1), might be necessary. These offsets may effect the true profiling capability of the CCP since they would not be in the same alongshore plane. However, the offsets would likely not have to be more than 0.005 m and is therefore a great improvement over using CCMs spaced 0.05 m or greater.
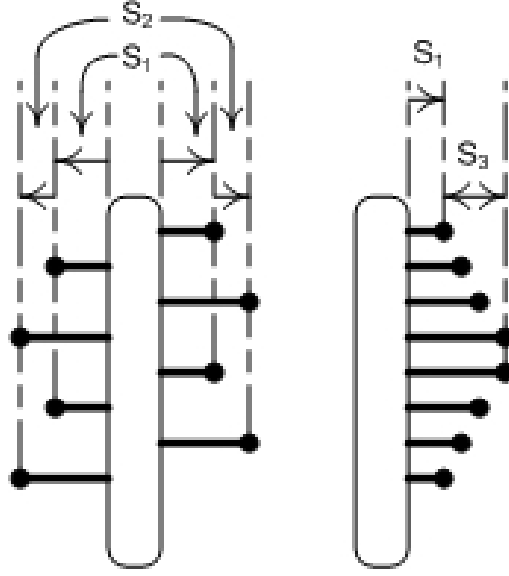
Figure 6.1: The sketches show future prototype design ideas that have the electrodes displaced from the body. The right sketch has electrodes displaced to either side of the CCP (with S_1 and $S_2 \leq O(0.005$ m)) while the left sketch has the electrodes displaced on the same side and offset from one another relative to a vertical plane (with with $S_1 \leq O(0.005$ m) and $S_3 \leq O(0.01$ m)).

Another essential improvement, for the sake of transport measurements, is obtaining velocity *profile* measurements near the bed simultaneously with the concentration measurements. The discrepancy between transport calculations from three simple boundary layer profiles were significant with the linear boundary being 5 - 8 times smaller than logarithmic calculations. There are no measurements made to validate one choice of a boundary layer over the others. None of the assumed velocity profile replicates the actual velocity profile through a mobilized sea bed, which is likely highly non-linear due to momentum transfer between sand grains and the fluid. Additionally, due to the physical limitations of the EMCMs, the velocity measurements were limited to portions of the swash cycle when swash depths were greater than 0.15 - 0.20 m while the dominant portion of the transport signal

119

occurs at the end of backwash when depth is 0.10 m or less. Therefore, a significant component of the net transport relies on an extrapolated velocity in addition to an idealized boundary layer profile. Further still, the accurate measurements of fluid velocity near the bed may not accurately approximate the actual sediment velocity, particularly in the sheet flow and bedload layer, since momentum is transfered from grain to grain in addition to momentum from the fluid to the grains. Therefore, the inadequency of current technology to measure sediment velocity profiles near the bed is likely to be the ultimate limitation on measuring accurate transport rates.

Another implication of the lack of velocity measurements within O(0.001 m) of the bed level is that the end of the transport signal poorly represents the actual sediment transport at the end of a swash cycle. The swash cycle was ended based on when the depth was less than that at which the concentration signal showed that the bed was begining to settle. This resulted in velocities and transport rates that abruptly ended after monotonically increasing. Such a discontinuity is physically unrealistic. The actual velocity and transport rates increase to a maximum during backwash before decreasing to zero rather than abruptly terminating. The velocity signal was not decreased to zero because no measurements were made from which this decrease in velocity could be approximated.

Further, there is an inclination for the sediment concentration to be over predicted by the CCMs. Since the CCM pins have a length associated with them and are oriented perpendicular to the bed, the CCMs resolution in the vertical is much coarser than the CCP. It was observed that before some events the pins of a CCM were slightly exposed leading to a reduction in the conductivity logged relative to the packed bed. The magnitude of this deviation from the packed bed, of course, depended on how much of the CCM's pins were exposed until they were finally fully exposed and recorded the null value corresponding to air. It was also frequently observed that the profile acreted at the sensor location during uprush before eroding

away during backwash. In many cases, the CCM pins were completely exposed before the swash event but were only partially exposed during flow reversal. This likely led to measurements of concentrations between 0.65 m^3/m^3 and 0 m^3/m^3 since the pins spanned the bed/water interface. During other parts of the cycle, as the bed dialated, it is possible that part of the CCM's pins were in the mobile bed layer while the other portions were in the packed bed or region of higher concentration (Figure 6.2). This tendency for the CCMs to overpredict sediment concentrations is also evident in the comparison between the concentration profile detected by the CCP and that detected by the CCMs (Chapter 4). Sediment concentrations detected by the CCMs during the same swash event were much greater than concentrations detected by the CCP. Though, one reason for this is scour, the fact that the CCMs have larger measuring volumes is likely an additional reason for the disagreement.
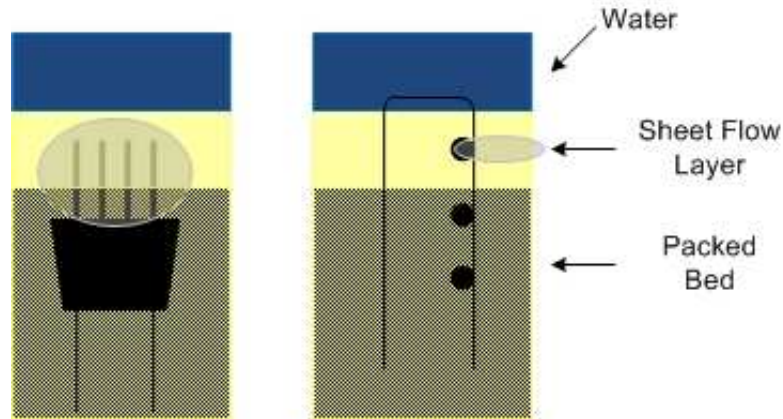
Figure 6.2: The sketches the theoretical sensing volumes (the transparent elipses) of the CCM (left) and the CCP (right) relative to the instantaneous interface between the packed bed and bedload/ sheet flow layer.

The transport calculations using a linear velocity boundary layer best agreed with the rough profile change measurements. The reason for this can be explained qualitatively. As previously mentioned, it is likely that the velocity extrapolation

over predicted actual velocity towards the end of the backwash as frictional forces become more dominant. Also, towards the end of backwash, when depth is shallow, the boundary layer likely extends through, rather than to, the free surface. Further, the Law of the Wall treatment assumed a fluid of uniform (clear water) density flowing over a rough surface. In actuallity, the fluid flowing over the instantaneous bed is a slurry of water and high sediment concentrations. The linear decay in velocity accounted for the over prediction of free stream velocity while the over prediction was propagated closer to the bed for the logarithmic case. The differences in predicted erosion based on net transport differences highlight the difficulty associated with the fact that net sediment transport is a small difference between two large quantities (uprush transport - backwash transport) [40].

BIBLIOGRAPHY

[1] J.A. Puleo, R. A. Beach, R.A. Holman, and J.S. Allen. Swash zone sediment suspension and transport and the importance of bore-generated turbulence. *Journal of Geophysical Research*, 105:17021–17044, 2000.

[2] R.G. Dean and R.A. Dalrymple. *Coastal Processes with Engineering Applications*. Cambridge University Press, 2002.

[3] J. Hardisty. A morphodynamic model for beach gradients. *Earth Surface Processes and Landforms*, 11:327–333, 1986.

[4] T. Butt and P. Russell. Hydrodynamics and cross-shore sediment transport in the swash-zone of natural beaches: A review. *Journal of Coastal Research*, 16(2):255–268, 2000.

[5] T. Sunamara. Onshore-offshore sediment transport rate in the swash zone of laboratory beaches. *Coastal Engineering Japan*, 27:205–212, 1984.

[6] J.A. Puleo, K.T. Holland, N. Plant, D.N. Slinn, and D.M. Hanes. Fluid acceleration effects on suspended sediment transport in the swash zone. *Journal of Geophysical Research*, 108 (C11):3350, 2003.

[7] T Butt and P. Russell. Suspended sediment transport mechanisms in high-energy swash. *Marine Geology*, 1999:361 – 375, 161.

[8] G. Masselink and P. Russell. Flow velocities, sediment transport and morphological change in the swash zone of two contrasting beaches. *Marine Geology*, 227:227–240, 2006.

[9] N. Kobayashi and M.T. Poff. Numerical model RBREAK2 for random waves on impermeable coastal structures and beaches. Technical report, Center for Applied Coastal Research, University of Delaware, Newark, Delaware, 1994.

[10] B. Raubenheimer. Observations and predictions of fluid velocities in the surf and swash zones. *Journal of Geophysical Research*, 107, C11:3190, 2002.

[11] P. Lin and W. Xu. Newflume: A numerical water flume for two-dimensional turbulent free surface flows. *Journal of Hydraulic Research*, 44:247–255, 2005.

[12] J.A. Puleo, A. Farhadzadeh, and N. Kobayashi. Numerical simulation of swash fluid accelerations. *Journal of Geophysical Research*, 112:C07007, 2007.

[13] E.A. Zedler and R.L. Street. Nearshore sediment transport: Unearthed by large eddy simulation. In *International Conference on Coastal Engineering*, pages 2504–2516. ASCE, 2002.

[14] J.A. Bailard. An energetics total load sediment transport model for a plane sloping beach. *Journal of Geophysical Research*, 86 (C11):10,938 – 10,954, 1981.

[15] J.A. Puleo and K.T. Holland. Estimating swash zone friction coefficients on a sandy beach. *Coastal Engineering*, 43:25–40, 2001.

[16] D.C. Conley and J.G. Griffin. Direct measurements of bed stress under swash in the field. *Journal of Geophysical Research*, 109:C03050, 2004.

[17] N.L. Jackson, G. Masselink, and K.F. Nordstrom. The role of bore collapse and local shear stresses on the spatial distribution of sediment load in the uprush of an intermediate-state beach. *Marine Geology*, 203:109–118, 2004.

[18] J.M. Alsina, S. Falchetti, and T.E. Baldock. Measurements and modelling of the advection of suspended sediment in the swash zone by solitary waves. *Coastal Engineering*, 56:621–631, 2009.

[19] G. Masselink and J.A. Puleo. Swash-zone morphodynamics. *Continental Shelf Research*, 26:661–680, 2006.

[20] N. Kobayashi and B.D. Johnson. Sand suspension, storage, advection, and settling in surf and swash zones. *Journal of Geophysical Research*, 106 (C5):9363–9376, 2001.

[21] D.P. Horn. Measurements and modelling of beach groundwater flow in the swash-zone: a review. *Continental Shelf Research*, 26 (5):622–652, 2006.

[22] J. Miles, T. Butt, and P. Russell. Swash zone sediment dynamics: A comparison of a dissipative and an intermediate beach. *Marine Geology*, 231:181–200, 2006.

[23] R.A. Beach, R.W. Sternberg, and R. Johnson. A fiber optic sensor for monitoring suspended sediment. *Marine Geology*, 103:513–520, 1992.

[24] M.G. Hughes. Application of a non-linear shallow water wave theory to swash following bore collapse on a sandy beach. *Journal of Coastal Research*, 8:562–578, 1992.

[25] K.C. Wilson. Analysis of bed-load motion at high shear stress. *Journal of the Hydraulic Division*, 113:97–103, 1987.

[26] D.P. Horn and T. Mason. Swash zone sediment transport modes. *Marine Geology*, 120:309–325, 1994.

[27] Z.H. Yu. Site investigation on sand concentration in the sheetflow layer. In *Proceedings of the 22nd International Conference on Coastal Engineering, ASCE*, 1990.

[28] P.D. Osborne and G. Rooker. Sand re-suspension events in a high-energy infragravity swash zone. *Journal of Coastal Research*, 15 (1):74–86, 1999.

[29] J.E. Dick and J.F. Sleath. Velocities and concentrations in oscillatory flow over beds of sediment. *Journal of Fluid Mechanics*, 233:165–196, 1991.

[30] K. Horikawa, A. Watanbe, and S. Katori. Sediment transport under sheet flow conditions. In *17th International Conference on Coastal Engineering*. World Scientific, 1982.

[31] T. O'Donoghue and T. Wright. Flow tunnel measurements of velocities and sand fluw in oscillatory sheet flow for well-sorted and graded sands. *Coastal Engineering*, 51:1163–1184, 2004.

[32] J.S. Ribberink and Al-Salem A.A. Sheet flow and suspension of sand in oscillatory boundary layers. *Coastal Engineering*, 25:205–225, 1995.

[33] M. Dohmen-Janssen and D.M. Hanes. Sheet flow dynamics under monochromatic nonbreaking waves. *Journal of Geophysical Research*, 107:1–21, 2002.

[34] M. Treu. Operation of full-wave bridge rectifier. Web Presentation, 2002.

[35] S.K Chua, J.W. Cleaver, and A. Millward. The measurement of salt concentration in a plume using a conductivity probe. *Journal of Hydraulic Research*, 25:171–180, 1986.

[36] F. Ncube, E.G. Kastrinakis, S.G. Nychas, and K.E. Lavdakis. Drifting behavior of a conductivity probe. *Journal of Hydraulic Research*, 29:643–655, 1991.

[37] K. Voloudakis, P. Vrahliotis, E.G. Kastrinakis, and S.G. Nychas. The behaviour of a conductivity probe in electrolytic liquids/solid suspensions. *Measurement Science Technology*, 10:100–105, 1999.

[38] C.H. Gibson and W.H. Schwarz. Detection of conductivity fluctuations in a turbulent flow field. *Journal of Fluid Mechanics*, 16:356–364, 1963.

[39] M.C. Gregg, T.B. Meagher, E.E. Aagaard, and W.C. Hess. A salt-stratified tank for measuring the dynamic response of conductivity probes. *IEEE Journal of Ocean Engineering*, OE-6(4):113–118, 1981.

[40] K.D. Hill and D.J. Woods. The dynamic response of the two-electrode conductivity cell. *IEEE Journal of Ocean Engineering*, 13(3):118–123, 1988.

[41] Instituition of Civil Engineers. *Manual of Applied Geology for Engineers.* Thomas Telford, 1976.

[42] J. Boussinesq. Theorie des ondes et des remous qui se propagent le long d'un canal rectangulaire horizontal, en communiquant au liquide contenu dans ce canal de vitesses sensiblement parreilles de la surface au fond,". *Journal de Mathematiques Pures et Appliquees, 2nd Series*, 17:55–108, 1872.

[43] D.G. Goring. *Tsunamis–The Propagation of Long Waves onto a Shelf.* PhD thesis, California Institute of Technology, 1978.

[44] C.E. Synolakis. *The Runup of Long Waves.* PhD thesis, California Institute of Technology, 1986.

[45] J. Calantoni and J.A. Puleo. Role of pressure gradients in sheet flow of coarse sediments under sawtooth waves. *Journal of Geophysical Research*, 111:C01010, 2005.

[46] M.G. Hughes. Friction factors for wave uprush. *Journal of Coastal Research*, 11 (4):1089–1098, 1995.

[47] H.A. Einstein. The bed-load function for sediment transport in open channel flows. Technical Report 1026, US Dept. Agriculture. Soil Conservation Service, 1950.

[48] F. Engelund and E. Hansen. Teknisk forlag. Copenhagen, Denmark, 1967.

[49] K. Mahmood. Water Management Technical Report. Technical report, Colorado State University, 1971.

[50] P. Ackers and W. White. Sediment transport: new approach and analysis. *Journal of Hydraulics Division 99*, HY11:2041–2060, 1973.

[51] J.W. Kamphius. Friction factor under oscillatory waves. *Journal of the Waterways, Harbors, and Coastal Engineering*, 101:135–144, 1975.

[52] R.D. Hey. Flow resistance in gravel-bed rivers. *Journal of the Hydraulics Division*, 105 (HY4):365–379, 1979.

[53] L.C. Van Rijn. Equivalent roughness of alluvial bed. *Journal of the Hydraulics Division*, 108 (HY10):1215–1218, 1982.
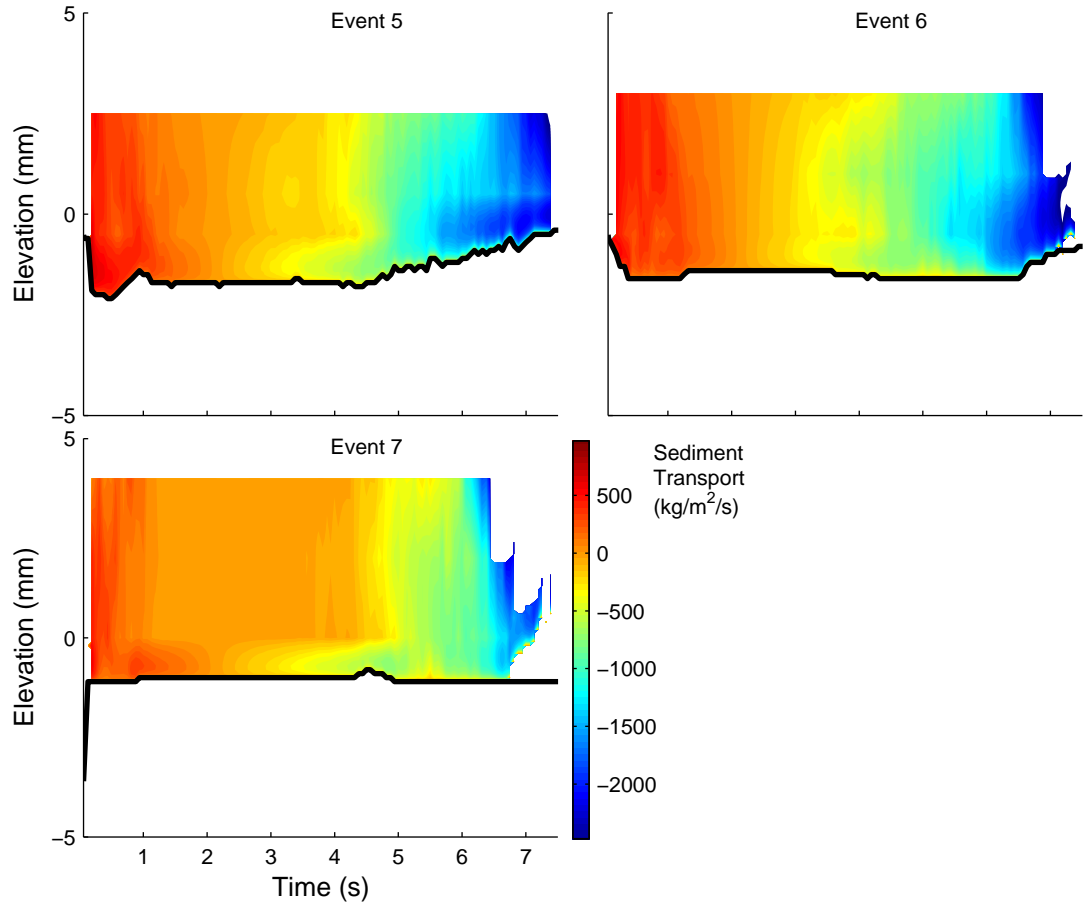
Appendix A

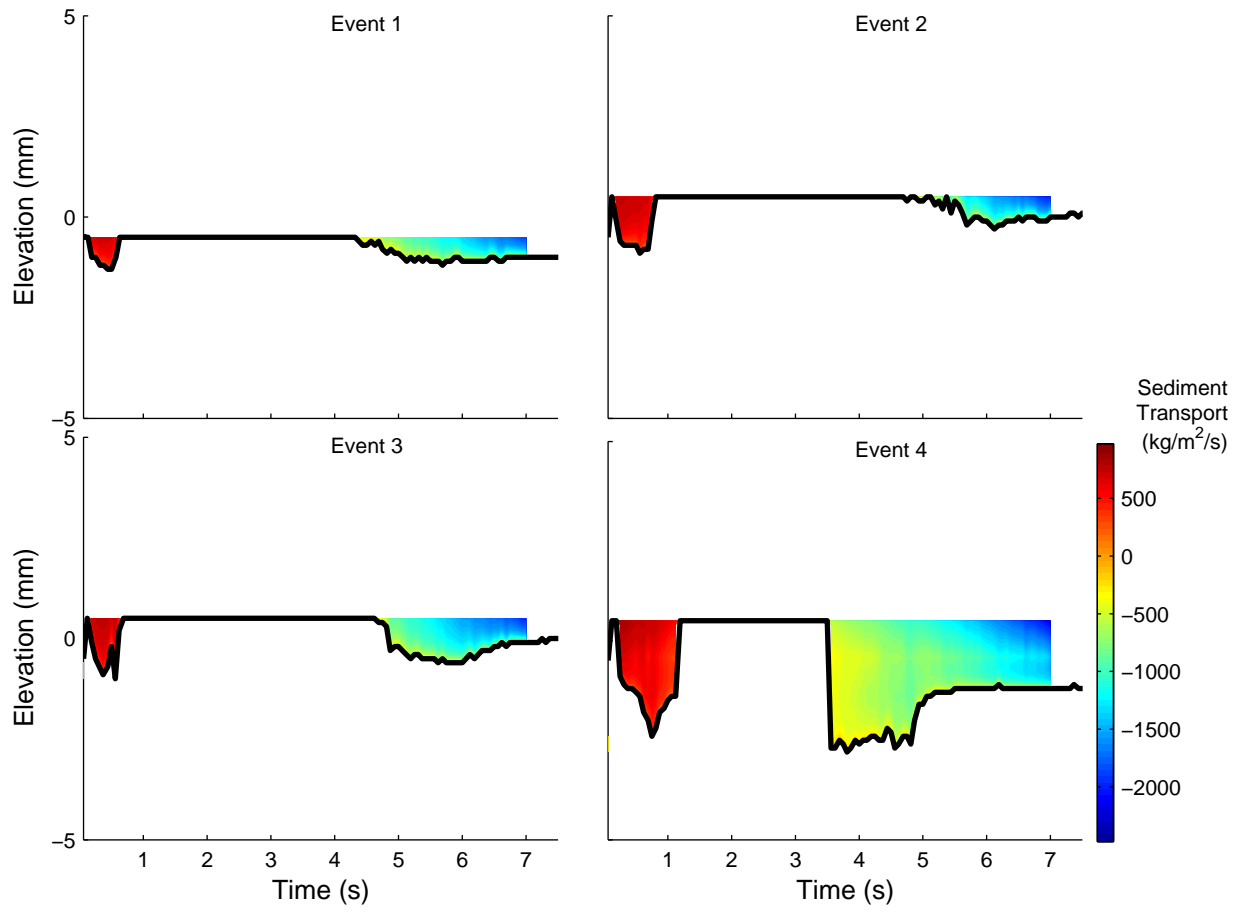# INSTANTANEOUS TRANSPORT PROFILES USING LOGRITHMIC VELOCITY PROFILES

A.1 $k_s = 0.44$ mm

The figures in this section show the instantaneous sediment transport profiles for each swash event at either cross shore location (x = 0.37 m and x = 0.90 m) using the logrithmic velocity profile corresponding to $k_s = 0.44$ mm.
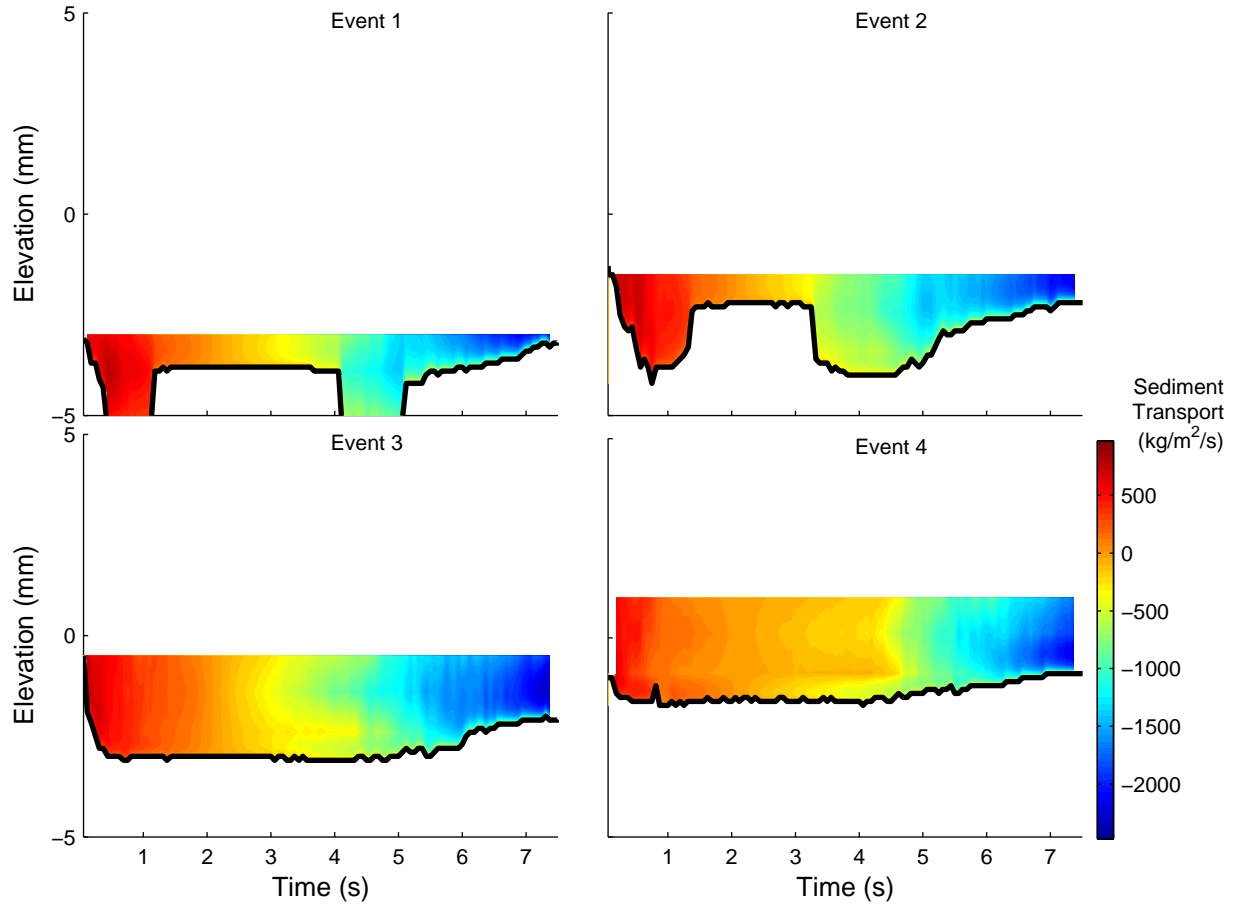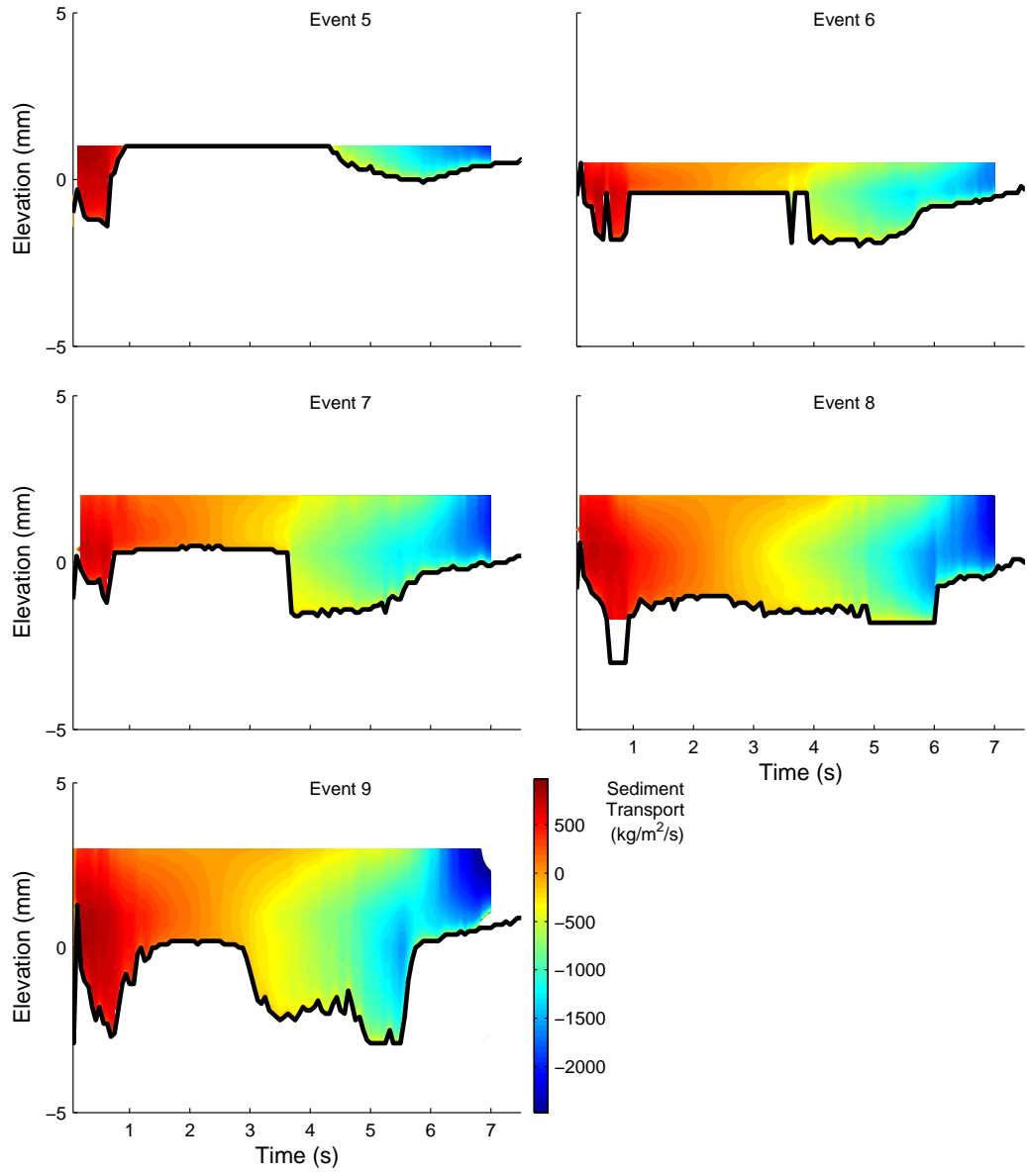
Figure A.1: The calculated transport profiles by applying the logarithmic ($k_s = 0.44$ mm) boundary layer profiles throughout swash events 1-4 collected at x = 0.37 are shown.
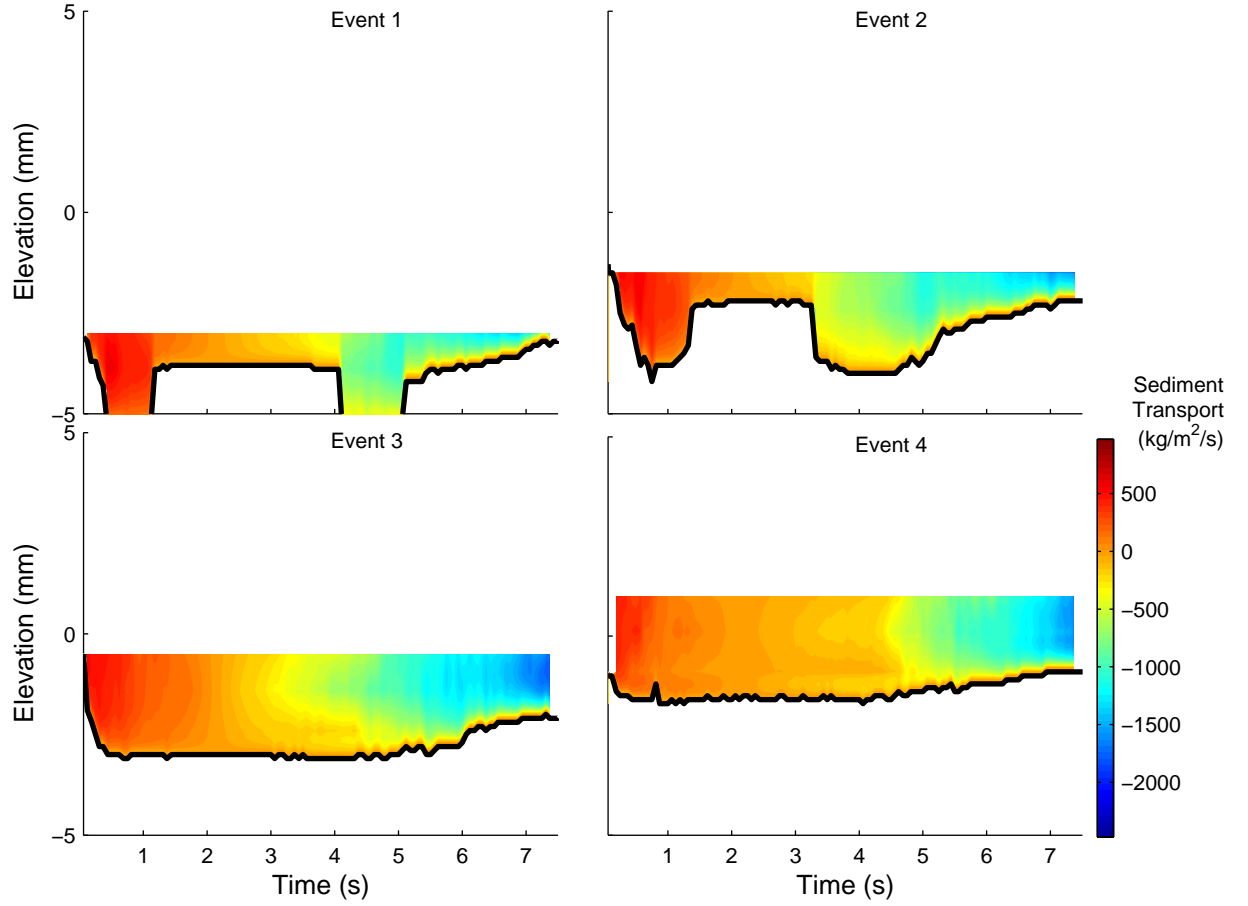
Figure A.2: The calculated transport profiles by applying the logarithmic ($k_s = 0.44$ mm) velocity boundary layer profiles throughout swash events 5-7 collected at x = 0.37 are shown.

Figure A.3: The calculated transport profiles by applying the logarithmic ($k_s = 0.44$ mm) velocity boundary layer profiles throughout swash events 1-4 collected at x = 0.90 are shown.
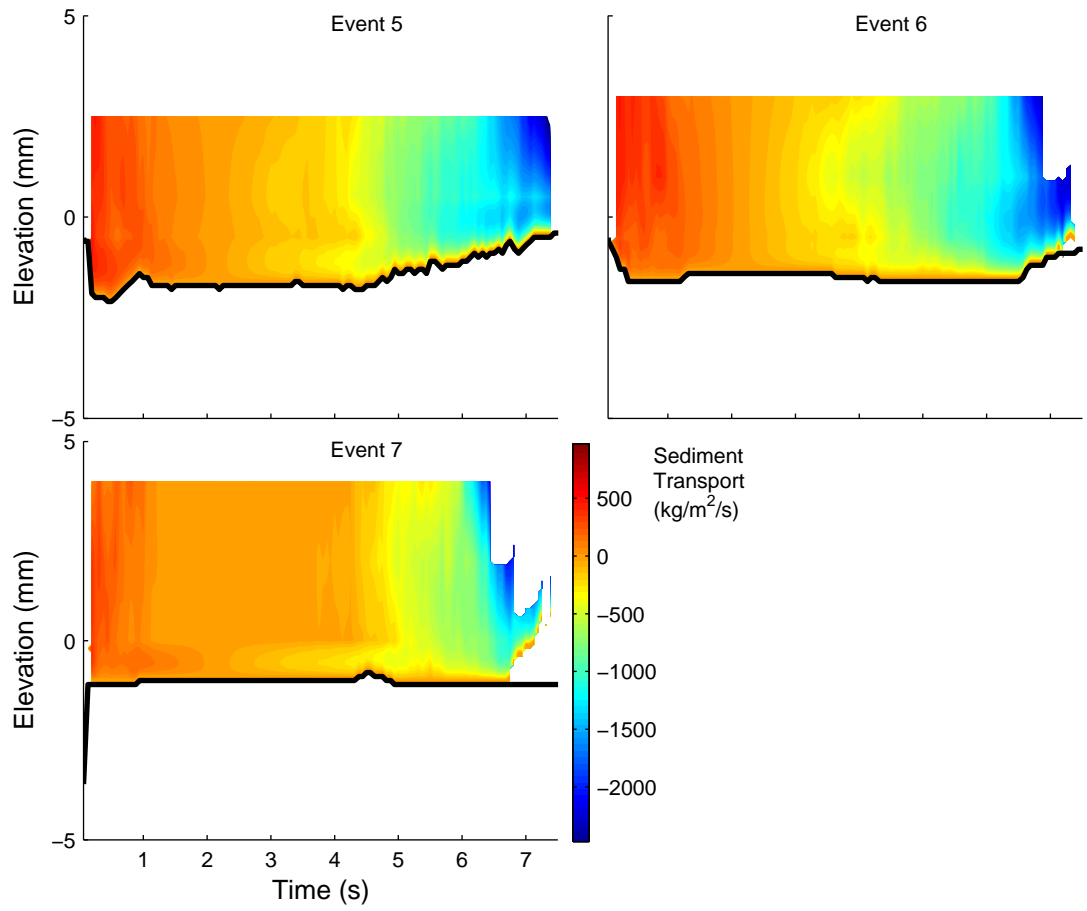
Figure A.4: The calculated transport profiles by applying the logarithmic ($k_s = 0.44$ mm) velocity boundary layer profiles throughout swash events 5-9 collected at x = 0.90 are shown.

A.2 $k_s = 3.67$ mm

The figures in this section show the instantaneous sediment transport profiles for each swash event at either cross shore location (x = 0.37 m and x = 0.90 m) using the logrithmic velocity profile corresponding to $k_s = 3.67$ mm.
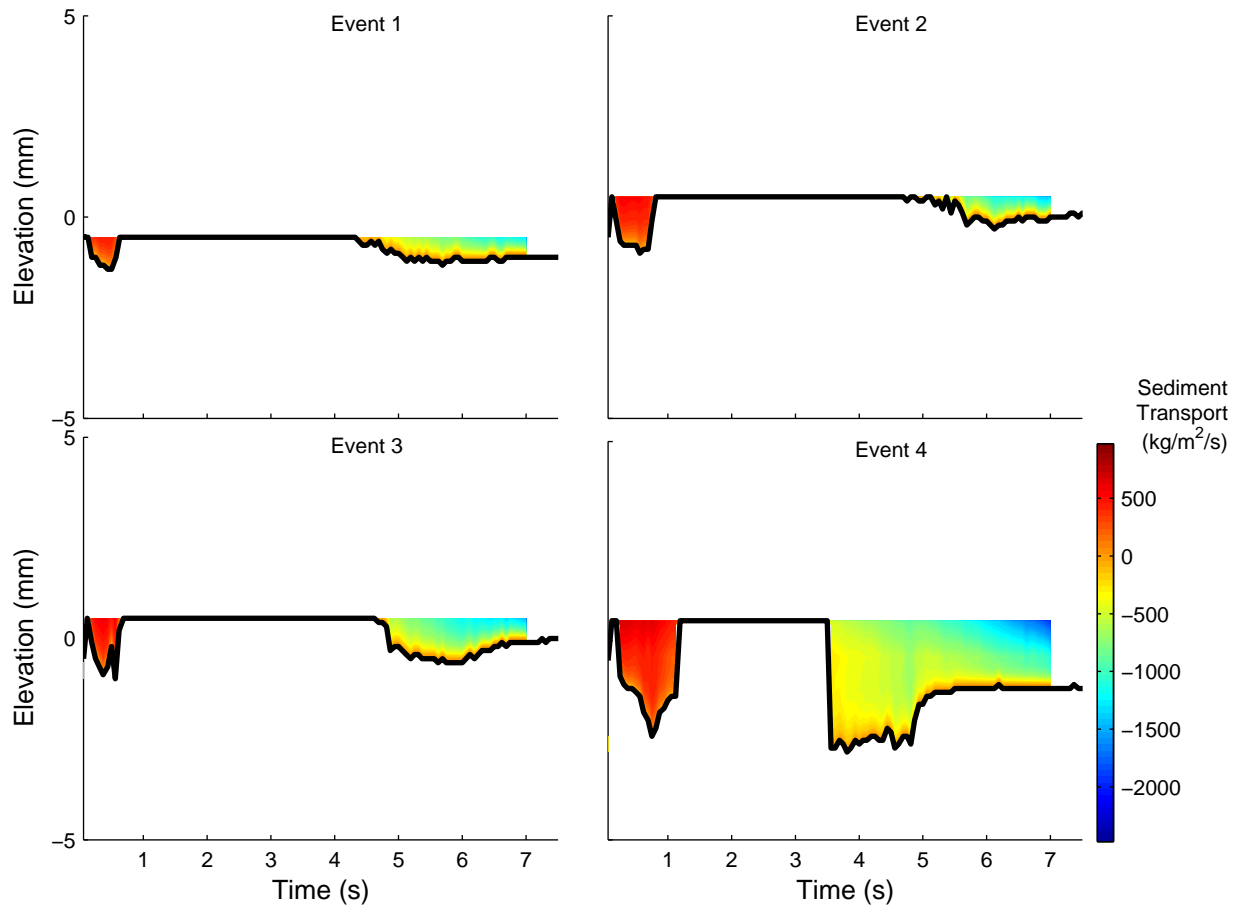

Figure A.5: The calculated transport profiles by applying the logarithmic ($k_s = 3.67$ mm) velocity boundary layer profiles throughout swash events 1-4 collected at x = 0.37 are shown.
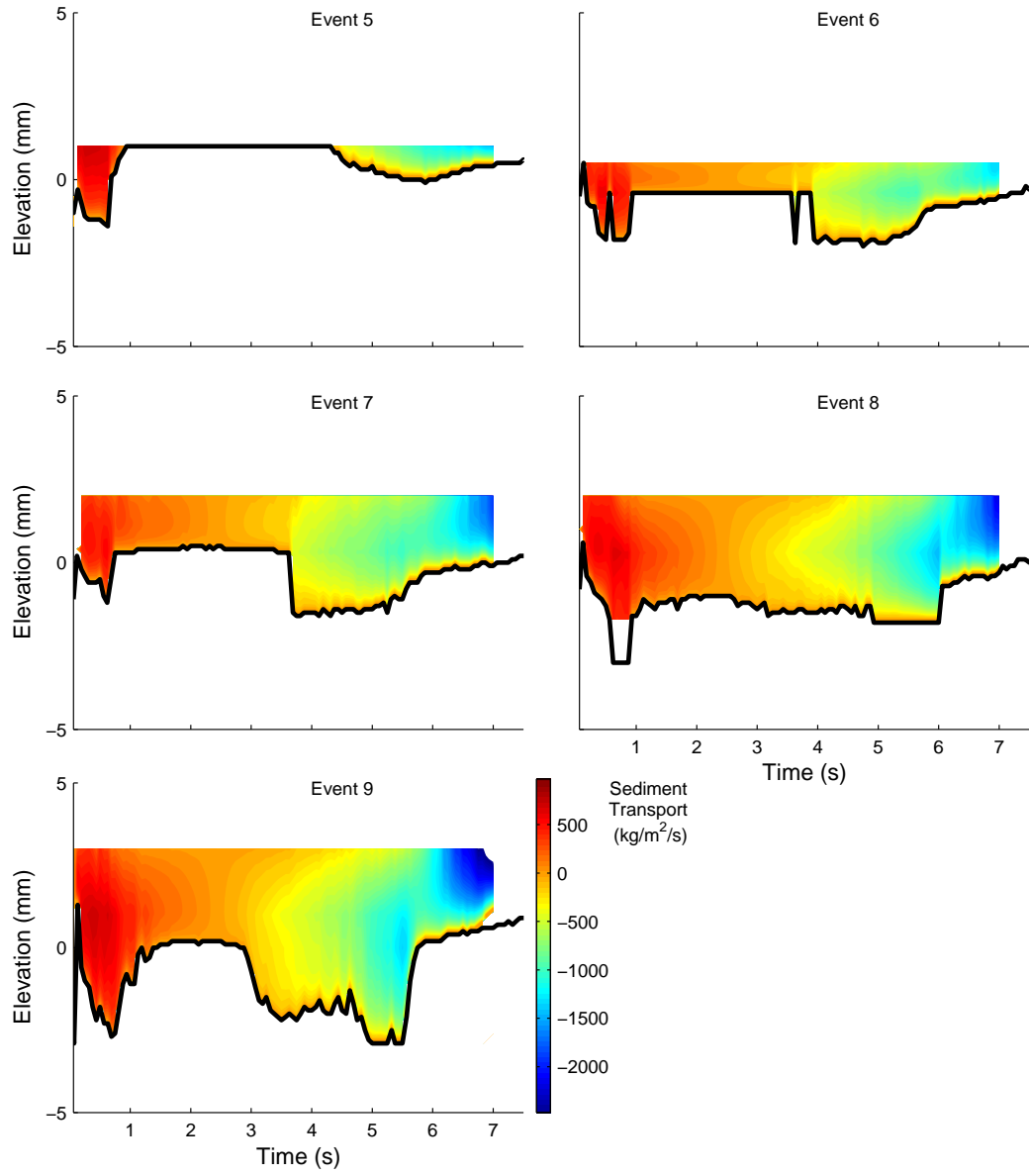
Figure A.6: The calculated transport profiles by applying the logarithmic ($k_s = 3.67$ mm) velocity boundary layer profiles throughout swash events 5-7 collected at x = 0.37 are shown.

Figure A.7: The calculated transport profiles by applying the logarithmic ($k_s = 3.67$ mm) velocity boundary layer profiles throughout swash events 1-4 collected at x = 0.90 are shown.

Figure A.8: The calculated transport profiles by applying the logarithmic ($k_s = 3.67$ mm) velocity boundary layer profiles throughout swash events 5-9 collected at x = 0.90 are shown.